

# Interhemispheric Comparisons of Large Nighttime Magnetic Perturbation Events Relevant to GICs

Mark J. Engebretson<sup>1</sup>, Kathryn R. Kirkevold<sup>2</sup>, Erik S. Steinmetz<sup>3</sup>, Vyacheslav A. Pilipenko<sup>4</sup>, Mark B. Moldwin<sup>5</sup>, Brett A. McCuen<sup>6</sup>, C. Robert Clauer<sup>7</sup>, Michael D. Hartinger<sup>8</sup>, Shane Coyle<sup>9</sup>, Hermann J. Opgenoorth<sup>10</sup>, Audrey Schillings<sup>11</sup>, Anna Willer<sup>12</sup>, Thom R Edwards<sup>13</sup>, David H Boteler<sup>14</sup>, Andrew J. Gerrard<sup>15</sup>, Mervyn P. Freeman<sup>16</sup>, and Mike C Rose<sup>16</sup>

<sup>1</sup>Department of Physics, Augsburg University

<sup>2</sup>Augsburg University

<sup>3</sup>Department of Computer Science, Augsburg University

<sup>4</sup>Space Research Institute

<sup>5</sup>University of Michigan-Ann Arbor

<sup>6</sup>University of Michigan

<sup>7</sup>Virginia Polytechnic Institute and State University

<sup>8</sup>Space Science Institute

<sup>9</sup>Virginia Tech

<sup>10</sup>Umeå University

<sup>11</sup>Swedish Institute of Space Physics

<sup>12</sup>Technical University of Denmark

<sup>13</sup>DTU Space, Technical University of Denmark

<sup>14</sup>Natural Resources Canada

<sup>15</sup>New Jersey Institute of Technology

<sup>16</sup>British Antarctic Survey

November 23, 2022

## Abstract

Nearly all studies of impulsive magnetic perturbation events (MPEs) with large magnetic field variability (dB/dt) that can produce dangerous geomagnetically-induced currents (GICs) have used data from the northern hemisphere. Here we present details of four large-amplitude MPE events ( $|\text{dBx}| > 900$  nT and  $|\text{dB/dt}| > 10$  nT/s in at least one component) observed between 2015 and 2018 in conjugate high latitude regions (65 - 80° corrected geomagnetic latitude), using magnetometer data from (1) Pangnirtung and Iqaluit in eastern Arctic Canada and the magnetically conjugate South Pole Station in Antarctica and (2) the Greenland West Coast Chain and two magnetically conjugate chains in Antarctica, AAL-PIP and BAS LPM. From 1 to 3 different isolated MPEs localized in corrected geomagnetic latitude were observed during 3 pre-midnight events; many were simultaneous within 3 min in both hemispheres. Their conjugate latitudinal amplitude profiles, however, matched qualitatively at best. During an extended post-midnight interval, which we associate with an interval of omega bands, multiple highly localized MPEs occurred independently in time at each station in both hemispheres. These nighttime MPEs occurred under a wide range of geomagnetic conditions, but common to each was a negative IMF Bz that exhibited at least a modest increase at or near the time of the event. A comparison of perturbation amplitudes to modeled ionospheric conductivities in conjugate hemispheres clearly favored a current generator model over a voltage generator model for 3 of the 4 events; neither

model provided a good fit for the pre-midnight event that occurred near vernal equinox.

1 Interhemispheric Comparisons of Large Nighttime Magnetic  
2 Perturbation Events Relevant to GICs

3  
4  
5  
6  
7 Mark J. Engebretson<sup>1</sup>, Kathryn R. Kirkevold<sup>1</sup>, Erik S. Steinmetz<sup>1</sup>, Viacheslav A. Pilipenko<sup>1,2</sup>,  
8 Mark B. Moldwin<sup>3</sup>, Brett A. McCuen<sup>3</sup>, C. R. Clauer<sup>4</sup>, Michael D. Hartinger<sup>4,5</sup>, Shane Coyle<sup>4</sup>,  
9 Hermann Opgenoorth<sup>6</sup>, Audrey Schillings<sup>6</sup>, Anna N. Willer<sup>7</sup>, Thom R. Edwards<sup>7</sup>, David H.  
10 Boteler<sup>8</sup>, Andy J. Gerrard<sup>9</sup>, Mervyn P. Freeman<sup>10</sup>, and Michael C. Rose<sup>10</sup>

11  
12  
13 <sup>1</sup> Augsburg University, Minneapolis, MN

14 <sup>2</sup> Institute of Physics of the Earth, Moscow, Russia

15 <sup>3</sup> University of Michigan, Ann Arbor, MI

16 <sup>4</sup> Virginia Tech, Blacksburg, VA

17 <sup>5</sup> Space Science Institute, Boulder, CO

18 <sup>6</sup> Umeå University, Umeå, Sweden

19 <sup>7</sup> DTU Space, Kgs. Lyngby, Denmark

20 <sup>8</sup> Natural Resources Canada, Ottawa, ON, Canada

21 <sup>9</sup> New Jersey Institute of Technology, Newark, NJ

22 <sup>10</sup> British Antarctic Survey, Cambridge, UK

23  
24 to be submitted to the Journal of Geophysical Research – Space Physics

25 date of this version: April 20, 2020

26

27

28

29

30 **Key Words:** geomagnetically-induced currents, magnetic perturbation events, substorms,  
31 magnetic storms, magnetic conjugacy, omega bands

32

33 **Key Points:**

34 Conjugate pre-midnight MPEs were largest in  $\text{dB}_x/\text{dt}$  and were often but not always  
35 simultaneous to within 3 min over  $\sim 100\text{-}700$  km in latitude.

36

37 Conjugate post-midnight MPEs were associated with omega bands, largest in  $\text{dBy}/\text{dt}$ , highly  
38 localized, and independent in time over  $\sim 1.5$  h.

39

40 Perturbation amplitudes and maximum derivatives favored a current generator model over a  
41 voltage generator model for near-solstice events.

42

43 **Abstract**

44 Nearly all studies of impulsive magnetic perturbation events (MPEs) with large magnetic  
45 field variability ( $\text{dB}/\text{dt}$ ) that can produce dangerous geomagnetically-induced currents (GICs)  
46 have used data from the northern hemisphere. Here we present details of four large-amplitude  
47 MPE events ( $|\Delta B_x| > 900$  nT and  $|\text{dB}/\text{dt}| > 10$  nT/s in at least one component) observed between  
48 2015 and 2018 in conjugate high latitude regions ( $65 - 80^\circ$  corrected geomagnetic latitude), using  
49 magnetometer data from (1) Pangnirtung and Iqaluit in eastern Arctic Canada and the  
50 magnetically conjugate South Pole Station in Antarctica and (2) the Greenland West Coast Chain  
51 and two magnetically conjugate chains in Antarctica, AAL-PIP and BAS LPM. From 1 to 3  
52 different isolated MPEs localized in corrected geomagnetic latitude were observed during 3 pre-  
53 midnight events; many were simultaneous within 3 min in both hemispheres. Their conjugate  
54 latitudinal amplitude profiles, however, matched qualitatively at best. During an extended post-  
55 midnight interval, which we associate with an interval of omega bands, multiple highly localized  
56 MPEs occurred independently in time at each station in both hemispheres. These nighttime  
57 MPEs occurred under a wide range of geomagnetic conditions, but common to each was a  
58 negative IMF  $B_z$  that exhibited at least a modest increase at or near the time of the event. A  
59 comparison of perturbation amplitudes to modeled ionospheric conductivities in conjugate  
60 hemispheres clearly favored a current generator model over a voltage generator model for 3 of

61 the 4 events; neither model provided a good fit for the pre-midnight event that occurred near  
62 vernal equinox.

63

## 64 **1. Introduction**

65 The study of Earth's space environment has in recent years become increasingly  
66 recognized as having significant practical importance as well as academic interest because of the  
67 damaging impacts that disturbances in the magnetosphere and ionosphere can impose on  
68 technological infrastructure. Extreme geomagnetically-induced currents (GICs) can disrupt the  
69 operation of large-scale ground-based electrically conducting systems such as electrical power  
70 grids, pipelines, telecommunication cables, and railway systems (Ngwira and Pulkkinen, 2019).  
71 Given this practical emphasis, it is not surprising that nearly all studies of the high latitude  
72 magnetic and electrical perturbations that can generate (GICs) have been based on data from the  
73 northern hemisphere. It is becoming increasingly clear that the chain of physical processes in the  
74 near-Earth magnetosphere and ionosphere that can generate GICs is complex (Viljanen, 1997;  
75 Henderson et al., 1998; Apatenkov et al., 2004; Ngwira et al., 2015, 2018; Kozyreva et al., 2018;  
76 and Dimmock et al., 2019) and that these events may be causally related to active conditions in  
77 the magnetotail such as bursty bulk flows and/or dipolarizing flux bundles (Angelopoulos et al.,  
78 1992; Sergeev et al., 1999; Kauristie et al., 2000; Zesta et al., 2000, 2006; Lyons et al., 2012;  
79 Gabrielse et al., 2014; Liu et al., 2014; and Engebretson et al., 2019b) that are expected to impact  
80 high latitude regions in both the northern and southern hemispheres.

81 Although the technological risk from GICs is greater during magnetic storms, when the  
82 auroral oval expands to subauroral latitudes, impulsive magnetic perturbation events (MPEs)  
83 with duration ~ 5 to 15 min have also been found to more often occur during non-storm times  
84 (Viljanen et al., 2006) and at up to at least 78° magnetic latitude (Engebretson et al., 2019a). A  
85 recent case study of three large amplitude MPEs observed using an extensive two-dimensional  
86 set of ground magnetometer arrays in Arctic Canada, Western Greenland, and Antarctica  
87 (Engebretson et al., 2019b) showed that these events appeared roughly simultaneously at near-  
88 magnetically-conjugate locations (at the northern and southern ends of the same magnetic field  
89 lines) in each hemisphere. In this study we present multi-station data from a large two-  
90 dimensional set of ground-based magnetometers in the northern hemisphere and magnetometers  
91 at magnetically conjugate locations in Antarctica, both covering a range in corrected

92 geomagnetic (CGM) latitude from  $\sim 65^\circ$  to over  $80^\circ$ . By detailing the similarities and differences  
93 between large MPEs in both hemispheres we provide additional information that may be helpful  
94 for understanding the physical mechanisms involved in their generation.

95

## 96 **2. Data Set and Event Identification Technique**

97 Vector magnetometer data used in this study were recorded by the MACCS (Engebretson  
98 et al., 1995) and CANMOS (Nikitina et al., 2016) arrays in Arctic Canada, the Greenland West  
99 Coast chain (<https://www.space.dtu.dk/MagneticGroundStations>), the conjugate AAL-PIP chain  
100 in Antarctica (Clauer et al., 2014), the British Antarctic Survey (BAS) Low Power  
101 Magnetometer chain (Kadokura et al., 2008), and the fluxgate magnetometer at South Pole  
102 Station, Antarctica (Lanzerotti et al., 1990; Engebretson et al., 1997). Data are presented in local  
103 magnetic coordinates. In the northern hemisphere (at MACCS, CANMOS and Greenland West  
104 Coastal chain stations) and in the southern hemisphere (at AAL-PIP and BAS LPM stations) the  
105 sensor axes are oriented as follows: X: magnetic north, Y: magnetic east, and Z: vertically  
106 down. The South Pole magnetometer sensors are X: magnetic north, Y: magnetic east, and Z:  
107 vertically upward (a left-handed system). The sampling rate of MACCS data is 2 Hz, and for the  
108 other stations 1 Hz.

109 Figure 1 and Table 1 show that South Pole Station in Antarctica is in approximate  
110 magnetic conjugacy to MACCS station Pangnirtung and CANMOS station Iqaluit in Canada.  
111 Figure 1 also shows that the six AAL-PIP stations in Antarctica, located about  $20^\circ$  farther east in  
112 corrected geomagnetic (CGM) longitude, are in close magnetic conjugacy to the middle of the  
113 Greenland West Coast chain, and that the BAS LPM chain is conjugate in CGM magnetic  
114 latitude to several of the lower latitude Greenland West Coast stations, but approximately  
115 midway in CGM longitude between the Canadian and Greenland stations (Table 1).

116 The semi-automated procedure used to identify and quantify MPEs in these data sets is  
117 detailed in Engebretson et al. (2019a), and a summary is presented here. Routinely produced  
118 daily magnetograms (24-hour plots of magnetic fields in local geomagnetic coordinates) were  
119 displayed on a computer screen. Once a large-amplitude 5-10 minute duration magnetic  
120 perturbation was visually identified, the IDL cursor function was used to select times before and  
121 after a region of interest containing the MPE. The times and values of extrema in this interval  
122 were recorded for each component, and after application of a 10-point smoothing to reduce noise

123 and eliminate isolated bad data points, the data were numerically differentiated. Plots of the time  
124 series of data and derivatives were produced and saved, and the maximum and minimum  
125 derivative values were automatically determined and recorded.

126

### 127 **3. Event Studies**

128 In this section we present four intervals of large-amplitude MPEs that were observed at  
129 both northern and southern high latitudes. In each case we also show OMNI interplanetary  
130 magnetic field (IMF) and solar wind data, time-shifted to the nose of the magnetosphere, as well  
131 as the SYM/H index and the SuperMAG SML and SMU indices (Newell and Gjerloev, 2011) of  
132 magnetic activity. The first three intervals occurred in the pre-midnight sector under conditions  
133 ranging from geomagnetically quiet to storm time. The fourth interval occurred in the post-  
134 midnight sector during the main and early recovery phases of a more intense magnetic storm.

135 For all three pre-midnight MPE intervals studied here, the largest  $|dB/dt|$  values occurred  
136 during a sharp initial pulse which set up the MPE. In contrast, within the post-midnight interval  
137 sharp (but less intense) pulses were seen at different times at each site over a span of  $\sim 1.5$  hours.  
138 Their multiple rapid variations resembled those of Pi 3 or Ps 6 pulsations (Opgenoorth et al.,  
139 1983; Solovyev et al., 1999; Apatenkov et al., 2020) rather than solitary impulses. Figure 2, a  
140 full-day magnetogram AAL-PIP PG4 on May 13, 2015, shows good examples of both pre- and  
141 post-midnight events. The post-midnight interval, to be discussed in detail in section 3.4 below,  
142 extended from 05:30 to 08:00 UT and was characterized by a long-lasting  $\sim 800$  nT negative bay  
143 in the Bx (north-south) component and three large  $\sim 20$  minute period pulsations of 200 nT  
144 amplitude in the Bx and By (east-west) components. The pre-midnight interval on this day was  
145 dominated by a single  $> 800$  nT southward (negative) impulse in the Bx component near 23:00  
146 UT. Large  $|dB/dt|$  values occurred during both events. The maximum derivatives during the  
147 pre-midnight interval were  $-14.5$  nT/s ( $dBx/dt$ ),  $9.4$  nT/s ( $dBy/dt$ ), and  $16.5$  nT/s ( $dBz/dt$ ).  
148 During the post-midnight event they were  $-5.2$  nT/s ( $dBx/dt$ ),  $5.2$  nT/s ( $dBy/dt$ ), and  $-6.1$  nT/s  
149 ( $dBz/dt$ ).

150

#### 151 3.1 Interval 1: 15 January 2018 00:24 – 00:51 UT YRDAY 18015

152 Figure 3a shows IMF and solar wind parameters from the OMNI database as well as the  
153 SuperMAG SML and SMU indices and the SYM/H index, from 2200 UT January 14, 2018 to

154 0200 UT January 15, 2018. Figures 3b and 3c show 3-component magnetic field data from  
155 AAL-PIP PG3 in Antarctica and Qeqertarsuaq (GDH) in Greenland. These stations were in  
156 close magnetic conjugacy, separated by  $0.6^\circ$  in CGM Lat and  $1.1^\circ$  in CGM Lon (Table 1 and  
157 Figure 1). The shaded region, from 00:24 to 00:51 UT January 15, spans the large magnetic  
158 perturbation observed at both stations. Substorm onsets included in the SuperMAG substorm list  
159 for 2018 occurred at 23:32 UT January 14 at  $67.8^\circ$  MLAT and 1.33 h MLT and 00:22 UT  
160 January 15 at  $66.86^\circ$  MLAT and 1.77 MLT). The times of these onsets, marked in Figure 3a by  
161 red arrows, were  $\sim 1$  hour and  $\sim 2$  minutes, respectively, before the beginning of the MPE interval,  
162 and they occurred  $\sim 4$ -5 h MLT distant from the MLTs of the arrays of stations analyzed for this  
163 event (Figure 4).

164 Before the onset of the MPE, the IMF magnitude increased slightly and the IMF Bz  
165 component was slightly negative but increasing toward 0. Both the IMF Bx and By components  
166 were near -4 nT (not shown), so the IMF had the most typical “garden-hose” orientation. The  
167 solar wind velocity ( $V_{sw}$ ) and dynamic pressure ( $P_{sw}$ ) were modest and relatively steady. The  
168 SML index decreased rapidly from -62 to -324 nT at the time of the first substorm onset,  
169 decreased rapidly again from -139 to -883 nT beginning near the time of the second substorm  
170 onset, and increased toward -500 nT near the end of the MPE interval. The SYM/H index  
171 decreased slightly before MPE onset to -14 nT and also remained near this level during the MPE.

172 As shown in Figures 3b and 3c, the Bx components at both GDH and PG3 reached their  
173 minimum value at 00:35 UT, 13 min after the most recent substorm onset. Perturbations in By  
174 and Bz had opposite signs at the two stations, and as was the case for each of the 4 events shown,  
175 also showed less similarity in shape than the Bx perturbations. The relative orientations of the  
176 Bx and By perturbations most likely reflect the hemispheric difference in the circular Hall  
177 current flow around a localized field-aligned current (FAC), counter-clockwise in the northern  
178 hemisphere and clockwise in the southern hemisphere. Also shown in these figures are the  
179 magnitude of the maximum derivative in each component. Both the perturbations ( $\Delta B$ ) and  
180 derivative amplitudes  $|dB/dt|$  in each component were slightly larger in the northern hemisphere.

181 Figure 4 shows Bx (north-south) component data from several stations during this event,  
182 organized by increasing local time (left to right) and decreasing magnetic latitude (top to  
183 bottom). Panel a) shows data from the near-conjugate South Pole and Pangnirtung station pair,  
184 panel b) shows data from AAL-PIP stations PG2, PG3, and PG5 and BAS LPM stations M79

185 and M78 in Antarctica, and panel c) shows data from West Greenland stations UMQ, GDH,  
186 STF, GHB, FHB, and NAQ. The same vertical and horizontal ranges are used in each panel. At  
187 each station, the time of maximum  $|\Delta B_x|$  perturbations is shown.

188 There was good agreement in the timing of Bx minima near 00:35 UT between northern  
189 and southern hemisphere stations with  $|\text{MLAT}| \geq 73.9^\circ$  in both local time sectors: PGG, UMQ,  
190 and GDH in Canada and Greenland, and SP, PG2, and PG3 in Antarctica, with amplitudes larger  
191 in the northern (winter) hemisphere. Two minima in Bx occurred at three intermediate latitude  
192 stations (STF, PG5, and GHB) between 00:20 and 01:00 UT, with no simultaneity between  
193 stations, and none showed evidence of the minimum at 00:35 UT that was observed at more  
194 poleward stations. One maximum in Bx occurred at the four lowest latitude stations (FHB, M79,  
195 NAQ, and M78). The largest derivative was in the X component at 8 stations, in the Z  
196 component at 4 stations, and in the Y component at none.

197 The  $\Delta B_x$  polarity reversal between  $69.3^\circ$  and  $66.6^\circ$  MLAT suggests the presence of an  
198 ionospheric flow shear, with westward flow poleward and eastward equatorward of it. The  
199 positive perturbation observed at the lower latitudes may represent the equivalent return current  
200 of the westward current in the negative  $\Delta B_x$  spike observed at higher latitudes. It is possible that  
201 the negative spike at 00:21 UT observed at PG5 was caused by a westward traveling surge that  
202 moved westward and poleward to appear successively later at more poleward stations: at 00:26  
203 UT at STF, at 00:33 UT at Pagnirtung, and between 00:35 and 00:39 at PG3, PG2, GDH, and  
204 UMQ. This would be qualitatively consistent with the progressive appearance of MPEs at more  
205 westward and poleward stations found in three recent case studies of MPEs by Engebretson et al.  
206 (2019b) using a two-dimensional array of stations in Arctic Canada.

207 Figure 5a shows the north-south perturbation amplitudes ( $\Delta B_x$ ) and Figure 5b shows the  
208 maximum derivative amplitude in any component observed at every available station during this  
209 event in the West Greenland Coastal Array (red triangles) and the conjugate AAL-PIP and BAS  
210 LPM arrays (black asterisks). Discussion of Figure 5c is deferred until section 4. In the MLAT  
211 range from  $\sim 70^\circ$  to  $\sim 76^\circ$ , corresponding to a distance of  $\sim 700$  km in both hemispheres, the  
212 amplitudes of both the perturbations and derivatives were larger in the northern hemisphere.  
213 However, the latitude profiles for  $\Delta B_x$  and maximum  $dB/dt$  in Greenland did not follow each  
214 other closely in the region of largest amplitudes. In both hemispheres the equatorward falloff of  
215 amplitude with MLAT was more gradual than its poleward counterpart.

216 The second column of Table 2 shows the maximum  $|dB/dt|$  values for each component  
217 for each of the stations shown in Figure 4. At the West Greenland stations and their conjugate  
218 arrays the maximum derivatives were larger in the northern hemisphere. However, the MLT  
219 dependence was complex: Figure 4a shows that farther west, the  $\Delta B_x$  value at SPA was smaller  
220 than that at PGG, but Table 2 indicates its peak derivative value was larger than that of any other  
221 station in the data set. During this interval the largest derivative was in the X component at 8  
222 stations, in the Z component at 4 stations, and in the Y component at none.

223

### 224 3.2 Interval 2: 16 March 2016 00:34-00:57 UT YRDAY 16076

225 This complex MPE interval, which had significant amplitude over an MLAT range of at  
226 least  $10^\circ$ , occurred during the early recovery phase of a weak magnetic storm, as shown in Figure  
227 6a. The SYM/H index decreased modestly from -30 to -50 nT between 22:00 and 24:00 UT on  
228 March 15, and showed a slight  $< 5$  nT increase before the interval and a similar small decrease  
229 during the interval. The IMF magnitude remained steady near 8 nT for  $\sim 2$  h before and during  
230 the highlighted interval and again the IMF Bz component was negative (-4 nT) but increased  
231 shortly before and during the interval. Both the IMF Bx and By components were near 0 nT (not  
232 shown). Vsw and Psw were again relatively constant before and during the interval. A substorm  
233 onset occurred at 23:51 UT March 15, at  $70.98^\circ$  MLAT and 8.37 h MLT. The time of this onset,  
234 shown in Figure 6a, was 40 minutes before the beginning of the MPE interval, and it occurred  
235 more than 10 h MLT away from the magnetometer stations shown in Figure 7.

236 A broad minimum in SML and maximum in SMU were evident during this MPE interval,  
237 after which time both indices gradually returned to more quiet levels. The SML index dropped  
238 gradually from  $\sim -284$  nT at onset to a minimum of -742 nT at 00:18 UT, and at 00:43 UT  
239 exhibited a short  $\sim -200$  nT negative spike, near the time of the large amplitude spikes shown in  
240 Figure 6b and c.

241 Three-component magnetic field data from PG4 and STF (Figures 6b and 6c) show  
242 similar Bx waveforms with minima simultaneous to within 1 min, again oppositely directed  
243 perturbations in By, and complex variations in Bx. In all three components the amplitudes of  
244 both the perturbations and derivatives were larger in the southern hemisphere.

245 This interval also showed latitude-dependent variations in timing that were very similar  
246 in both hemispheres (Figure 7). A Bx minimum occurred simultaneously to within 1 min at

247 00:48 UT at the four most poleward stations in both hemispheres ((SP, PG2, PG3, and GDH, all  
248 above  $73.9^\circ$  |MLAT|), but occurred earlier (at 00:42 UT) at the two Canadian stations (PGG,  
249 IQA). In the |MLAT| range from  $69.8^\circ$  to  $71.9^\circ$  a Bx minimum occurred nearly simultaneously  
250 at 00:37 UT at Antarctic stations PG4, M85 (not shown), PG5, and M84 (not shown), and at STF  
251 in Greenland, and Bx minima appeared at SKT and GHB in Greenland 1-3 minutes later. A  
252 more temporally extended substorm bay in Bx rather than a single dominant but short-lived  
253 negative perturbation was observed at the four lower latitude stations (M81, M79, FHB, and  
254 NAQ). Rapid negative excursions in Bx were evident at each of these four stations and at GHB,  
255 during the downward slope of the bay between 00:35 and 00:37 UT, but were in each case  
256 (except at M79) relatively small. It is possible that the 00:35-00:37 UT disturbance that first  
257 appeared at these lower latitude stations expanded poleward and westward to appear later at  
258 higher latitude stations, as in interval 1.

259 Figure 8 shows latitudinal profiles of the  $\Delta B_x$  perturbation amplitude (panel a) and the  
260 maximum derivative amplitude (panel b), as in Figure 5. At all latitudes both quantities were  
261 consistently larger in the southern hemisphere, and the latitudinal profiles were similar, with one  
262 major exception: the derivative amplitude at M84, located  $10^\circ$  magnetic longitude west of PG5  
263 and other AAL-PIP stations, was substantially larger ( $25.7$  nT/s) than the amplitude at PG5 ( $16.2$   
264 nT/s). Figure 7a shows that the  $\Delta B_x$  value at SP in Antarctica was also larger than at the Arctic  
265 stations PGG and IQA.

266 The third column of Table 2 shows the maximum  $|dB/dt|$  values for each component for  
267 each of the stations shown in Figure 7. During this interval the derivatives were consistently  
268 larger at all stations in the southern hemisphere than at northern hemisphere stations at  
269 comparable latitudes and local times. The largest derivative was in the X component at 11  
270 stations, in the Z component at 2 stations, and in the Y component at one (SPA). Derivative  
271 magnitudes were nearly equal in X and Z at 2 stations.

272

### 273 3.3 Interval 3: 8 May 2016 21:02-21:30 UT YRDAY 16129

274 This MPE interval, which occurred shortly before the second minimum of a double-  
275 minimum geomagnetic storm (minimum SYM/H  $\sim -87$  nT, Figure 9a), included an extremely  
276 large  $dB/dt$  value of  $37.7$  nT/s at BAS LPM M79, but appeared only within an |MLAT| range of  
277  $\sim 5^\circ$ , from  $64^\circ$  to  $69^\circ$ . During and before this interval the IMF magnitude was relatively steady

278 near 8 nT, and the IMF Bz component was increasing from a slightly negative value. The IMF  
279 Bx and By components were near +3 and -3 nT, respectively (not shown), so the IMF had an  
280 “ortho-garden hose” orientation. Vsw was over 600 km/s and falling slightly during the interval,  
281 and Psw was near 3.4 nPa. Multiple substorm onsets occurred at 1809 UT at 66.70° MLAT and  
282 2.75 h MLT; 18:48 UT at 70.6° MLAT and 7.13 h MLT; 19:08 UT at 65.94° MLAT and 6.01 h  
283 MLT; 19:48 UT at 65.94° MLAT and 6.69 h MLT; and 20:12 UT at 65.94° MLAT and 7.09 h  
284 MLT. The times of these onsets, shown in Figure 9a, were from ~1 - 3 hours before the  
285 beginning of the MPE interval, and they occurred ~7 to 12 h MLT away from the magnetometer  
286 stations shown in Figure 10.

287 The SML index decreased from -457 nT at the time of the latest substorm onset 20:12  
288 UT) to -1022 nT at 20:23 UT, and returned to near -500 nT at 20:55 before dropping to -699 nT  
289 near the beginning of the MPE interval. The SMU index was relatively steady near 400 nT for  
290 nearly 3 hours, from 18:00 to 20:55 UT, before rising to 616 nT at 21:02 UT, the beginning of  
291 the MPE interval. The variation of SMU and SML approximately in tandem shortly before and  
292 during the interval suggests the occurrence of a magnetospheric convection event or  
293 pseudobreakup. Both SML and SMU values gradually returned to more quiet levels during and  
294 after the MPE interval.

295 Figures 9b and 9c show magnetograms from BAS LPM M79 and FHB, respectively,  
296 from 20:00 to 22:00 UT on this day. A single Bx minimum at M79 appeared at 21:07 UT, and  
297 two Bx minima appeared at FHB at 21:04 and 21:22 UT, respectively. The largest dBx/dt  
298 excursion at FHB was substantial ( -6.7 nT/s), but was a factor of ~5 smaller than that at M79.

299 Figure 10 shows Bx component data from the four lowest latitude stations available in  
300 each hemisphere from 20:00 to 22:00 UT. Both  $\Delta B_x$  and the derivatives in each component at  
301 the Antarctic stations (Figure 10a) were highly localized in MLAT: as shown in Table 3, the  
302 maximum  $|dB_x/dt|$  value decreased to less than half its value at M79 within 1° and 1.7° toward  
303 higher and lower MLAT (at M81 and M78, respectively). The first MPE observed in Greenland  
304 occurred within ~3 minutes of the much larger MPE observed in Antarctica, and conversely  
305 there was no evidence of the second Greenland MPE at any of the Antarctic stations. Thus for  
306 both MPEs there was an apparent lack of conjugacy. However, as will be discussed in section 5,  
307 at least some of this lack of conjugacy might be attributed to longitudinal localization of both  
308 MPEs: BAS LPM stations M79 and M81 were located ~9° in magnetic longitude west of the

309 conjugate point of FHB – at distances of 431 and 429 km, respectively. Figures 11a,b show that  
310 magnetometer deflections and derivative amplitudes at stations at  $|\text{MLAT}| > 70^\circ$  in both  
311 hemispheres were at near background levels.

312 The fourth column of Table 2 shows the maximum  $|\text{dB}/\text{dt}|$  values for each component for  
313 the lowest latitude stations shown in Figure 10. During this interval the derivatives were again  
314 consistently larger in the southern hemisphere than at northern hemisphere stations at  
315 comparable latitudes. The largest derivative was in the X component at all stations shown except  
316 FHB, where it was largest in the Z component.

317 The observations at BAS LPMs M81, M79, and M78, located in nearly a straight line with  
318 similar MLON (to within  $1.5^\circ$ ) and MLAT (to within  $2.7^\circ$ ), can provide additional information  
319 about this MPE. The distance from M79 to M81 is 139 km, and from M79 to M78 is 240 km.  
320 At the most equatorward station, M78, the minimum in Bx occurred at 2105 UT. At M79 it  
321 occurred at 2107 UT, and at M81 it occurred at 2108 UT. This indicates a possible drift of the  
322 epicenter of the MPE westward and poleward. This drift is again consistent with that found in  
323 the Engebretson et al. (2019b) case studies.

324

#### 325 3.4 Interval 4: 13 May 2015 05:30-08:00 UT YRDAY 15133

326 This extended post-midnight interval occurred during the main phase of a large magnetic  
327 storm (minimum SYM/H = -95 nT), as shown in Figure 12a. The IMF magnitude was near 15  
328 nT before the beginning of the interval, and fell slightly to 12 nT at its end, and the IMF Bz  
329 component rose unsteadily from a large negative value (-13 nT) at 0500 UT to +4 nT by 07:00  
330 UT. The IMF Bx and By components were near +10 and -7 nT, respectively (not shown), so the  
331 IMF again had an “ortho-garden hose” orientation.  $V_{\text{sw}}$  fluctuated slightly near 600 km/s during  
332 the event, and  $P_{\text{sw}}$  varied near 7 nPa. Two substorm onsets occurred prior to this event, at 05:04  
333 UT at  $60.49^\circ$  MLAT and 1.87 h MLT and at 05:25 UT at  $67.47^\circ$  MLAT and 21.15 h MLT. The  
334 times of these onsets were 26 min and 5 min, respectively, before the beginning of the shaded  
335 MPE interval, and they occurred ~1-2 and 6-7 h MLT away from the magnetometer stations  
336 shown in Figure 13, respectively.

337 The SMU index rose gradually beginning near 04:35 UT from ~ 250 nT to a maximum of  
338 507 nT at 05:14 UT, fell to ~300 nT by 05:40 UT, and exhibited only modest variations during  
339 the remainder of the MPE interval. The SML index also began a gradual drop near 04:35 UT,

340 but declined sharply from the time of the second substorm onset, reaching a minimum of -1160  
341 nT at 05:46 UT before gradually returning toward more quiet levels, reaching values near -300  
342 nT near 08:00 UT.

343 The beginning and end times of this interval (05:30 to 08:00 UT) correspond to the  
344 duration of double-minimum negative bays in the Bx component at M81 (Figure 12b) and GHB  
345 (Figure 12c). These bays showed a rapid recovery in the Bx component between 06:30 and  
346 ~07:00 UT, followed by a slower recovery from 07:00 to 08:00 UT that was still characterized  
347 by large fluctuations in all 3 components. There was again little correspondence in the By and  
348 Bz components between the two stations.

349 Figure 13 shows that a large negative bay appeared all 14 stations shown, covering an  
350 MLAT range of  $>10^\circ$ , but was deeper and more extended at lower latitudes and in the southern  
351 hemisphere. This bay, and the many rapid perturbations embedded within it, resembles  
352 published signatures of omega band structures (e. g., Figure 4 of Opgenoorth et al., 1983). These  
353 multiple short-lived perturbations, which have been designated variously as Ps6 and Pi3  
354 magnetic pulsations (Solovyev et al., 1999), appeared in all 3 components at all stations (not  
355 shown), and were often largest in the By component, but were highly localized. At each station,  
356 the maximum derivative amplitude in each component is listed. Derivative amplitudes  
357 generally increased from higher to lower MLAT, but the largest derivatives appeared at different  
358 times at each station, and spanned the time range from 05:50 to 07:40 UT. Only at one  
359 neighboring station pair (FHB and GHB, separated by 262 km) at 06:55 UT was one  
360 simultaneous large perturbation observed. The blue arrows in each panel show the times of the  
361 largest derivatives in the Bx component. Two  $> 6$  nT/s derivatives in Bx appeared at M83 and  
362 M81 (Figures 13g and 13h), and two  $> 8$  nT/s derivatives in Bx appeared at NAQ (Figure 13n).  
363 At all other stations Bx derivative amplitudes were  $< 6$  nT/s; for these only the largest Bx  
364 derivative is shown (2 of equal magnitude at SP and FHB).

365 Figure 14a shows that similar latitudinal profiles of  $\Delta B_x$  occurred in both northern and  
366 southern hemispheres, with elevated values extending over nearly  $15^\circ$  MLAT and generally  
367 larger at lower latitudes, but their amplitude was 20% to 60% larger in the southern (winter)  
368 hemisphere. The derivative amplitudes (Figure 14b) were again larger at lower latitudes. They  
369 were again somewhat larger in the southern hemisphere, but showed large differences between

370 two pairs of Antarctic stations at similar MLAT but different MLON: M83 - M84 and PG4 –  
371 M85.

372 The fifth column of Table 2 shows the maximum  $|dB/dt|$  values for each component for  
373 the lowest latitude stations shown in Figure 13. In contrast to the pre-midnight MPEs, the largest  
374 derivative observed at the stations shown in Figure 13 was in the Y component at 6 stations,  
375 equal in the Y and Z components at 1 station, in the X component at 5 stations, and in the Z  
376 component at 3 stations.

377

#### 378 **4. Comparison of amplitudes in conjugate hemispheres**

379 In each of the 4 MPE intervals studied, the latitudinal profiles in conjugate hemispheres  
380 showed fair to good qualitative agreement (Figures 5, 8, 11, and 14). Conditions were dark at  
381 most sites in both hemispheres. During intervals 1, 3, and 4 both perturbation and derivative  
382 amplitudes were larger in the winter hemisphere by up to a factor of 3, but during the second  
383 (near-equinox) event, Antarctic stations recorded consistently larger amplitudes. Derivative  
384 amplitudes (but not perturbation amplitudes) also varied significantly between stations in the  
385 southern hemisphere that differed in magnetic longitude by  $6^\circ$  or more (e.g., the M84 - PG5 pair  
386 in Figure 8 and the M83 - M84 and PG4 – M85 pairs in Figure 14).

387 Many studies have suggested that MPEs are driven by localized field-aligned currents  
388 (e.g., Viljanen et al., 2001; Viljanen and Tanskanen, 2011; Belakhovsky et al., 2019), and in  
389 models of magnetosphere - ionosphere electrodynamic drivers it is physically intuitive to use a  
390 circuit analogy and distinguish between generators which deliver a fixed current and those in  
391 which the voltage is fixed (Lysak, 1990).

392 Distinctions between the applicability of these two drivers can be revealed by analyzing  
393 the dependence of the ground magnetic response on the ionospheric conductance. If the  
394 magnetospheric driving of a FAC behaves as a voltage generator, then one expects the ground  
395 magnetic field perturbation to increase as the ionospheric conductance increases. In contrast, if  
396 the magnetospheric process behaves as a current generator, one expects the intensity of magnetic  
397 field perturbations to remain only weakly sensitive to the ionospheric conductance.

398 Quantitative relationships between conjugate amplitudes and height-integrated  
399 ionospheric conductances for these two generators were examined by Pilipenko et al. (2019)  
400 using a simple "plasma box" model of the magnetosphere with asymmetric conjugate

401 ionospheres driven by an external current located at the magnetospheric equatorial plane. The  
 402 ranges of validity of current and voltage generators are determined by the ratio between an  
 403 internal generator resistance and a load resistance. For a FAC generator, the local ionospheric  
 404 resistance above an observation site plays the role of a load resistance, whereas the  
 405 magnetospheric Alfvén wave resistance and the resistance of the conjugate ionosphere play the  
 406 role of an internal source resistance. Oscillatory FACs interact with the ionosphere in a different  
 407 way depending on relationship between the driver periodicity  $\tau$  and the Alfvén field line  
 408 eigenperiod  $T_A$ .

409 For a forced quasi-DC driving ( $\tau \gg T_A$ ),

$$410 \quad \frac{\Delta B_x^{(N)}}{\Delta B_x^{(S)}} = \frac{\Sigma_H^{(N)}}{\Sigma_H^{(S)}}, \quad (1)$$

411 and for excitation of resonant field line oscillations ( $\tau \sim T_A$ ),

$$412 \quad \frac{\Delta B_x^{(N)}}{\Delta B_x^{(S)}} = \frac{\Sigma_H^{(N)}}{\Sigma_H^{(S)}} \frac{\Sigma_P^{(S)}}{\Sigma_P^{(N)}}. \quad (2)$$

413 The quasi-DC driving of a FAC corresponds to a voltage generator, for which the ground  
 414 magnetic response is proportional to the ionospheric Hall conductance. The excitation of  
 415 resonant field line oscillations corresponds to a current generator, for which the ground magnetic  
 416 response only weakly depends on the ionospheric conductance.

417 In order to determine the applicability of either of these models, the ratio of conductances  
 418 at conjugate points can be compared with the ratio of magnetic disturbance amplitudes. Because  
 419 MPEs are localized in both latitude and longitude, it is best to focus on stations observing the  
 420 maximal amplitude of the MPE as well as to examine these ratios at more than one station. The  
 421 bottom panels of Figures 5, 8, 11, and 14 show the ionospheric conductances calculated for each  
 422 interval at all available West Greenland and conjugate AAL-PIP and BAS-LPM stations. Solid  
 423 lines and dashed lines in panel c) of these figures denote Pedersen conductances ( $\Sigma_P$ ) and Hall  
 424 conductances ( $\Sigma_H$ ), respectively. These were determined using an updated AMIE procedure  
 425 based on an empirical model parameterized by solar zenith angle and the solar radio flux index,  
 426  $F_{10.7}$  (Cousins et al. (2015)).

427 Cousins et al. (2015) also noted that on physical grounds one would expect auroral  
 428 precipitation to contribute to ionospheric conductances. Panel d) of Figures 5, 8, and 14 shows

429 the above conductances plus conductances determined using the empirical relationship of  
430 Robinson et al (1987) that relates particle flux and energy output to conductance, using the  
431 Ovation Prime DMSP-based empirical auroral precipitation model (Newell et al., 2009, 2010,  
432 2014). This augmented model contributed only negligible additional conductances for interval 3  
433 because the modeled auroral zone was located below the MLAT range of the available stations,  
434 so Figure 11 does not include this additional panel.

435 However, Cousins et al. (2015) noted that large uncertainties remain in all current  
436 conductance models. They evaluated a number of conductance models and adjustments,  
437 including both of those described above, using metrics based on comparing SuperDARN plasma  
438 drift data to AMPERE field-aligned current data by means of these conductance models, and  
439 found that none of the model combinations they tested generated significantly better agreement.  
440 In addition, the localized field-aligned currents that drive MPEs are expected to produce  
441 localized increases of unknown size in ionospheric conductances, and no model including such  
442 effects yet exists.

443 During the northern winter event shown in Figure 5, the magnetic perturbations and  
444 derivatives were mostly somewhat larger in the northern hemisphere, but in both conductance  
445 models both  $\Sigma_p$  and  $\Sigma_H$  were larger in the southern hemisphere. These relations are opposite to  
446 those expected for a voltage generator. Southern hemisphere (summer) conductances based on  
447 the AMIE model (Figure 5c) increased relatively smoothly with MLAT, while in the augmented  
448 model (Figure 5d) the contribution of modeled auroral precipitation is evident for MLAT < 70°.  
449 Northern hemisphere (winter) conductances based on the AMIE model were nearly constant, and  
450 the auroral contribution in the augmented model extended to 73° MLAT. These additions are  
451 consistent with the center of the modeled auroral zone being located at or equatorward of 65°  
452 MLAT.

453 Inverse interhemispheric patterns are evident in Figure 14cd during northern summer  
454 events: magnetic perturbations and derivatives were mostly larger in the southern hemisphere,  
455 and conductances were much larger in the northern hemisphere. Northern hemisphere (winter)  
456 conductances based on the AMIE model (Figure 14c) increased relatively smoothly with MLT,  
457 while southern hemisphere conductances were nearly constant. The augmented model (Figure  
458 14d) again increased the conductances at lower latitudes, but in this case again more rapidly in  
459 the southern hemisphere. The MPE event in interval 3 (Figure 11) was considerably more

460 localized in latitude, and also occurred in a region with nearly constant conductances that was  
461 poleward of the modeled auroral zone. Both intervals 3 and 4 occurred during northern summer  
462 and showed the same seasonal interhemispheric patterns. It is also clear in Figures 5, 11, and 14  
463 that peak MPE amplitudes occurred in latitudinal regions of near-constant conductances, based  
464 on both models. These relations indicate that for both pre-midnight and post-midnight events  
465 during solstice conditions the voltage generator model is not applicable to MPEs.

466 In order to make a more quantitative comparison between models, we chose 4 station  
467 pairs in regions of relatively constant conductances from both interval 1 (between  $69^\circ$  and  $76^\circ$   
468 MLAT) and interval 4 (between  $70^\circ$  and  $76^\circ$  MLAT) and calculated both  $\Delta B_x$  ratios and the  
469 AMIE model conductance ratios defined in equations (1) and (2). The ratios between left and  
470 right sides of equation (1) for a voltage generator model were  $7.08 \pm 3.96$  and  $0.159 \pm 0.032$  for  
471 intervals 1 and 4, respectively (nearly inverse between winter and summer), while the  
472 corresponding ratios of equation (2) for a current generator model were  $1.48 \pm 0.15$  and  $1.10 \pm$   
473  $0.17$ , both much closer to unity, and thus approximately satisfying the equality. Comparisons for  
474  $|dB/dt|$  ratios were similar: the ratios for a voltage generator model were  $6.16 \pm 3.42$  and  $0.315 \pm$   
475  $0.172$  for intervals 1 and 4, respectively, and the ratios for a current generator model were  $1.31 \pm$   
476  $0.15$  and  $2.19 \pm 1.28$ . The greater scatter in the  $|dB/dt|$  ratios for both models using data from  
477 interval 4 is consistent with the greater variability in  $|dB/dt|$  values for this interval shown in  
478 Figure 14b, which we attributed to longitudinal variations. Given the known uncertainties in the  
479 modeled conductances (Cousins et al., 2015), comparison of these ratios indicates the  
480 reasonableness of using a current generator model to drive these events.

481 The conductances for the 16 March 2016 pre-midnight event that occurred close to  
482 equinox (Figure 8c,d) showed more complex behavior. The AMIE conductances were below 1 S  
483 in both hemispheres below  $72^\circ$  MLAT (Figure 8c), but the southern hemisphere conductances  
484 increased toward higher latitudes while the northern hemisphere conductances remained  
485 constant. The augmented conductances shown in Figure 8d again showed the influence of an  
486 auroral zone for  $MLAT < \sim 72^\circ$ . As with the other intervals, neither conductance profile matched  
487 the large-scale latitudinal profiles of magnetic perturbations or derivatives shown in Figures 8a  
488 and 8b; the largest perturbations and derivatives occurred between  $66^\circ$  and  $72^\circ$  MLAT, in ranges  
489 of relatively flat conductances in the AMIE model and of both high and low conductances in the  
490 augmented model. During this event both perturbations and derivatives were larger in the

491 southern hemisphere even near  $72^\circ$  MLAT, where the conductances for both models were nearly  
492 equal. In addition, the latitudinal profile in the southern hemisphere between  $69^\circ$  and  $72^\circ$  MLAT  
493 (blue traces) showed sharp changes in conductances between M84 and PG5 and between PG4  
494 and M85 (Figures 8b,c) that correspond to sharp changes in derivative and perturbation  
495 amplitude (Figures 8a,b). Similar sharp changes also appeared in Figure 11c. As noted near the  
496 beginning of this section, these changes appear to be linked to differences in station longitude,  
497 but the relative polarity of the changes is more consistent with a voltage generator model than a  
498 current generator model.

499 Several factors may complicate the modeling of ionospheric conductances in  
500 magnetically conjugate points, especially near equinoxes: a) the differing effects on ground  
501 conductivity of coastlines and oceans in the north vs. ice sheets in the south, b) the different  
502 distances and azimuths between the geographic and geomagnetic poles in opposite hemispheres  
503 (Liou et al., 2018), and c) the fact that Antarctic stations in this study were situated at  $13$ - $18^\circ$   
504 higher geographic latitude than Arctic stations at similar MLAT. However, addressing these  
505 factors quantitatively is beyond the scope of this paper.

506

## 507 5. Discussion

508 This study has presented four examples of nighttime MPEs observed by multiple  
509 magnetometers in near-magnetically conjugate regions in both polar regions. We here  
510 summarize both the commonalities and differences between these events.

511 The geomagnetic context of these four MPE intervals was similar only in that the  $B_z$   
512 component of the IMF was  $< 0$  before each event, and had at least a modest increase at or near  
513 the time of the event. MPEs could occur during both magnetically quiet times and storm times,  
514 but little or no change in solar wind pressure or velocity occurred shortly before or during each  
515 event, and there was no consistent pattern in IMF  $B_x$  or  $B_y$  levels or trends. Clear minima in the  
516 SML index were evident in each of the MPE intervals presented here, but as was the case for the  
517 statistical and event studies of MPEs presented by Engebretson et al. (2019a,b), there was no  
518 consistent timing of events relative to the most recent substorm onset(s).

519 The availability of data from latitudinally-spaced stations covering nearly  $15^\circ$  in MLAT  
520 makes it possible to characterize the latitudinal extent of individual MPEs. Pre-midnight MPEs  
521 did not extend over large latitude ranges: one, two, or three independent events could appear

522 across the available latitude range, with the more poleward events occurring some few minutes  
523 later. Simultaneous large-amplitude pre-midnight impulses in event 1 occurred over an MLAT  
524 range of ~320 km (the distance from STF to GHB, the extent of the central range in Figure 4). In  
525 event 2 they occurred over ranges from 436 km (the distance from PG4 to M84, the central range  
526 in Figure 7 in which a large negative Bx impulse dominated the signal) to 703 km (the distance  
527 from PG4 to M79, the full range of latitudes over which a Bx minimum near 0037 UT was  
528 observed).

529         The amplitude and location data for the MPE event during interval 3 (Figure 11) can be  
530 used to estimate its latitudinal and longitudinal scale size. Using a linear slope calculation  
531 between pairs of stations gives the half-amplitude falloff distances shown in Table 3. For the  
532 two lowest-latitude and relatively closely-spaced BAS-LPM station pairs, these latitudinal  
533 distances ranged from 106 to 192 km, and for the two somewhat less closely-spaced West  
534 Greenland stations at nearly the same magnetic longitude, 204 km. The longitudinal half-  
535 amplitude falloff distances between BAS LPM stations M81 and M79 and the conjugate location  
536 to Greenland station FHB were 446 and 262 km, respectively. These latitudinal distances are  
537 roughly comparable to but mostly lower than the ~275 km two-dimensional half-amplitude  
538 radius calculated for several events in Arctic Canada using the SECs technique by Engebretson  
539 et al. (2019a,b), and the longitudinal distances are comparable to or somewhat higher. An MPE  
540 event with even larger differences in perturbation amplitude between relatively closely spaced  
541 stations than this one is shown in Figures 3 and 4 of Pulkkinen et al. (2015).

542         During the extended post-midnight interval multiple highly localized MPEs occurred  
543 independently in time at each station in both hemispheres, embedded within large amplitude,  
544 longer-duration magnetic bays (Figure 13). Only at the FHB-GHB station pair did one event  
545 occur simultaneously. MPE derivative amplitudes  $\geq 6$  nT/s appeared from 65.0° to 71.9°  
546 MLAT (NAQ to STF, a distance of 700 km). Based on the latitudinal profiles in Figure 14,  
547 showing increasing perturbation and derivative amplitudes toward the lower MLAT end of the  
548 range of available stations, we consider it to be likely that these bays and their associated large  
549 MPEs may have extended even farther equatorward.

550         The pre- and post-midnight MPEs also differed in the directions of their largest  
551 perturbations. Pre-midnight MPEs were often largest in the Bx component, with some largest in  
552 Bz but with By largest at only one station (out of 37) in all 3 events. In contrast, post-midnight

553 MPEs were most often largest in the By component. This difference is consistent with earlier  
554 observations reported by Viljanen et al. (2001), who noted the strong southward direction of  
555 magnetic field fluctuations for large events in the auroral zone midnight sector, compared to a  
556 more East–West alignment in the morning sector.

557 Many of the nighttime MPEs in intervals 1 and 2 occurred simultaneously to within 1-2  
558 minutes in latitudinal ranges of 300-700 km in conjugate hemispheres. The MPEs in interval 3  
559 exhibited more significant differences between hemispheres, but these may have been caused by  
560 the greater longitudinal separation between available conjugate stations during this interval.  
561 Although it might be expected that magnetic perturbations in high latitude regions should show  
562 some symmetry (or at least some form of direct control of asymmetry by the orientation of the  
563 interplanetary magnetic field, season, or ionospheric conductivity), Kim et al. (2013)  
564 documented that this is seldom true for dayside magnetic impulse events (the high latitude  
565 geomagnetic response to sudden changes in solar wind pressure). They suggested that these  
566 asymmetric dayside ground responses might be of local origin rather than magnetospheric origin.

567

## 568 5.1 Connection to omega bands and their physical mechanisms

569 Because only magnetometer data are utilized in this study, we have no additional  
570 information about auroral phenomena that might contribute to the causal chain leading to these  
571 events, as was provided for the 3 events presented by Engebretson et al. (2019b). That study  
572 included a SECS (spherical elementary current systems) analysis using a large 2-d set of  
573 magnetometers across North America and Greenland (Weygand et al., 2011) as well as auroral  
574 snapshots from the THEMIS all-sky imager array and GOES 13 dipolarization data. However,  
575 we comment briefly on the post-midnight interval and explore why we link it to the occurrence  
576 and physics of omega bands.

577 Opgenoorth et al. (1983) characterized the source of omega bands as a “meandering”  
578 ionospheric Hall current, composed of a westward background electrojet and circular Hall  
579 current vortices around the locations of localized field-aligned currents, and Opgenoorth et al.  
580 (1994) equivalently described them as “large-scale auroral vortex streets.” Omega bands have  
581 also been closely associated with long period irregular Pi3 or Ps6 magnetic pulsations with  
582 periods of 5 – 15 min (e.g., Kawasaki and Rostoker, 1979; Andre and Baumjohann, 1982;  
583 Solovyev et al., 1999; Henderson et al., 2002, and Wild et al., 2011). Apatenkov et al. (2020)

584 provided detailed observations of a very large GIC that was associated with an interval of omega  
585 bands. They modeled this event using the sum of two basic current systems: a 1D linear current  
586 (mimicking the auroral electrojet) and a 2D vortex that passed eastward over the field of view of  
587 the ground magnetometers. As a result of pointing out that the magnetic field created by  
588 ionospheric and magnetospheric currents may vary due to both temporal changes of current  
589 amplitudes and to the motion of the current structures, they suggested that propagating  
590 nonexplosive and relatively long-lived structures might be responsible for large rapid magnetic  
591 field variations if their propagation speeds were sufficiently large.

592 The magnetospheric source of these currents may be, as Partamies et al. (2017) and  
593 Weygand et al. (2015) have suggested, fast earthward flows in the magnetotail, e.g., bursty bulk  
594 flows (BBFs, Angelopoulos et al., 1992) or the more localized dipolarizing flux bundles (DFBs)  
595 described by Liu et al. (2014). Palin et al. (2015) found that highly localized FACs and  
596 ionospheric currents were associated with BBFs and/or dipolarizing flux bundles observed by  
597 THEMIS spacecraft in the near magnetotail, and suggested that these might be the smallest  
598 elements of substorms and pseudobreakups. A recent satellite-ground study by Liu et al. (2018)  
599 also found that omega bands are related to a flow shear near the inner edge of the plasma sheet,  
600 and suggested that an enhanced flow in the magnetosphere drives the omega bands by triggering  
601 plasma instabilities. Within a BBF, the flow velocity exhibits peaks of very large amplitude with  
602 a characteristic time scale of the order of a minute, which are usually associated with magnetic  
603 field dipolarizations and ion temperature increases.

604 Although mid- or small-scale magnetotail flows are likely the ultimate sources for the  
605 field-aligned and ionospheric currents that generate nighttime MPEs, the contrast between the  
606 highly localized nature of the MPEs at each station observed during the post-midnight event and  
607 the larger-scale synchronicity of MPEs observed during the three pre-midnight events suggests  
608 that even smaller-scale magnetosphere-ionosphere coupling processes and resulting plasma  
609 instabilities may play a significant role in generating post-midnight MPEs. We note that Sato et  
610 al. (2017) similarly concluded their study of omega bands by strongly suggesting that  
611 magnetosphere-ionosphere coupling should play an important role in the formation of omega  
612 band auroras.

613

## 614 **6. Summary and Conclusions**

615 Under both quiet and moderately disturbed geomagnetic conditions large pre-midnight  
616 MPEs at high magnetic latitudes exhibited fair to good hemispheric conjugacy in the timing of  
617 the equatorward excursion of their N-S component ( $\Delta B_x$ ) and fair conjugacy in their latitudinal  
618 profiles and amplitude peaks. During interval 3, which occurred during a highly disturbed  
619 interval, there was little similarity in MPE occurrence or amplitude between hemispheres, but the  
620 MPE appeared to be highly localized in both latitude and longitude, and available stations in  
621 opposite hemispheres were separated in longitude. Although the opposite orientation of the  $\Delta B_y$   
622 perturbations in conjugate hemispheres was consistent with Hall currents surrounding localized  
623 FACs, the shapes of the perturbations in the  $B_y$  and  $B_z$  components were rarely similar in  
624 conjugate hemispheres.

625 The  $\Delta B_x$  amplitude was largest in the winter hemisphere during 3 of the 4 intervals  
626 presented here, and comparison of conjugate amplitudes and modeled ionospheric conductances  
627 suggested that the MPEs were fit much better by a current generator model than by a voltage  
628 generator model. However, during near-equinox interval 2 the  $\Delta B_x$  amplitudes were strongest  
629 in the southern hemisphere, and neither a simple current or voltage generator model was  
630 consistent with these amplitudes. In addition, a conductance model including auroral  
631 precipitation effects may suggest that the MPEs observed in this study occurred at or poleward of  
632 the poleward edge of the auroral zone, consistent with the multi-instrument MPE case studies of  
633 Engebretson et al. (2019b).

634 These large nighttime MPEs occurred under a range of solar wind and IMF conditions,  
635 but common to all four intervals was a negative IMF  $B_z$  that exhibited at least a modest increase  
636 at or near the time of the event.

637 Large  $dB/dt$  values occurred both pre- and post-midnight. During the 3 pre-midnight  
638 events they were usually isolated and were largest in the X and Z components and smallest in Y  
639 at all but one station in one pre-midnight event. During the post-midnight interval they were  
640 grouped in quasi-periodic patterns embedded within a large magnetic bay, and the largest values  
641 occurred more often in the Y component than in X or Z.

642 The local time range of the more clearly impulsive events matches that of BBFs and/or  
643 dipolarizing flux bundles, while the range of the dawn sector events matches that of omega  
644 bands. These results may indicate that two separate and highly localized magnetosphere-

645 ionosphere coupling mechanisms may be responsible for generating the large, rapid geomagnetic  
646 perturbations that generate GICs.

647

## 648 **Acknowledgements**

649 This work was supported by National Science Foundation grants AGS-1651263 to  
650 Augsburg University, AGS-1654044 to the University of Michigan, OPP-1744828 to Virginia  
651 Tech, and OPP-1643700 to the New Jersey Institute of Technology; and Natural Environmental  
652 Research Council grant NE/R016038/1 to the British Antarctic Survey. HO and AS thank the  
653 National Swedish Space Agency (SNSA) for support.

654 Solar wind and IMF data are available at the Goddard Space Flight Center Space Physics  
655 Data Facility at <https://cdaweb.sci.gsfc.nasa.gov/index.html/>, as are also data from the Greenland  
656 West Coast magnetometer chain. MACCS and CANMOS magnetometer data are available in  
657 IAGA 2002 ASCII format at <http://space.augsburg.edu/maccs/requestdatafile.jsp> and  
658 <http://geomag.nrcan.gc.ca/data-donnee/sd-en.php>, respectively. South Pole Station  
659 magnetometer data are available in ASCII format at <https://antarcticgeospace.njit.edu/Data/>.  
660 AAL-PIP magnetometer data are available in CDF and IDL save set formats at  
661 <http://mist.nianet.org/> and in ASCII format at <https://cdaweb.gsfc.nasa.gov>. BAS LPM  
662 magnetometer data are available at [https://data.bas.ac.uk/full-  
663 record.php?id=GB/NERC/BAS/AEDC/00263](https://data.bas.ac.uk/full-record.php?id=GB/NERC/BAS/AEDC/00263).

664 The SML and SMU indices are available at <http://supermag.jhuapl.edu/indices/>, and the  
665 SuperMAG substorm database is available at <http://supermag.jhuapl.edu/substorms/>. Jesper  
666 Gjerloev is SuperMAG Principal Investigator. These SuperMAG products are derived from  
667 magnetometer data from INTERMAGNET, Alan Thomson; USGS, Jeffrey J. Love; CARISMA,  
668 PI Ian Mann; CANMOS, Geomagnetism Unit of the Geological Survey of Canada; The S-  
669 RAMP Database, PI K. Yumoto and Dr. K. Shiokawa; The SPIDR database; AARI, PI Oleg  
670 Troshichev; The MACCS program, PI M. Engebretson; GIMA; MEASURE, UCLA IGPP and  
671 Florida Institute of Technology; SAMBA, PI Eftyhia Zesta; 210 Chain, PI K. Yumoto;  
672 SAMNET, PI Farideh Honary; IMAGE, PI Liisa Juusola; Finnish Meteorological Institute, PI  
673 Liisa Juusola; Sodankylä Geophysical Observatory, PI Tero Raita; UiT the Arctic University of  
674 Norway, Tromsø Geophysical Observatory, PI Magnar G. Johnsen; GFZ German Research  
675 Centre For Geosciences, PI Jürgen Matzka; Institute of Geophysics, Polish Academy of

676 Sciences, PI Anne Neska and Jan Reda; Polar Geophysical Institute, PI Alexander Yahnin and  
677 Yaroslav Sakharov; Geological Survey of Sweden, PI Gerhard Schwarz; Swedish Institute of  
678 Space Physics, PI Masatoshi Yamauchi; AUTUMN, PI Martin Connors; DTU Space, PI Dr.  
679 Thom R. Edwards and Anna Willer; PENGUIn; South Pole and McMurdo Magnetometer, PIs  
680 Louis J. Lanzerotti and Allan T. Weatherwax; ICESTAR; RAPIDMAG; British Antarctic  
681 Survey; McMAC, PI Dr. Peter Chi; BGS, PI Dr. Susan Macmillan; Pushkov Institute of  
682 Terrestrial Magnetism, Ionosphere and Radio Wave Propagation (IZMIRAN);; MFGL, PI B.  
683 Heilig; Institute of Geophysics, Polish Academy of Sciences, PI Anne Neska and Jan Reda; and  
684 University of L'Aquila, PI M. Vellante; BCMT, V. Lesur and A. Chambodut; Data obtained in  
685 cooperation with Geoscience Australia, PI Marina Costelloe; AALPIP, co-PIs Bob Clauer and  
686 Michael Hartinger; SuperMAG; Data obtained in cooperation with the Australian Bureau of  
687 Meteorology, PI Richard Marshall.

688

## 689 **References**

690

691 André, D., and W. Baumjohann (1982), Joint two-dimensional observations of ground magnetic  
692 and ionospheric electric fields associated with auroral currents. 5. Current system  
693 associated with eastward drifting omega bands, *Journal of Geophysics*, 50, 194–201,  
694 <https://journal.geophysicsjournal.com/JofG/article/view/201>.

695 Angelopoulos, V., W. Baumjohann, C. F. Kennel, F. V. Coroniti, M. G. Kivelson, R. Pellat, R. J.  
696 Walker, H. Luehr, and G. Paschmann, (1992), Bursty bulk flows in the inner central  
697 plasma sheet. *Journal of Geophysical Research*, 97, 4027–4039, doi:10.1029/91JA02701

698 Apatenkov, S. V., V. A. Sergeev, R. Pirjola, and A. Viljanen (2004), Evaluation of the geometry  
699 of ionospheric current systems related to rapid geomagnetic variations, *Annales*  
700 *Geophysicae*, 22, 63-72, doi:10.5194/angeo-22-63-2004

701 Apatenkov, S. V., Pilipenko, V. A., Gordeev, E. I., Viljanen, A., Juusola, L., Belakhovsky, V.  
702 B., Sakharov, Ya. A., and Selivanov, V. N. (2020), Auroral omega bands are a significant  
703 cause of large geomagnetically induced currents, *Geophysical Research Letters*, 47,  
704 e2019GL086677, doi:10.1029/2019GL086677

705 Belakhovsky, V., V. Pilipenko, M. Engebretson, Ya. Sakharov, and V. Selivanov (2019),

706 Impulsive disturbances of the geomagnetic field as a cause of induced currents of electric

707 power lines, *Journal of Space Weather and Space Climate*, 9, A18,  
708 doi:10.1051/swsc/2019015

709 Clauer, C. R., H. Kim, K. Deshpande, Z. Xu, D. Weimer, S. Musko, G. Crowley, C. Fish, R.  
710 Nealy, T. E. Humphreys, J. A. Bhatti, and A. J. Ridley (2014), An autonomous adaptive  
711 low-power instrument platform (AAL-PIP) for remote high-latitude geospace data  
712 collection, *Geosci. Instrum. Method. Data Syst.*, 3, 211–227, doi:10.5194/gi-3-211-2014

713 Cousins, E. D. P., T. Matsuo, and A. D. Richmond (2015), Mapping high-latitude ionospheric  
714 electrodynamics with SuperDARN and AMPERE, *J. Geophys. Res. Space Physics*, 120,  
715 5854–5870, doi:10.1002/2014JA020463

716 Dimmock, A. P., L. Rosenqvist, J-O. Hall, A. Viljanen, E. Yordanova, I. Honkonen, M. André,  
717 and E. C. Sjöberg (2019), The GIC and geomagnetic response over Fennoscandia to the  
718 7-8 September 2017 geomagnetic storm, *Space Weather*, 17, 989–1010,  
719 <https://doi.org/10.1029/2018SW002132>

720 Engebretson, M. J., W. J. Hughes, J. L. Alford, E. Zesta, L. J. Cahill, Jr., R. L. Arnoldy, and G.  
721 D. Reeves (1995), Magnetometer array for cusp and cleft studies observations of the  
722 spatial extent of broadband ULF magnetic pulsations at cusp/cleft latitudes, *Journal of*  
723 *Geophysical Research*, 100, 19371-19386, doi:10.1029/95JA00768

724 Engebretson, M. J., Araki, T., Arnoldy, R. L., Carpenter, D. L., Doolittle, J. H., Fukunishi, H., et  
725 al. (1997), The United States automatic geophysical observatory (AGO) program in  
726 Antarctica, in M. Lockwood, M. N. Wild, & H. J. Opgenoorth (Eds.), *the Satellite—*  
727 *Ground Based Coordination Sourcebook*, ESA-SP-1198 (pp. 65–99). ESTEC, Noordwijk,  
728 Netherlands: ESA Publications.

729 Engebretson, M. J., Pilipenko, V. A., Ahmed, L. Y., Posch, J. L., Steinmetz, E. S., Moldwin, M.  
730 B., Connors, M. G., Weygand, J. M., Mann, I. R., Boteler, D. H., Russell, C. T., and  
731 Vorobev, A. V. (2019a), Nighttime magnetic perturbation events observed in Arctic  
732 Canada: 1. Survey and statistical analysis, *Journal of Geophysical Research: Space*  
733 *Physics*, 124, 7442-7458, doi:10.1029/2019JA026794

734 Engebretson, M. J., E. S. Steinmetz, J. L. Posch, V. A. Pilipenko, M. B. Moldwin, M. G.  
735 Connors, D. H. Boteler, I. R. Mann, M. D. Hartinger, J. M. Weygand, L. R. Lyons, Y.  
736 Nishimura, H. J. Singer, S. Ohtani, C. T. Russell, A. Fazakerley, and L. M. Kistler  
737 (2019b), Nighttime magnetic perturbation events observed in Arctic Canada: 2.

738 Multiple-instrument observations, *Journal of Geophysical Research: Space Physics*, 124,  
739 7459-7476, doi:10.1029/2019JA026797

740 Gabrielse, C., V. Angelopoulos, A. Runov, and D. L. Turner (2014), Statistical characteristics of  
741 particle injections throughout the equatorial magnetotail, *Journal of Geophysical*  
742 *Research: Space Physics*, 119, 2512–2535, doi:10.1002/2013JA019638

743 Henderson, M. G., Reeves, G. D., and Murphree, J. S. (1998), Are north-south aligned auroral  
744 structures an ionospheric manifestation of bursty bulk flows?, *Geophysical Research*  
745 *Letters*, 25, 3737–3740, doi:10.1029/98GL02692

746 Henderson, M. G., Kepko, L., Spence, H. E., Connors, M., Sigwarth, J. B., Frank, L. A., Singer,  
747 H.,J., and Yumoto, K. (2002), The evolution of north-south aligned auroral forms into  
748 auroral torch structures: The generation of omega bands and Ps6 pulsations via flow  
749 bursts, in the *Proceedings of the Sixth International Conference on Substorms*, edited by  
750 R. M. Winglee, University of Washington, Seattle, WA, ISBN:0971174032  
751 9780971174030

752 Kadokura, A., H. Yamagishi, N. Sato, K. Nakano, and M. C. Rose (2008), Unmanned  
753 magnetometer network observation in the 44<sup>th</sup> Japanese Antarctic Research Expedition:  
754 Initial results and an event study on auroral substorm evolution, *Polar Science* 2, 223-  
755 235, doi:10.1016/j.polar.2008.04.002

756 Kauristie, K., Sergeev, V. A., Kubyshkina, M., Pulkkinen, T. I., Angelopoulos, V., Phan, T., Lin,  
757 R. P., and Slavin, J. A. (2000), Ionospheric current signatures of transient plasma sheet  
758 flows, *Journal of Geophysical Research*, 105, 10,677–10,690,  
759 doi:10.1029/1999JA900487

760 Kawasaki, K., and Rostoker, G. (1979), Perturbation magnetic fields and current systems  
761 associated with eastward drifting auroral structures, *Journal of Geophysical Research*,  
762 84, 1464–1480, doi:10.1029/JA084iA04p01464

763 Kim, H., X. Cai, C. R. Clauer, B. S. R. Kunduri, J. Matzka, C. Stolle, and D. R. Weimer (2013),  
764 Geomagnetic response to solar wind dynamic pressure impulse events at high-latitude  
765 conjugate points, *J. Geophys. Res. Space Physics*, 118, 6055–6071,  
766 doi:10.1002/jgra.50555.

767 Kozyreva, O. V., V. A. Pilipenko, V. B. Belakhovsky, and Ya. A. Sakharov (2018), Ground  
768 geomagnetic field and GIC response to March 17, 2015 storm, *Earth, Planets and Space*,

769 70:157, doi:10.1186/s40623-018-0933-2

770 Lanzerotti, L. J., A. Wolfe, N. Trivedi , C. G. MacLennan, and L. V. Medford (1990), Magnetic  
771 impulse events at high latitudes: Magnetopause and boundary layer plasma processes,  
772 *Journal of Geophysical Research*, 95, 97-107, doi:10.1029/JA095iA01p00097

773 Liou, K., T. Sotirelis, and E. J. Mitchell (2018), North-south asymmetry in the geographic  
774 location of auroral substorms correlated with ionospheric effects, *Scientific Reports*, 8,  
775 17230, doi:10.1038/s41598-018-35091-2

776 Liu, J., V. Angelopoulos, X.-Z. Zhou, and A. Runov (2014), Magnetic flux transport by  
777 dipolarizing flux bundles, *Journal of Geophysical Research: Space Physics*, 119, 909–  
778 926, doi:10.1002/2013JA019395

779 Liu, J., L. R. Lyons, W. E. Archer, B. Gallardo-Lacourt, Y. Nishimura, Y. Zou, C. Gabrielse, and  
780 J. M. Weygand (2018), Flow shears at the poleward boundary of omega bands observed  
781 during conjunctions of Swarm and THEMIS ASI, *Geophysical Research Letters*, 45,  
782 1218–1227, doi:10.1002/2017GL076485

783 Lyons, L. R., Nishimura, Y., Xing, X., Runov, A., Angelopoulos, V., Donovan, E., and Kikuchi,  
784 T. (2012), Coupling of dipolarization front flow bursts to substorm expansion phase  
785 phenomena within the magnetosphere and ionosphere, *Journal of Geophysical Research*,  
786 117, A02212, doi:10.1029/2011JA017265

787 Lysak, R. L. (1990), Electrodynamic coupling of the magnetosphere and ionosphere, *Space*  
788 *Science Reviews*, 52, 33–87, doi:10.1007/BF00704239

789 Mravlag, E., Scourfield, M. W. J., Walker, A. D. M., Sutcliffe, P. R., and Nielsen, E. (1991),  
790 Simultaneous observations of omega band related phenomena in both hemispheres,  
791 *Journal of Atmospheric and Terrestrial Physics*, 53, 309–317, doi:10.1016/  
792 0021-9169(91)90114-m

793 Newell, P. T., T. Sotirelis, and S. Wing (2009), Diffuse, monoenergetic, and broadband aurora:  
794 The global precipitation budget, *Journal of Geophysical Research*, 114, A09207,  
795 doi:10.1029/2009JA014326.

796 Newell, P. T., T. Sotirelis, and S. Wing (2010), Seasonal variations in diffuse, monoenergetic,  
797 and broadband aurora, *Journal of Geophysical Research*, 115, A03216,  
798 doi:10.1029/2009JA014805.

799 Newell, P. T., and J. W. Gjerloev (2011), Evaluation of SuperMAG auroral electrojet indices as

800 indicators of substorms and auroral power, *Journal of Geophysical Research*, 116,  
801 A12211, doi:10.1029/2011JA016779

802 Newell, P. T., Liou, K., Zhang, Y., Sotirelis, T., Paxton, L. J., and Mitchell, E. J. (2014),  
803 OVATION Prime-2013: Extension of auroral precipitation model to higher disturbance  
804 levels, *SpaceWeather*, 12, 368–379, doi:10.1002/2014SW001056

805 Ngwira, C. M., A. A. Pulkkinen, E. Bernabeu, J. Eichner, A. Viljanen, and G. Crowley (2015),  
806 Characteristics of extreme geoelectric fields and their possible causes: Localized peak  
807 enhancements, *Geophysical Research Letters*, 42, 6916–6921,  
808 doi:10.1002/2015GL065061

809 Ngwira C. M., D. G. Sibeck, M. D. V. Silveira, M. Georgiou, J. M. Weygand, Y. Nishimura, and  
810 D. Hampton (2018), A study of intense local  $dB/dt$  variations during two geomagnetic  
811 Storms, *Space Weather*, 16, 676–693, doi:10.1029/2018SW001911.

812 Ngwira, C. M., and A. A. Pulkkinen (2019), An introduction to geomagnetically induced  
813 currents (2019), in *Geomagnetically Induced Currents from the Sun to the Power Grid*,  
814 Geophysical Monograph Series, 244, edited by J. L. Gannon, A. Swidinsky, and Z. Xu,  
815 American Geophysical Union, Washington, D.C., 3-14, doi:10.1002/9781119434412.ch1

816 Nikitina, L., Trichtchenko, L., and Boteler, D. H. (2016), Assessment of extreme values in  
817 geomagnetic and geoelectric field variations for Canada. *Space Weather*, 14, 481–494,  
818 doi:10.1002/2016SW001386

819 Opgenoorth, H. J., Oksman, J., Kaila, K. U., Nielsen, E., and Baumjohann, W. (1983),  
820 Characteristics of eastward drifting omega bands in the morning sector of the auroral  
821 oval, *Journal of Geophysical Research*, 88, 9171–9185, doi:10.1029/JA088iA11p09171

822 Opgenoorth, H. J., M. A. L. Persson, T. I. Pulkkinen, and R. J. Pellinen (1994), Recovery phase  
823 of magnetospheric substorms and its association with morning-sector aurora, *Journal of*  
824 *Geophysical Research*, 99, 4115–4129, doi:10.1029/93JA01502

825 Palin, L., C. Jacquey, H. Opgenoorth, M. Connors, V. Sergeev, J.-A. Sauvaud, R. Nakamura,  
826 G. D. Reeves, H. J. Singer, V. Angelopoulos, and L. Turc (2015), Three-dimensional  
827 current systems and ionospheric effects associated with small dipolarization fronts, *J.*  
828 *Geophys. Res. Space Physics*, 120, 3739–3757, doi:10.1002/2015JA021040

829 Partamies, N., Weygand, J. M., and Juusola, L. (2017), Statistical study of auroral omega bands,  
830 *Annales Geophysicae*, 35, 1069–1083, doi:10.5194/angeo-35-1069-2017

831 Pilipenko, V. A., Fedorov, E. N., Hartinger, M. D., and Engebretson, M. J. (2019),  
832 Electromagnetic fields of magnetospheric ULF disturbances in the ionosphere:  
833 Current/voltage Dichotomy, *Journal of Geophysical Research: Space Physics*, 124, 109–  
834 121, doi:10.1029/2018JA026030

835 Pulkkinen, A., E. Bernabeu, J. Eichner, A. Viljanen, and C. Ngwira (2015), Regional-scale high-  
836 latitude extreme geoelectric fields pertaining to geomagnetically induced currents, *Earth,*  
837 *Planets, and Space*, 67, 93, doi:10.1186/s40623-015-0255-6

838 Robinson, R. M., R. R. Vondrak, K. Miller, T. Dabbs, and D. Hardy (1987), On calculating  
839 ionospheric conductances from the flux and energy of precipitating electrons, *Journal of*  
840 *Geophysical Research*, 92, 2565–2569, doi:10.1029/JA092iA03p02565

841 Sato, N., Yukimatu, A. S., Tanaka, Y., and Hori, T. (2017), Morphologies of omega band  
842 auroras, *Earth, Planets and Space*, 69, 103,

843 Sergeev, V. A., Liou, K., Meng, C.-I., Newell, P. T., Brittnacher, M., Parks, G., and Reeves, G.  
844 D, (1999), Development of auroral streamers in association with localized impulsive  
845 injections to the inner magnetotail, *Geophysical Research Letters*, 26, 417–420,  
846 doi:10.1029/1998GL900311

847 Solovyev, S. I., Baishev, D. G., Barkova, E. S., Engebretson, M. J., Posch, J. L., Hughes, W. J.,  
848 Yumoto, K., and Pilipenko, V. A. (1999), Structure of disturbances in the dayside and  
849 nightside ionosphere during periods of negative interplanetary magnetic field Bz, *Journal*  
850 *of Geophysical Research*, 104, 28,019–28,039, doi:10.1029/1999JA900286

851 Viljanen A. (1997), The relation between geomagnetic variations and their time derivatives and  
852 implications for estimation of induction risks, *Geophysical Research Letters*, 24, 631-  
853 634, doi:10.1029/97GL00538

854 Viljanen, A., Nevanlinna, H., Pajunpää, K., and Pulkkinen, A. (2001), Time derivative of the  
855 horizontal geomagnetic field as an activity indicator, *Annales Geophysicae*, 19(9), 1107–  
856 1118, doi:10.5194/angeo-19-1107-2001

857 Viljanen, A., E. I. Tanskanen, and A. Pulkkinen (2006), Relation between substorm  
858 characteristics  
859 and rapid temporal variations of the ground magnetic field, *Annales Geophysicae*, 24,  
860 725-  
861 733, doi:10.5194/angeo-24-725-2006.

862 Viljanen, A., and Tanskanen, E. (2011), Climatology of rapid geomagnetic variations at high  
863 latitudes over two solar cycles, *Annales Geophysicae*, 29, 1783–1792,  
864 doi:10.5194/angeo-29-1783-2011

865 Weygand, J. M., O. Amm, A. Viljanen, V. Angelopoulos, D. Murr, M. J. Engebretson et al.  
866 (2011), Application and validation of the spherical elementary currents systems technique  
867 for deriving ionospheric equivalent currents with the North American and Greenland  
868 ground magnetometer arrays, *Journal of Geophysical Research*, 116, A03305,  
869 doi:10.1029/2010JA016177

870 Weygand, J. M., Kivelson, M. G., Frey, H. U., Rodriguez, J. V., Angelopoulos, V., Redmon, R.,  
871 and Amm, O. (2015), An interpretation of spacecraft and ground based observations of  
872 multiple omega band events, *Journal of Atmospheric and Solar-Terrestrial Physics*, 133,  
873 185–204, doi:10.1016/j.jastp.2015.08.014

874 Wild, J. A., Woodfield, E. E., Donovan, E., Fear, R. C., Grocott, A., Lester, M., Fazakerley, A.  
875 N., Lucek, E., Khotyaintsev, Y., Andre, M., Kadokura, A., Hosokawa, K., Carlson, C.,  
876 McFadden, J. P., Glassmeier, K. H., Angelopoulos, V., and Björnsson, G. (2011),  
877 Midnight sector observations of auroral omega bands, *Journal of Geophysical Research*,  
878 116, A00130, doi:10.1029/2010JA015874

879 Zesta, E., Lyons, L., and Donovan, E. (2000), The auroral signature of Earthward flow bursts  
880 observed in the magnetotail, *Geophysical Research Letters*, 27, 3241–3244,  
881 doi:10.1029/2000GL000027

882 Zesta, E., Lyons, L., Wang, C.-P., Donovan, E., Frey, H., and Nagai, T. (2006), Auroral  
883 poleward boundary intensifications (PBIs): Their two-dimensional structure and  
884 associated dynamics in the plasma sheet, *Journal of Geophysical Research*, 111, A05201,  
885 doi:10.1029/2004JA010640

886  
887  
888  
889  
890  
891  
892

893

894

895

896  
 897  
 898  
 899  
 900  
 901  
 902  
 903  
 904  
 905  
 906  
 907  
 908  
 909  
 910  
 911  
 912  
 913  
 914  
 915  
 916  
 917  
 918  
 919  
 920  
 921  
 922  
 923  
 924  
 925  
 926  
 927  
 928

Table 1. Magnetometer Stations Used in This Study

Northern Hemisphere					Southern Hemisphere				
Array	Geogr Lat	Geogr Lon	CGM Lat	CGM Lon	Array	Geogr Lat	Geogr Lon	CGM Lat	CGM Lon
MACCS									
Pangnirtung	66.1°	294.2°	73.2°	19.8°	South Pole	-90.00 °	--	-74.5°	18.7°
CANMOS									
Iqaluit	63.8°	291.5°	71.4°	15.2°	AAL-PIP				
Greenland Coastal Chain					PG0	-83.67°	88.68°	-78.7°	38.2°
THL	77.47°	290.77°	84.0°	26.4°	PG1	-84.50°	77.20°	-77.3°	37.3°
TAB	76.54°	291.18°	83.2°	25.0°	PG2	-84.42°	57.95°	-75.7°	39.1°
SVS	76.02°	294.90°	82.3°	30.4°	PG3	-84.81°	37.63°	-73.9°	36.7°
KUV	74.57°	302.82°	80.0°	39.4°	PG4	-83.34°	12.25°	-71.2°	36.4°
UPN	72.78°	303.85°	78.2°	38.1°	PG5	-81.96°	5.71°	-69.9°	37.2°
UMQ	70.68°	307.87°	75.7°	40.8°	British Antarctic Survey Low Power Magnetometer Chain				
GDH	69.25°	306.47°	74.5°	37.8°	M85-002	-85.36°	2.06°	-71.8°	30.1°
ATU	67.93°	306.43°	73.2°	36.8°	M84-336	-84.36°	-23.85°	-69.8°	25.9°
STF	67.02°	309.28°	71.9°	39.5°	M83-348	-82.90°	-12.25°	-69.2°	30.6°
SKT	65.42°	307.10°	70.7°	36.1°	M81-338	-80.89°	-22.25°	-67.0°	29.2°
GHB	64.17°	308.27°	69.2°	36.8°	M79-336	-79.68°	-24.12°	-66.0°	29.3°
FHB	62.00°	310.32°	66.6°	38.1°	M78-337	-77.52°	-23.42°	-64.3°	30.7°
NAQ	61.16°	314.56°	65.0°	42.3°					

Note: Corrected geomagnetic (CGM) coordinates were calculated for epoch 2016 (using [http://sdnet.thayer.dartmouth.edu/aacgm/aacgm\\_calc.php#AACGM](http://sdnet.thayer.dartmouth.edu/aacgm/aacgm_calc.php#AACGM)).

929 Table 2. The maximum |dB/dt| values for each component for each of the stations shown during  
 930 each of the intervals presented here.

931

932 Station	15 Jan 2018	16 Mar 2018	8 May 2016	13 May 2015
933 SPA	-15.1, -, -	7.5,-12.1, 4.9		-3.3, -, -
934 PGG	-9.1, 5.7, 4.3	-6.3, 3.3, 4.4		3.2, 2.5, 1.9
935 IQA		2.0, 1.7, 2.0		-3.8, 3.4, 4.9
936				
937 PG2	4.9, 2.6, -3.1	4.2, -3.3, 3.8		-3.6, 4.3, 2.7
938 PG3	-8.1, 6.4, -9.8	8.6, 4.2, 4.8		5.4, -3.4, -5.7
939 PG4		-13.2,-11.4, 13.6		5.2, 5.2, -6.1
940 PG5	-8.0, 5.5, 7.8	-16.2, 13.3,-12.0		
941 M85				3.2, 1.9, 1.9
942 M84		-25.7, 12.7, 5.2		
943 M83				7.7, 6.7, 4.2
944 M81		15.6, 8.6, 9.6	-12.9, -3.2, -4.0	-7.7,-10.7,-6.1
945 M79	3.4, -2.3, 1.2	15.8, 6.3, 3.4	37.7, 13.7, 19.5	
946 M78	4.5, 3.8, -3.3		14.4, 9.1, 10.3	
947				
948 UMQ	-8.8, 3.8, 4.9			2.1, 1.5, 1.6
949 GDH	-10.0,-10.6,-12.7	3.0, 2.2, -4.5		-2.8, 1.6, 2.0
950 STF	-12.8, -7.0, -8.9	-7.2, -5.6, -7.1		3.1, 6.0, -3.7
951 SKT		-6.4,-4.7, 9.8		2.9, 6.3, 6.3
952 GHB	-4.5, 5.0, -8.3	-8.1, -5.9, -	-2.4, 1.6, -	3.4, 7.0, -5.9
953 FHB	3.2, 3.5, -4.6	6.6, -3.0, 5.8	-6.7, 6.5, -9.6	-4.7, 7.0, -8.1
954 NAQ	4.3, 2.1, -2.2	-3.8, -3.0, -3.3	-7.5, -6.5, -6.4	-9.2, 10.5, -5.3

955

956

957

958

959

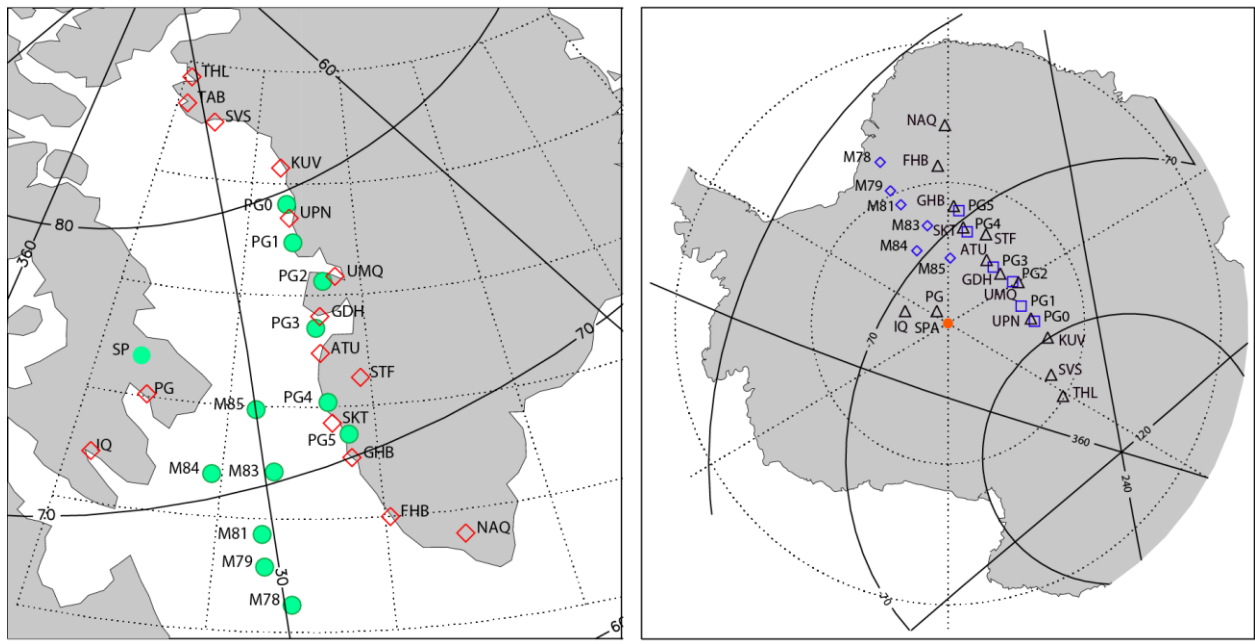
960

961 Table 3. Half-amplitude latitudinal and longitudinal falloff distances between adjacent station  
 962 pairs for the MPE occurring near 2105 UT on 8 May 2016 in Antarctica and Greenland,  
 963 respectively.

964

965	BAS LPM	Greenland	BAS LPM – Greenland Conjugate
966	M81 – M79 106 km	GHB – FHB 204 km	M81 – FHB 446 km
967	M81 – M79 192 km		M79 – FHB 262 km

968



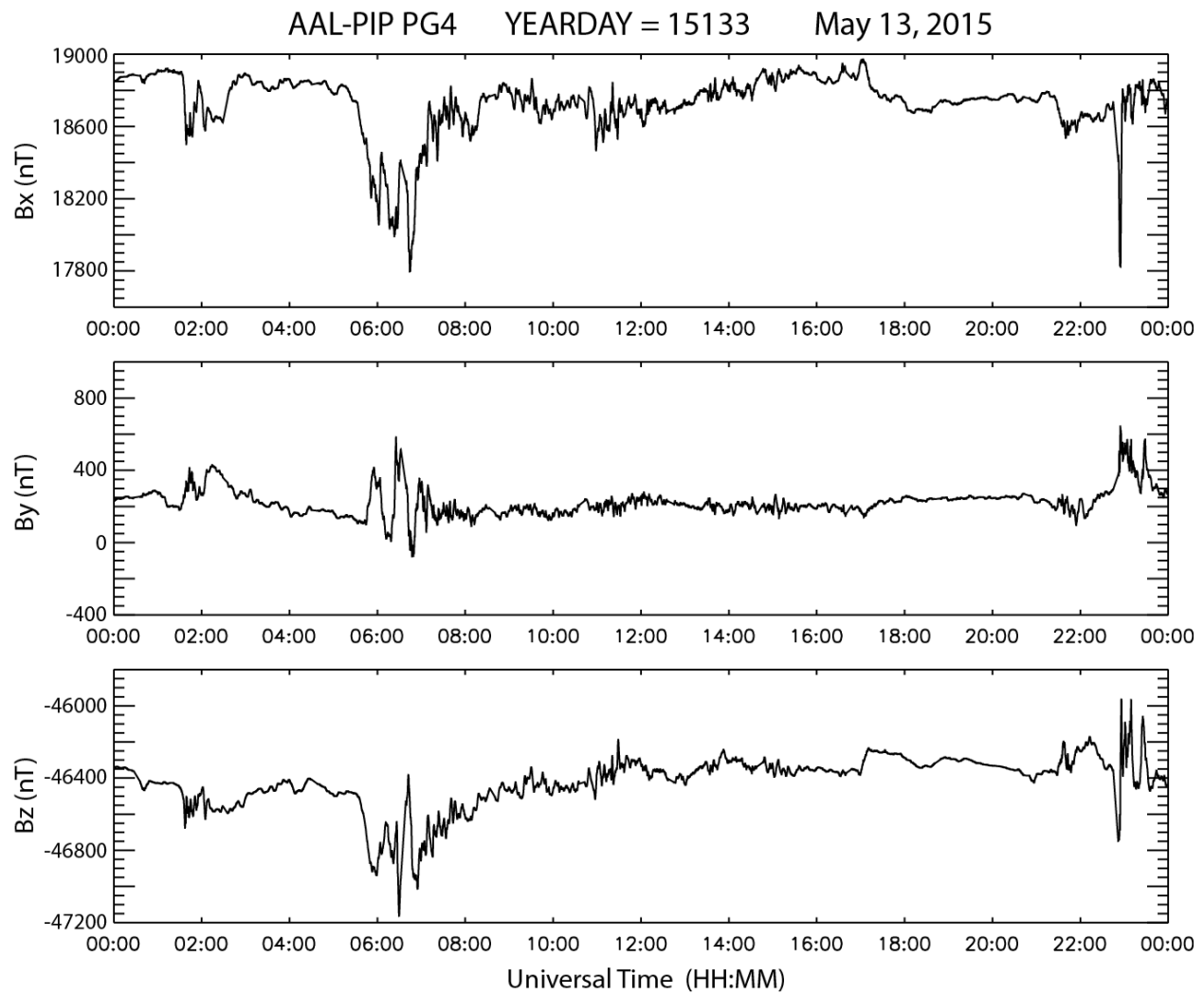
970

971

972

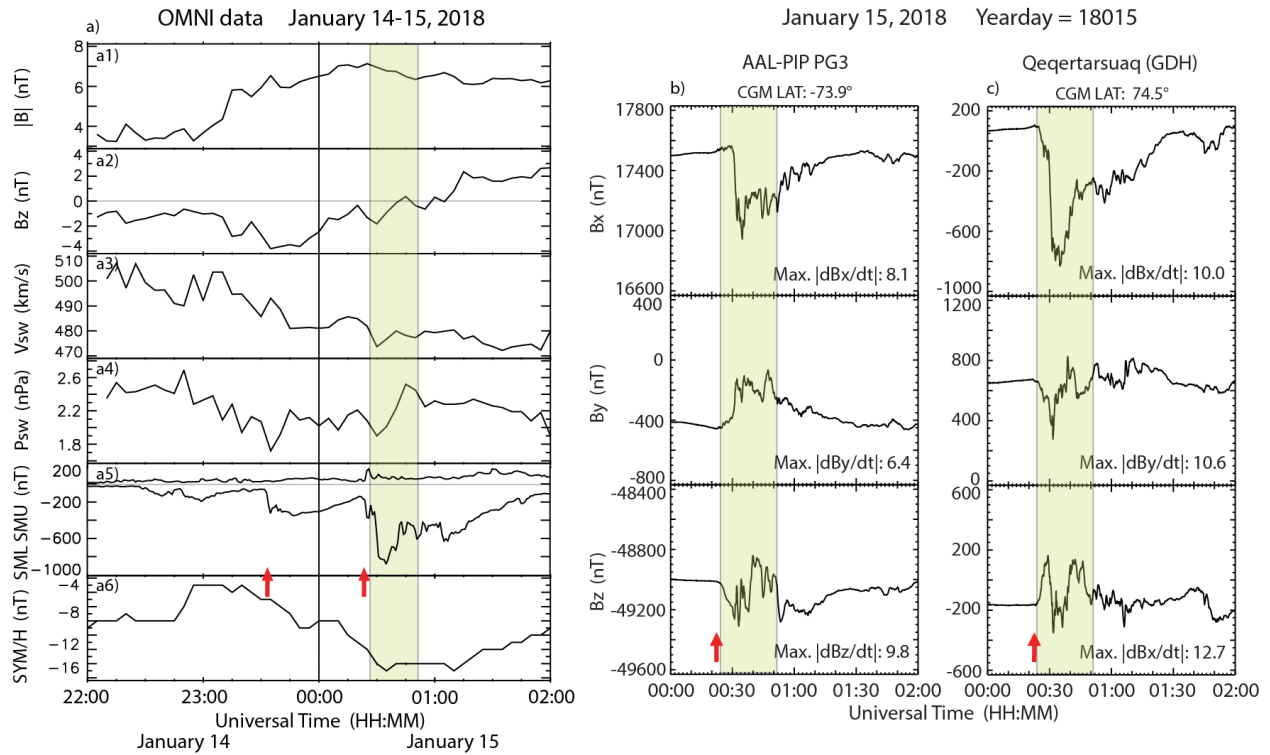
973 Figure 1. Maps showing the location of ground magnetometer stations used for this study. a)  
 974 Map of Arctic Canada and Greenland, showing stations in the northern hemisphere (diamonds)  
 975 and the conjugate mapped locations of southern hemisphere stations (green circles). b) Map of  
 976 Antarctica, showing stations in the southern hemisphere (diamonds, squares, and red circle) and  
 977 the conjugate mapped locations of northern hemisphere stations (triangles). Solid lines show  
 978 corrected geomagnetic coordinates.

979



980  
 981  
 982  
 983  
 984  
 985  
 986

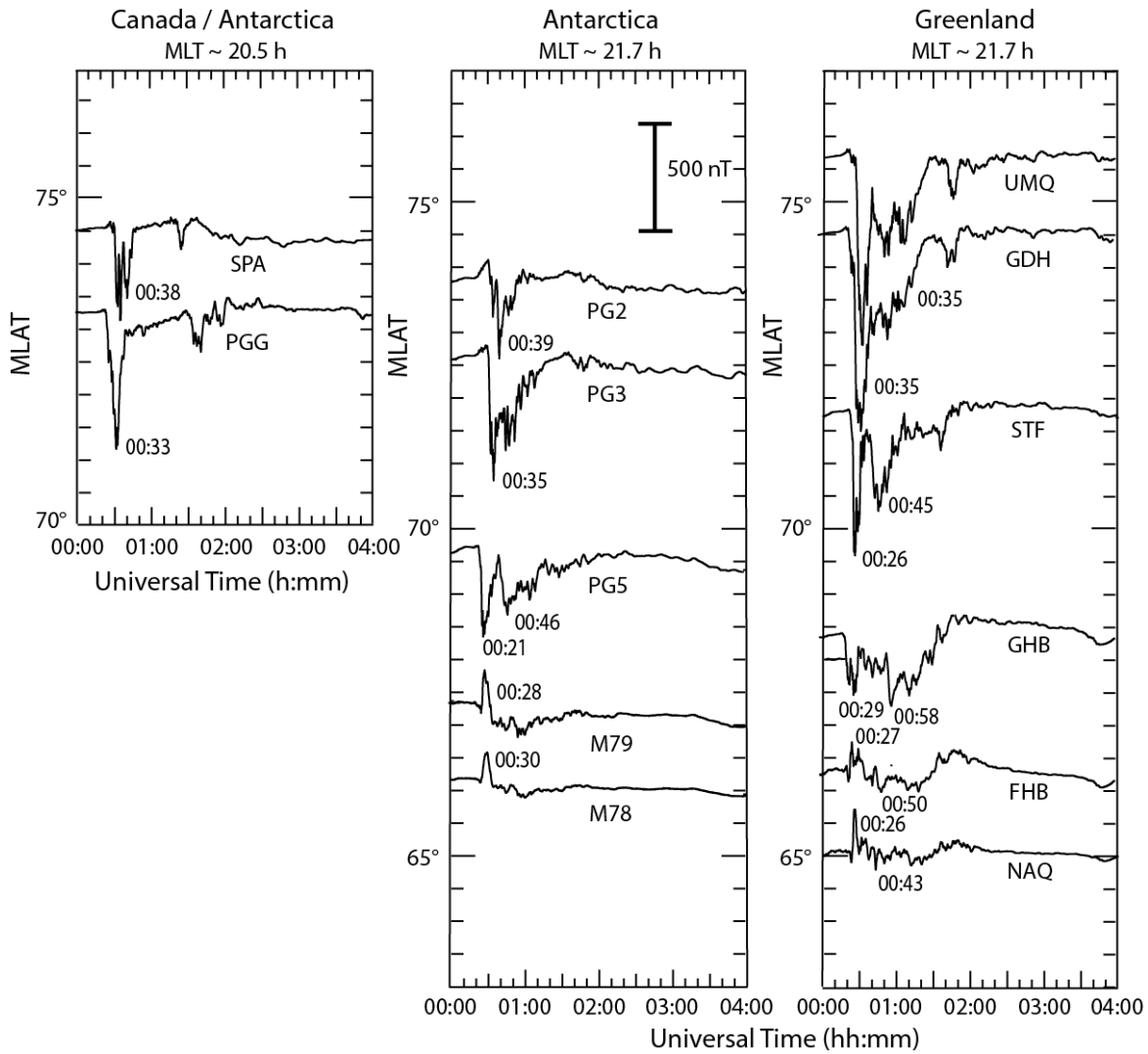
Figure 2. Daily magnetogram from AAL-PIP PG4 on May 13, 2015 with uniform vertical scale increments. The data are shown in local magnetic coordinates: Bx is northward, By eastward, and Bz vertically downward.



987  
988

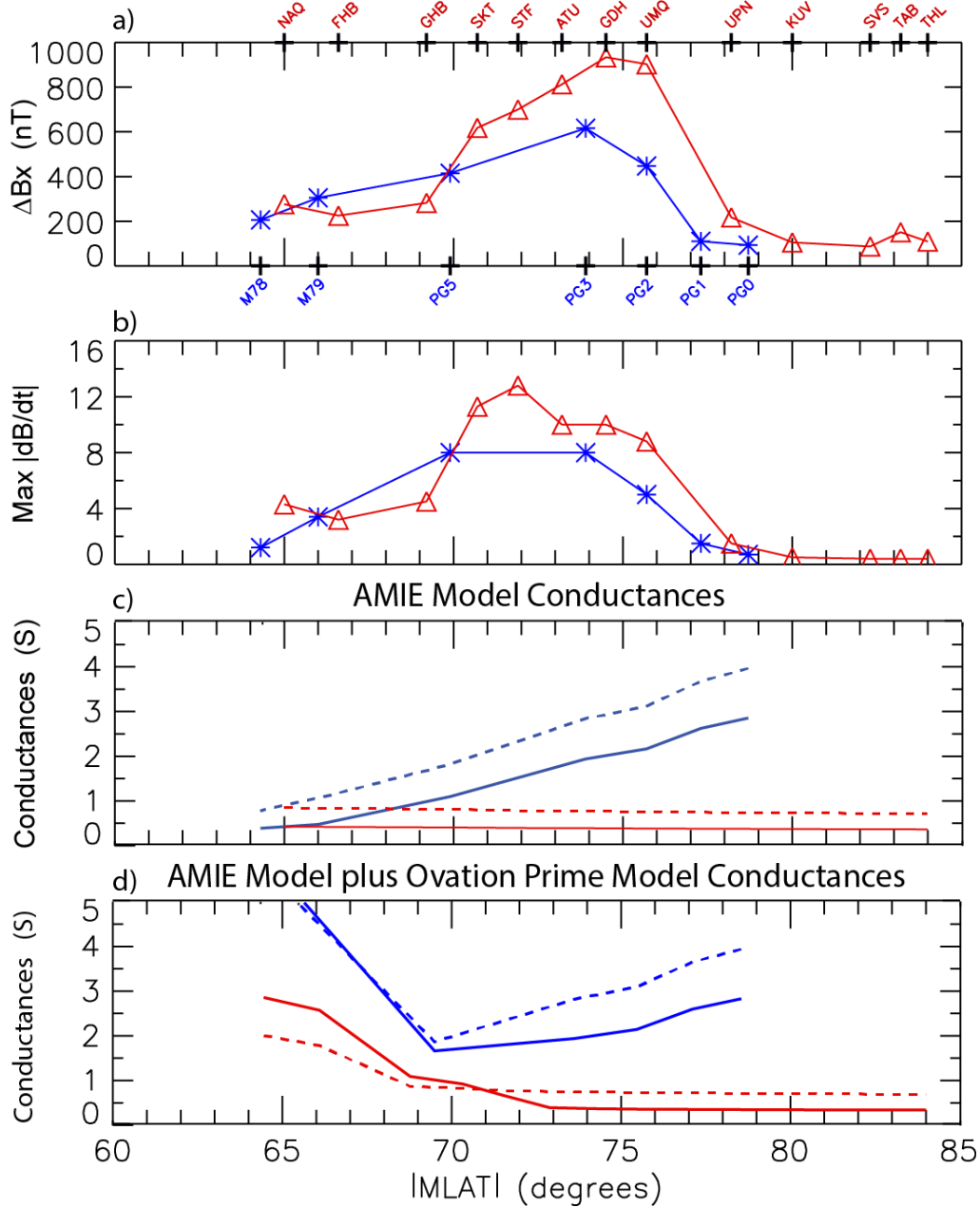
989 Figure 3. Panel a shows OMNI data that provide the interplanetary and magnetospheric context  
990 for the MPE event on January 15, 2018. Panels a1 and a2 show the magnitude  $|B|$  and north-  
991 south component  $B_z$  of the interplanetary magnetic field (IMF), respectively. Panel a3 shows the  
992 solar wind flow speed,  $V_{sw}$ , and panel a4 shows the solar wind dynamic pressure,  $N_{sw}$ . Panel  
993 a5 shows the SuperMAG SML and SMU indices, and panel a6 shows the SYM/H index. Panels  
994 b and c show two-hour excerpts of magnetograms from AAL-PIP PG3, Antarctica, and  
995 Qeqertarsuaq (GDH), Greenland, respectively. The shaded region in each panel, from 0024 to  
996 0052 UT, highlights the large magnetic perturbation observed at both stations, and the red arrows  
997 indicates the time of the closest prior substorm onsets.

998  
999



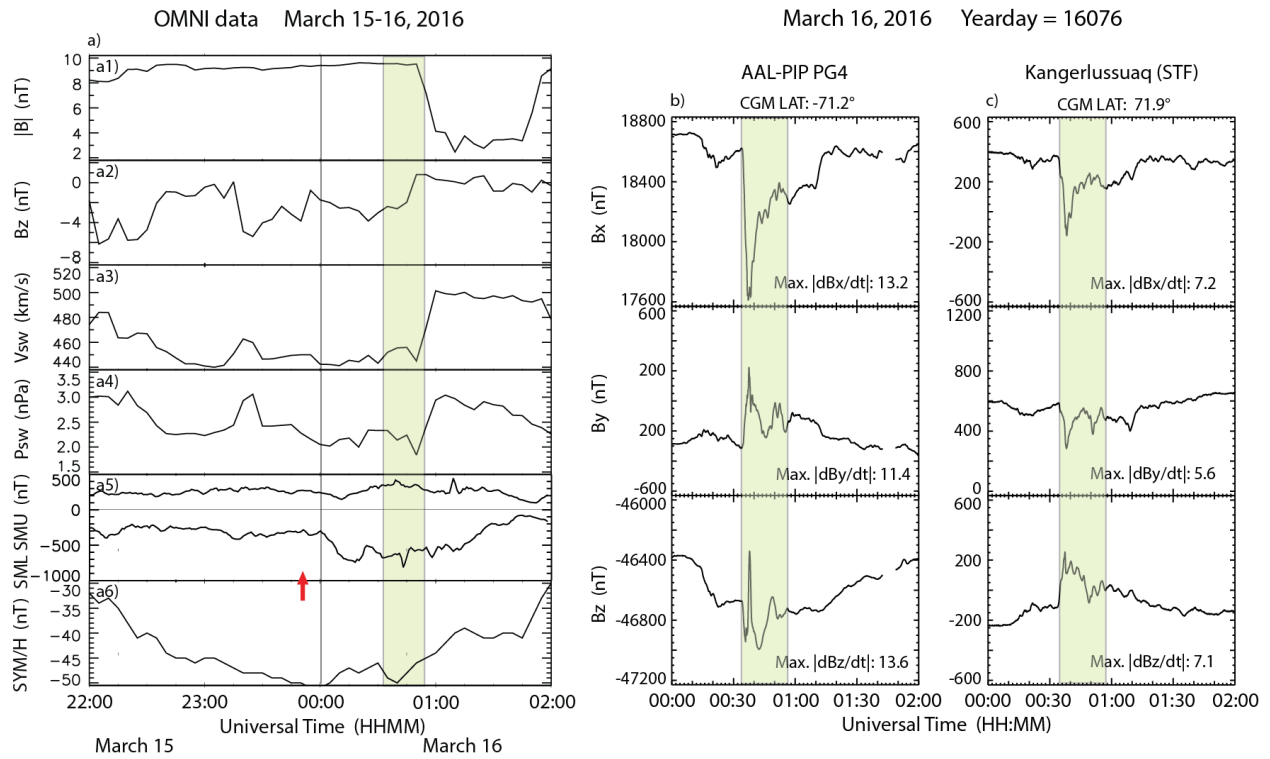
1000  
 1001  
 1002 Figure 4. Four-hour excerpts of Bx component (north-south) magnetograms for January 15,  
 1003 2018 from a) SPA and PGG, b) PG2, PG3, PG5, M79, and M78, and c) UMQ, GDH, STF, GHB,  
 1004 FHB, and NAQ), arranged vertically in order of magnetic latitude and horizontally in order of  
 1005 magnetic local time / magnetic longitude. At each station, the time of maximum  $|\Delta B_x|$   
 1006 perturbations is shown.

January 15, 2018 18015 ~ 00:35 UT



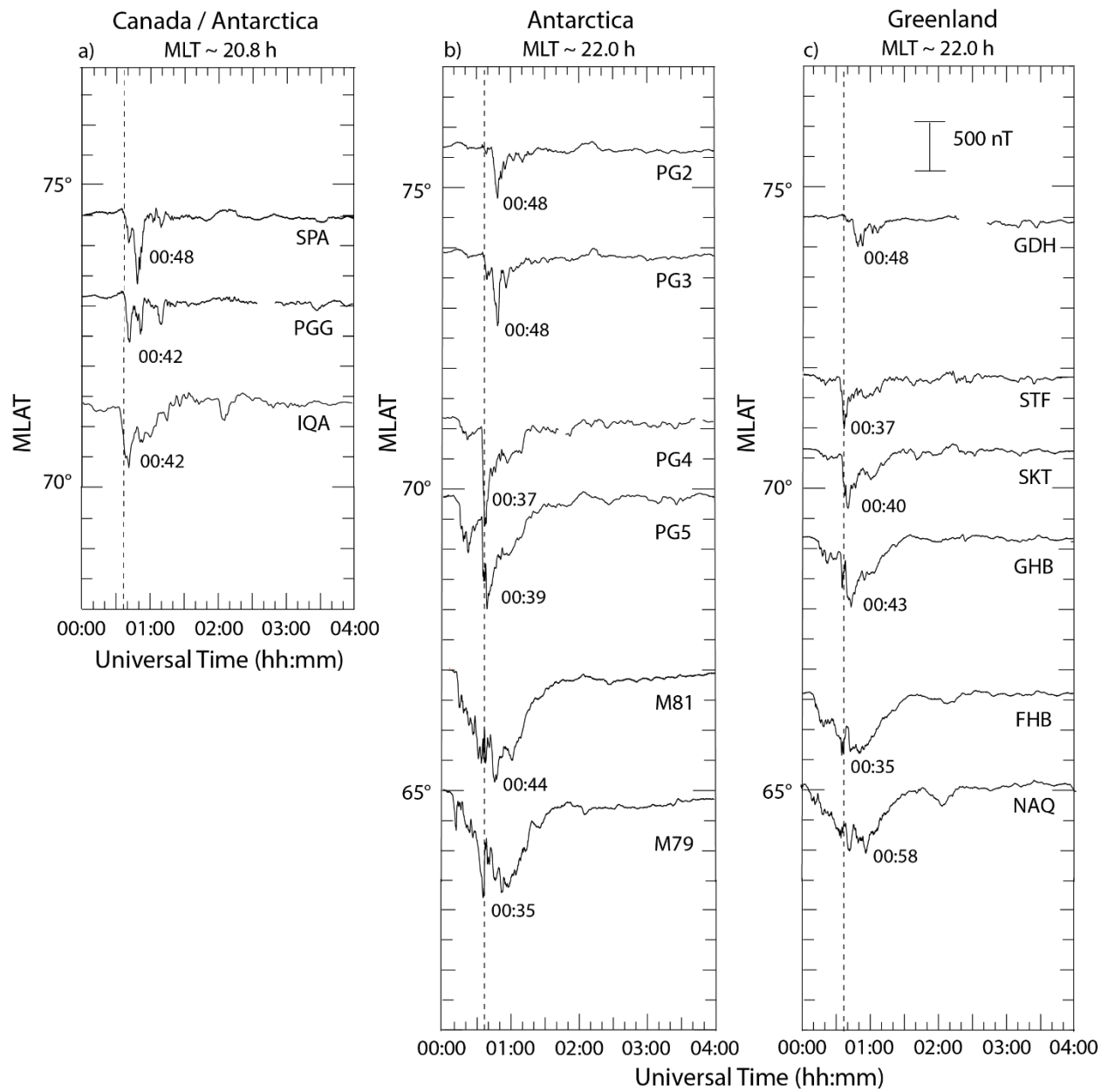
1007

1008 Figure 5. Plots of the perturbation amplitude  $\Delta B_x$  (panel a), the maximum derivative in any  
 1009 component (panel b), and two models of the ionospheric Pedersen and Hall conductances (panels  
 1010 c and d), as a function of magnetic latitude, observed at every available station in the West  
 1011 Greenland Coastal Array (red) and the AAL-PIP and BAS LPM arrays (blue) for the MPE at  
 1012 ~0035 UT January 15, 2018. Solid lines denote Pedersen conductances ( $\Sigma_P$ ) and dashed lines  
 1013 Hall conductances ( $\Sigma_H$ ).



1014  
 1015  
 1016  
 1017  
 1018  
 1019  
 1020  
 1021  
 1022  
 1023

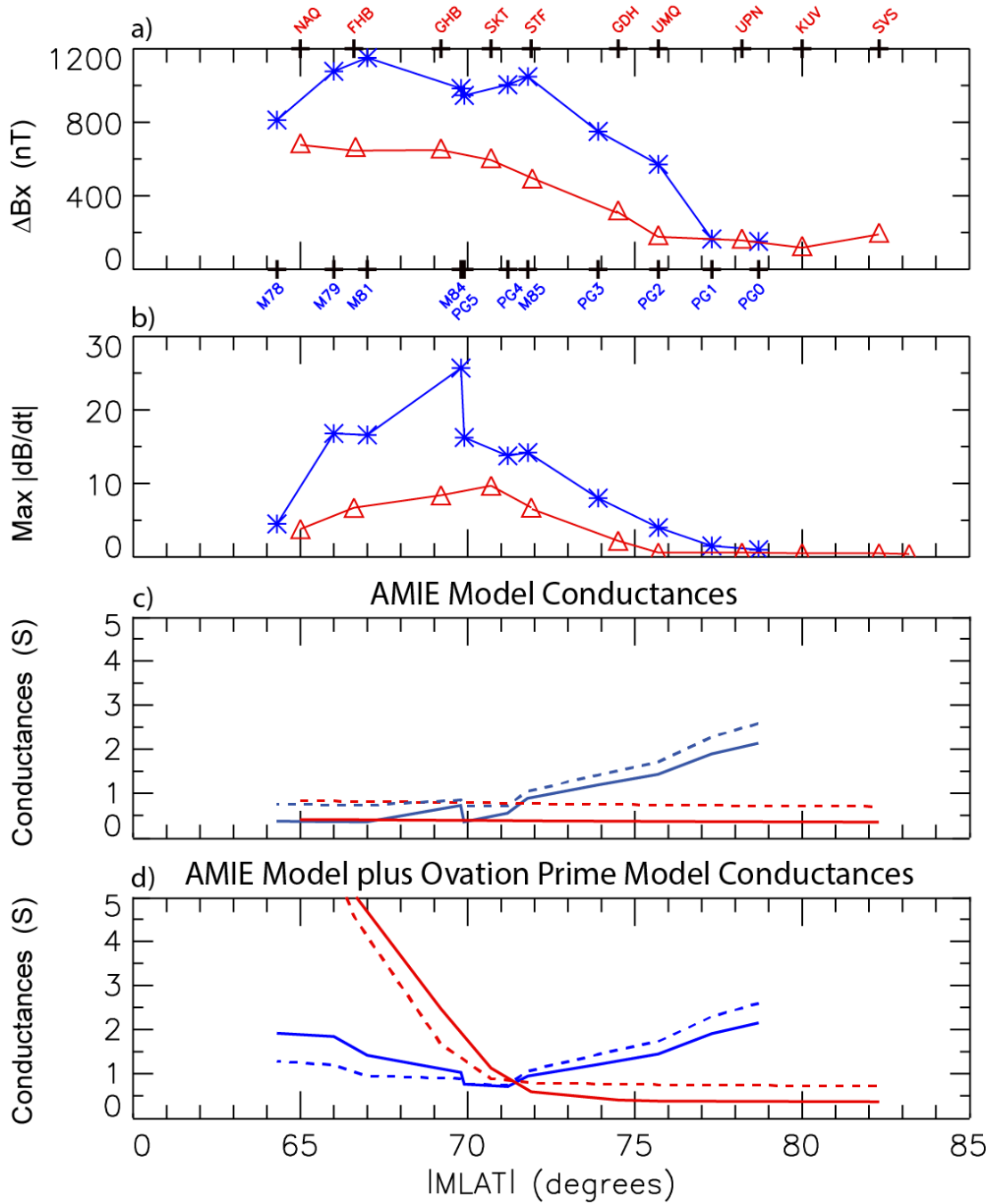
Figure 6. Panel a shows OMNI data for the MPE event on March 16, 2016, as in Figure 3. Panels b and c show two-hour excerpts of magnetograms from AAL-PIP PG4, Antarctica, and Kangerlussuaq (STF), Greenland, respectively. The shaded region in each panel, from 0034 to 0057 UT, highlights the large magnetic perturbation observed at both stations, and the red arrow indicates the time of the closest prior substorm onset.



1024  
 1025  
 1026  
 1027  
 1028  
 1029  
 1030  
 1031

Figure 7. Four-hour excerpts of Bx component (north-south) magnetograms for March 16, 2016, as in Figure 4. a) SPA, PGG, and IQA, b) PG2, PG3, PG4, PG5, M81, and M79, and c) GDH, STF, SKT, GHB, FHB, and NAQ. At each station, the time of maximum  $|\Delta B_x|$  perturbations is shown. The vertical dashed lines mark 00:37 UT, the time of minima in the Bx component at PG4, M84 (not shown), and STF.

March 16, 2016 16076 00:38 and 00:48 UT



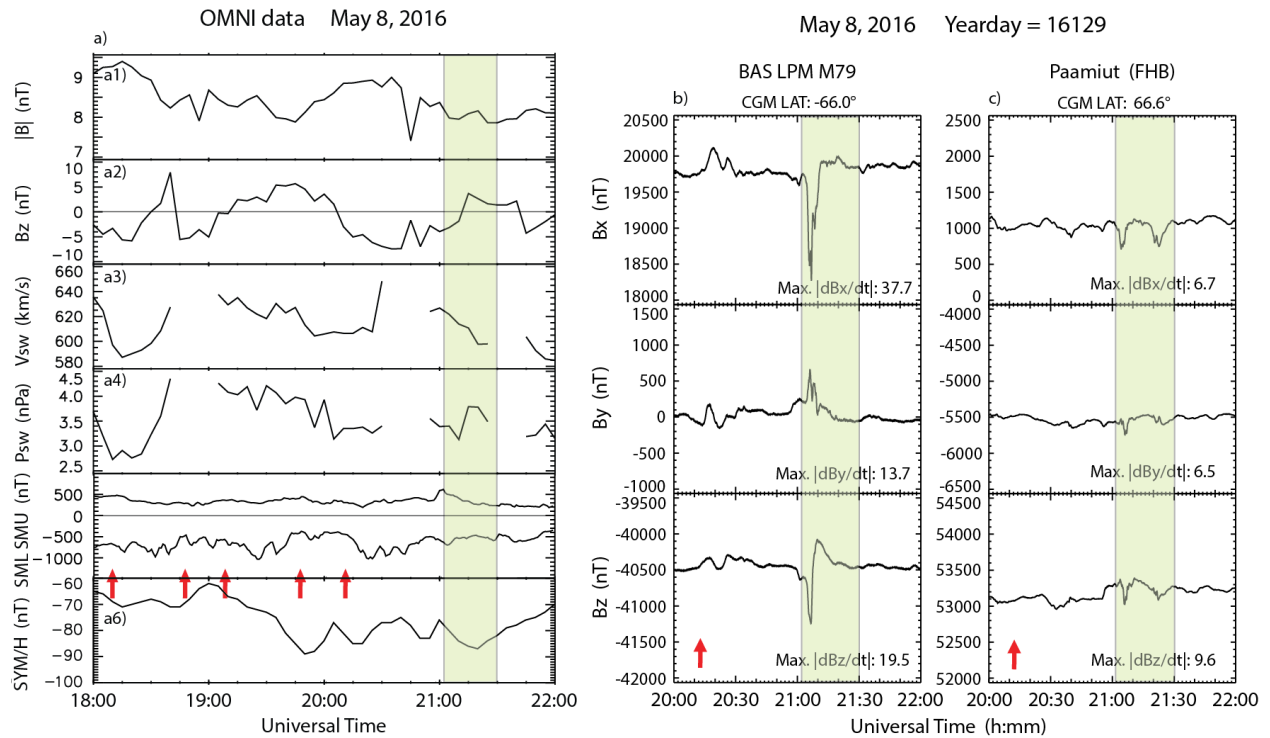
1032

1033 Figure 8. Plots of the perturbation amplitude  $\Delta B_x$  (panel a), the maximum derivative in any  
 1034 component (panel b), and two models of the ionospheric Pedersen and Hall conductances (panels  
 1035 c and d), as a function of magnetic latitude as in Figure 5, for the MPEs near ~0040 UT March  
 1036 16, 2016. Solid lines denote Pedersen conductances ( $\Sigma_P$ ) and dashed lines Hall conductances  
 1037 ( $\Sigma_H$ ).

1038

1039

1040



1041

1042

1043 Figure 9. Panel a shows OMNI data for the MPE event on May 8, 2016, as in Figure 3. Panels b

1044 and c show two-hour excerpts of magnetograms from BAS LPM M79, Antarctica, and Paamiut

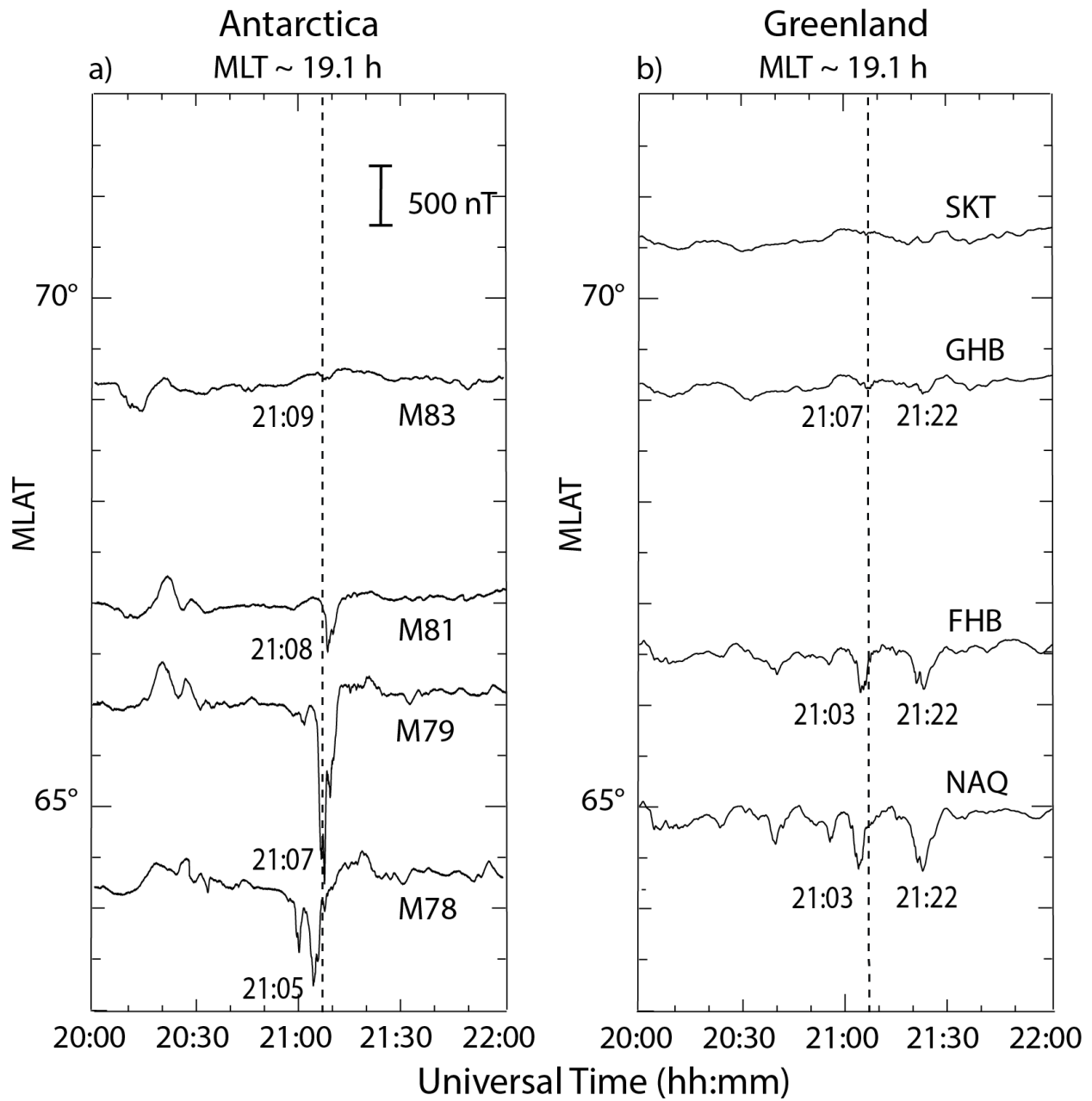
1045 (FHB), Greenland, respectively. The shaded region in each panel, from 2102 to 2130 UT,

1046 highlights the large magnetic perturbations observed at both stations, and the red arrows indicate

1047 the times of the closest prior substorm onsets.

1048

1049



1051

1052 Figure 10. Two-hour excerpts of Bx component (north-south) magnetograms for May 8, 2016,

1053 as in Figure 4. a) M83, M81, M79, and M78, and b) SKT, GHB, FHB, and NAQ. At each

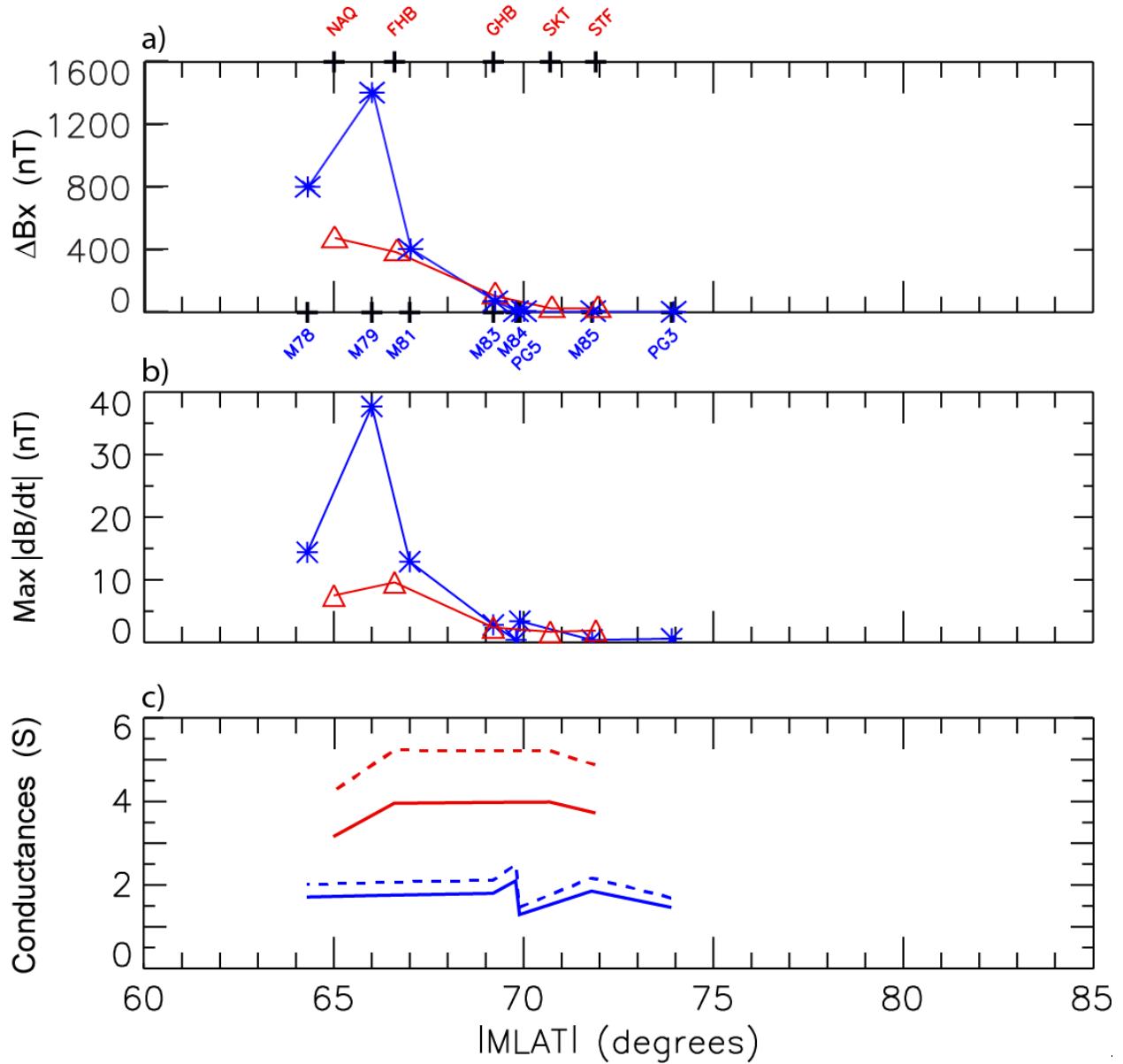
1054 station, the time of maximum  $|\Delta B_x|$  perturbations is shown. The vertical dashed lines mark

1055 21:07 UT, the time of minima in the Bx component at GHB and M79.

1056

1057

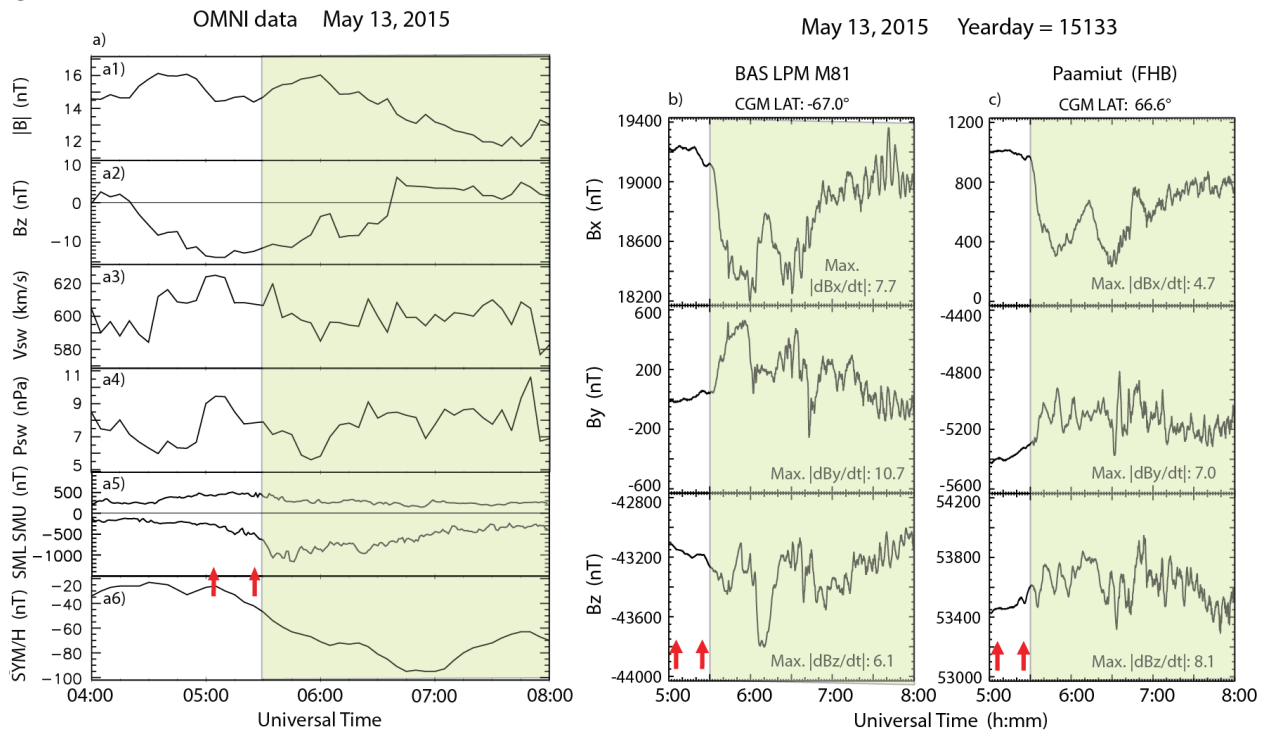
May 8, 2016 16129 ~21:08 UT



1058

1059 Figure 11. Plots of the perturbation amplitude  $\Delta B_x$  (panel a), the maximum derivative in any  
 1060 component (panel b), and a model of the ionospheric Pedersen and Hall conductances (panel c),  
 1061 as a function of magnetic latitude as in Figure 5, for the MPE at ~2108 UT May 8, 2016. Solid  
 1062 lines denote Pedersen conductances ( $\Sigma_P$ ) and dashed lines Hall conductances ( $\Sigma_H$ ).

1063 C



1064

1065

1066

1067

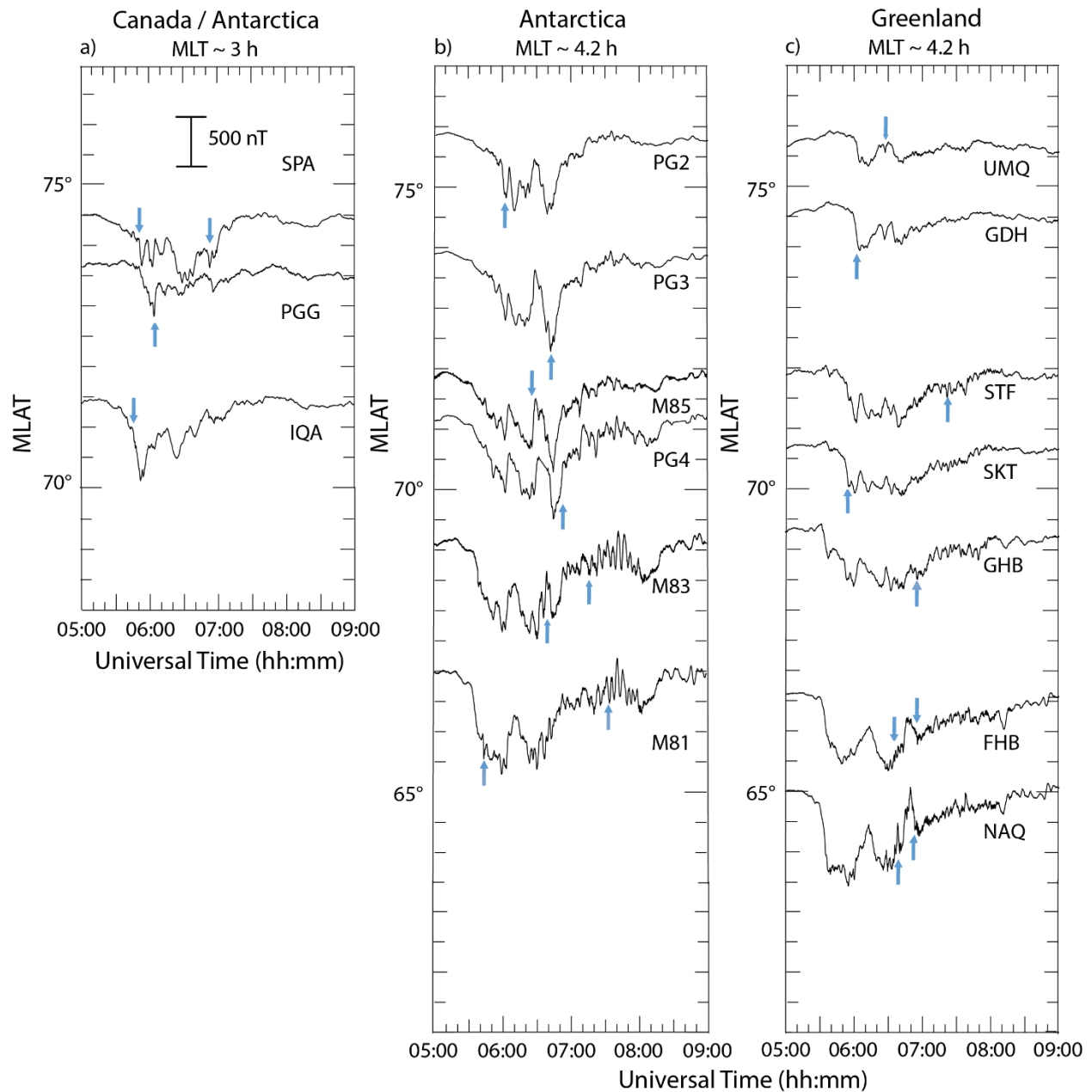
1068

1069

1070

1071

Figure 12. Panel a shows OMNI data for the MPE event on May 3, 2015, as in Figure 3. Panels b and c show three-hour excerpts of magnetograms from BAS LPM M81, Antarctica, and Paamiut (FHB), Greenland, respectively. The shaded region in each panel, from 0530 to 0800 UT, highlights the large magnetic perturbations observed at both stations, and the red arrows indicate the times of the closest prior substorm onsets.



1072

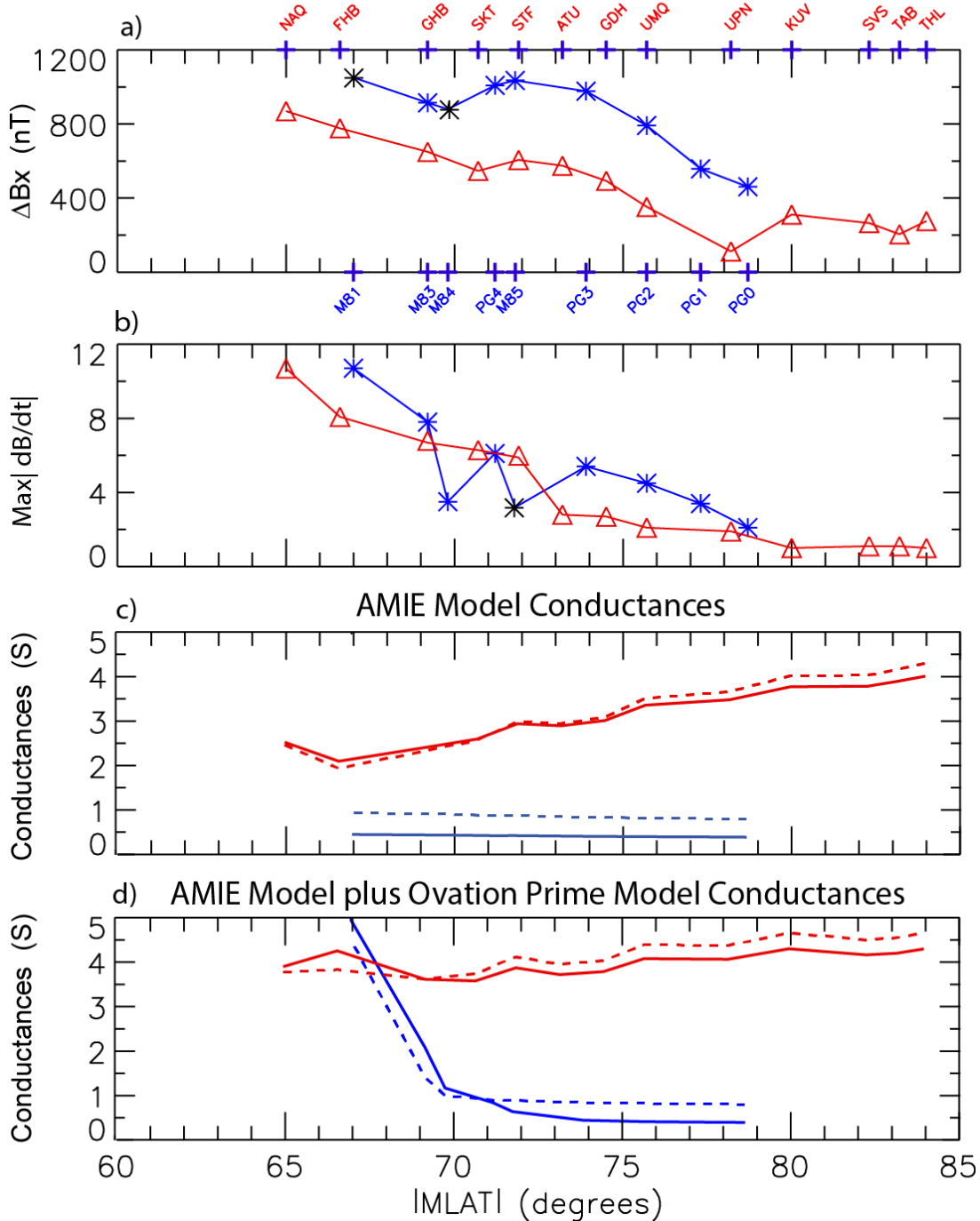
1073 Figure 13. Four-hour excerpts of Bx component (north-south) magnetograms for May 13, 2015,

1074 as in Figure 4. a) SPA, PGG, and IQA, b) PG2, M85, PG4, M83, and M81, and c) UMQ, STF,

1075 SKT, GHB, FHB, and NAQ. Blue arrows indicate the strongest MPEs at each station.

1076

May 13, 2015 15133 05:30 - 08:00 UT



1077

1078 Figure 14. Plots of the perturbation amplitude  $\Delta B_x$  (panel a), the maximum derivative in any  
 1079 component (panel b), and two models of the ionospheric Pedersen and Hall conductances (panels  
 1080 c and d), as a function of magnetic latitude as in Figure 5, for the MPEs from 0530 to 0800 UT  
 1081 May 13, 2015. Solid lines denote Pedersen conductances ( $\Sigma_P$ ) and dashed lines Hall  
 1082 conductances ( $\Sigma_H$ ).

Figure 1.

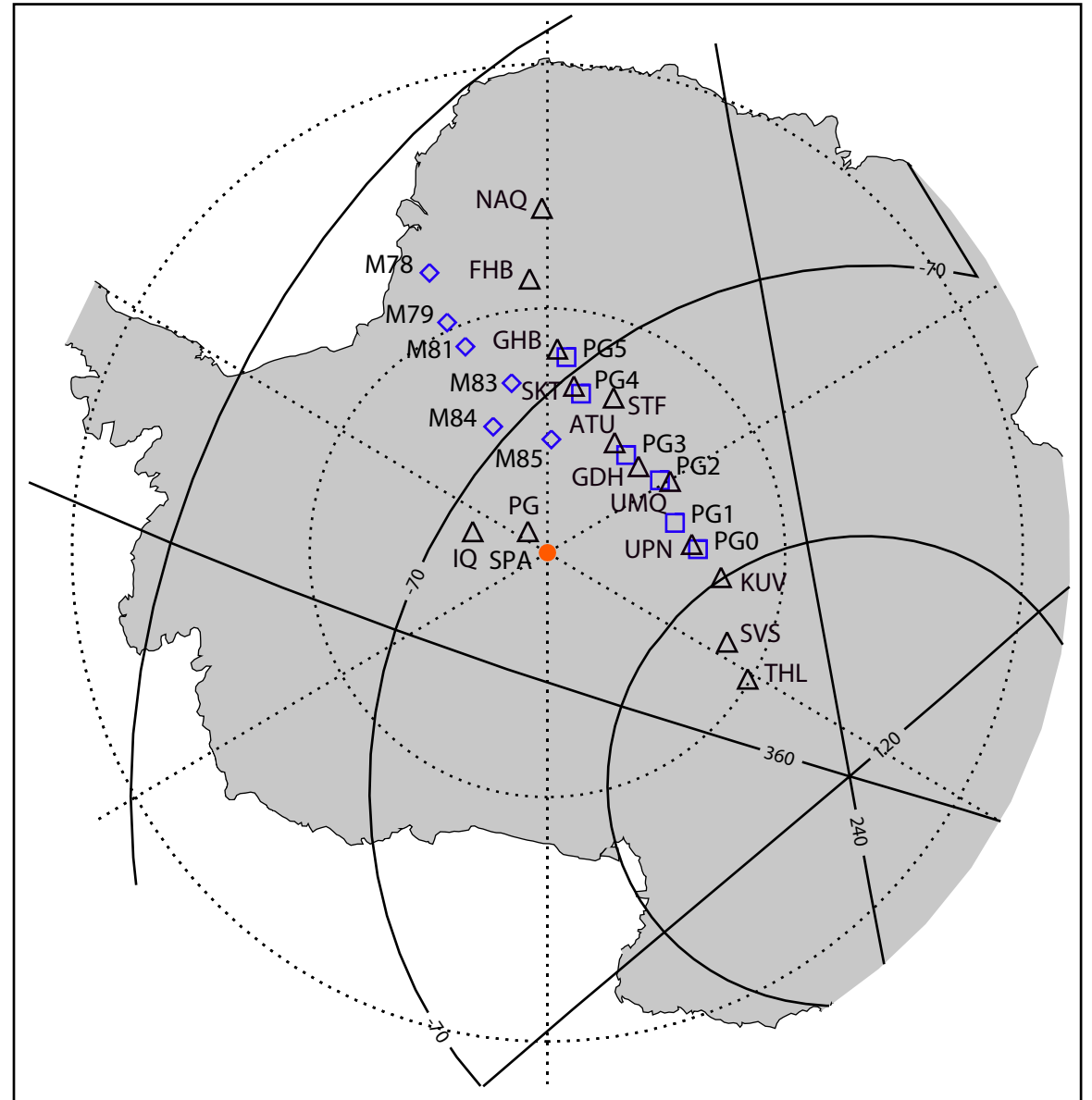
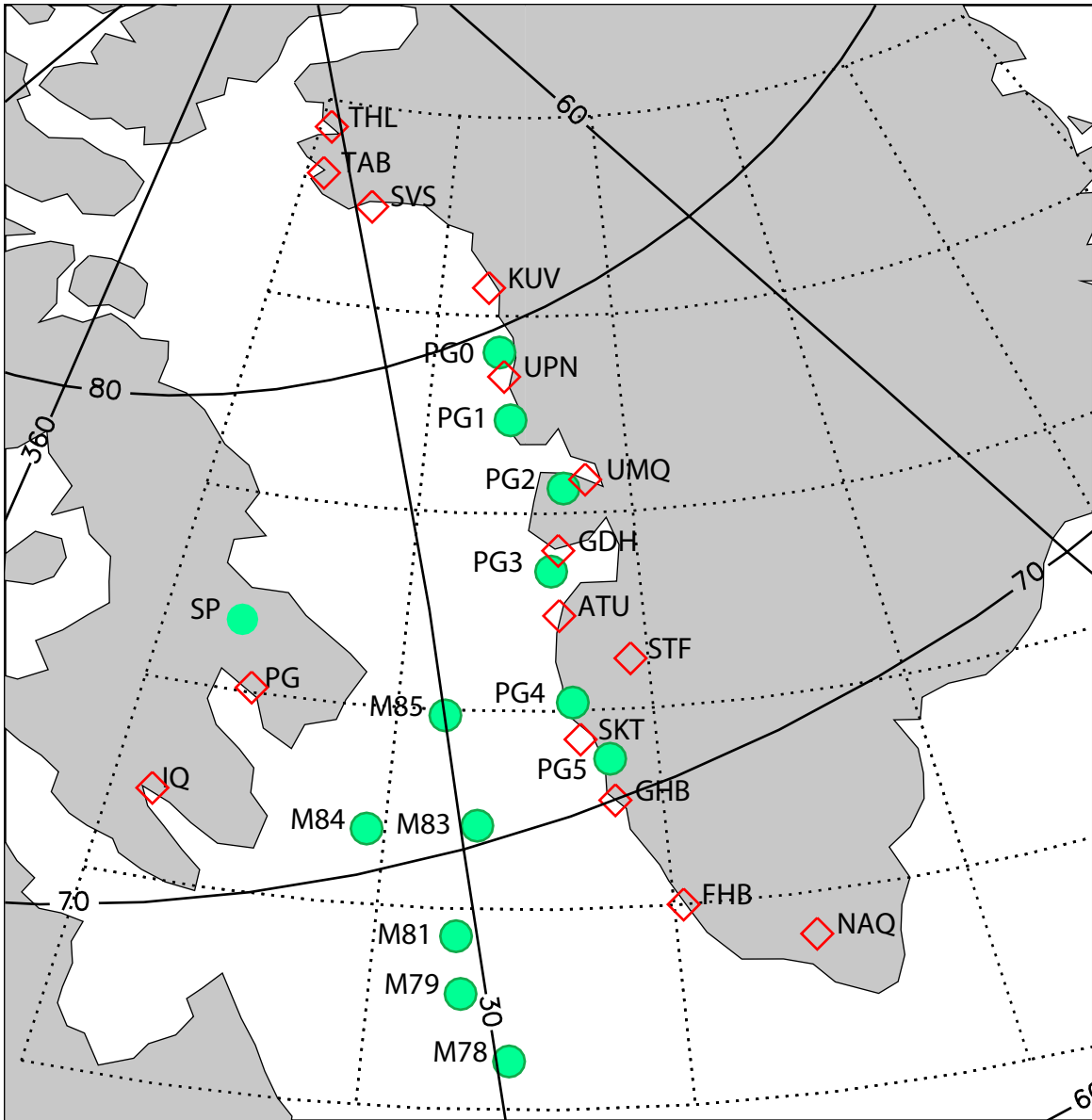
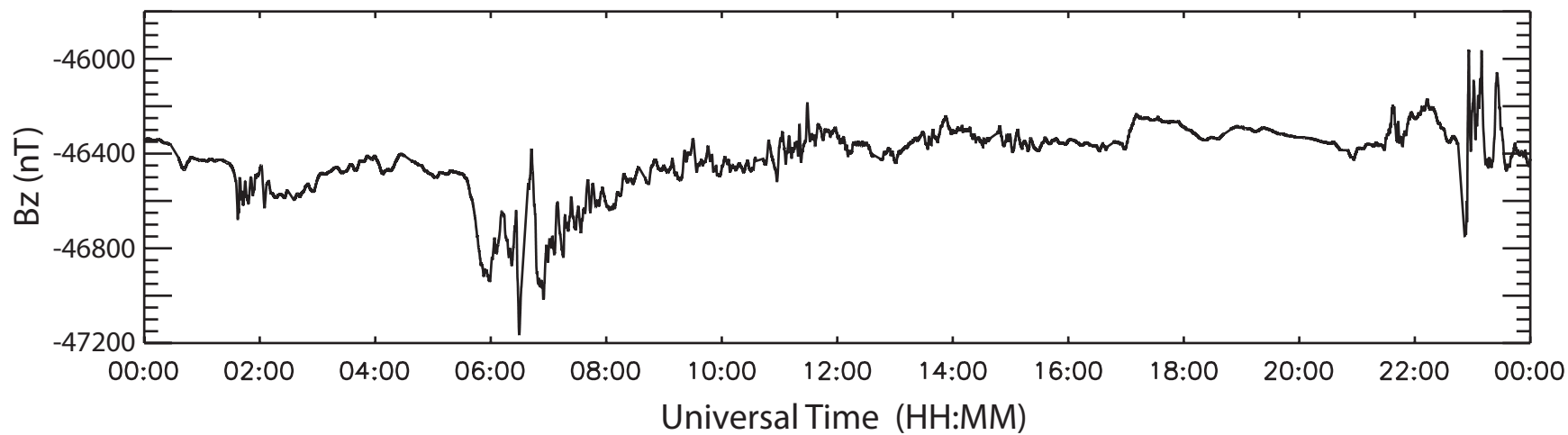
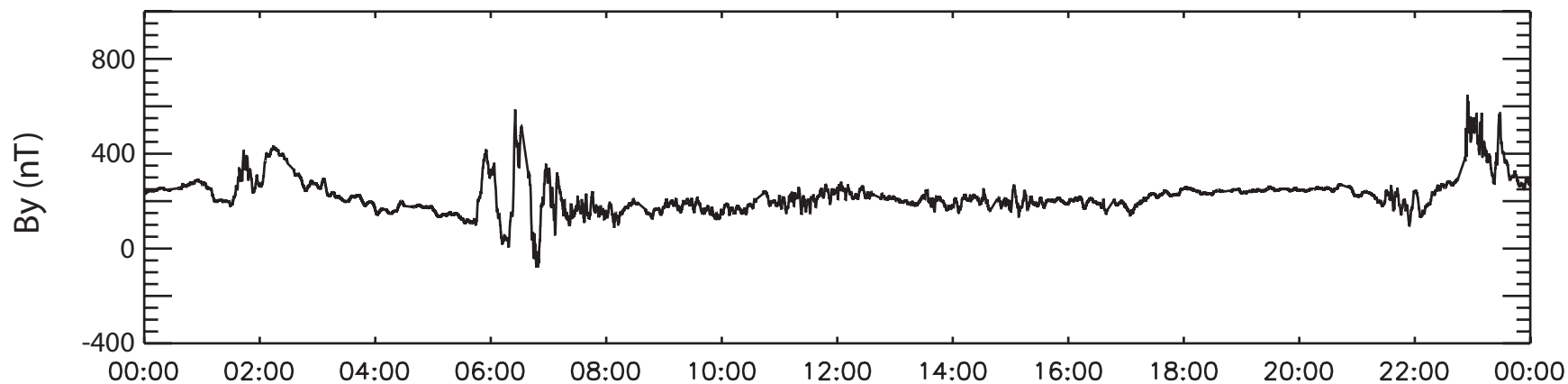
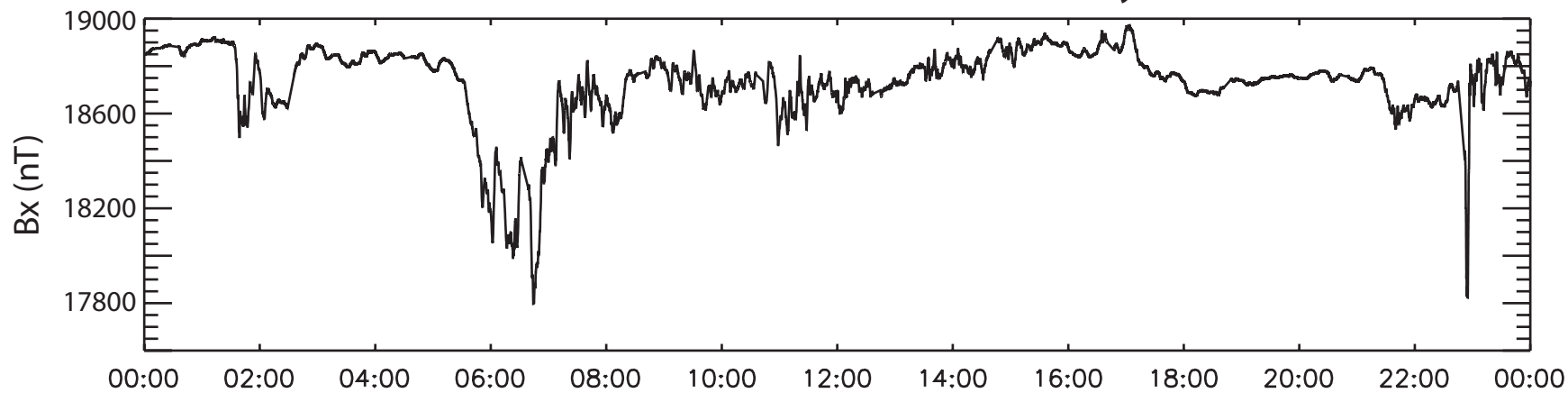


Figure 2.

AAL-PIP PG4

YEARDAY = 15133

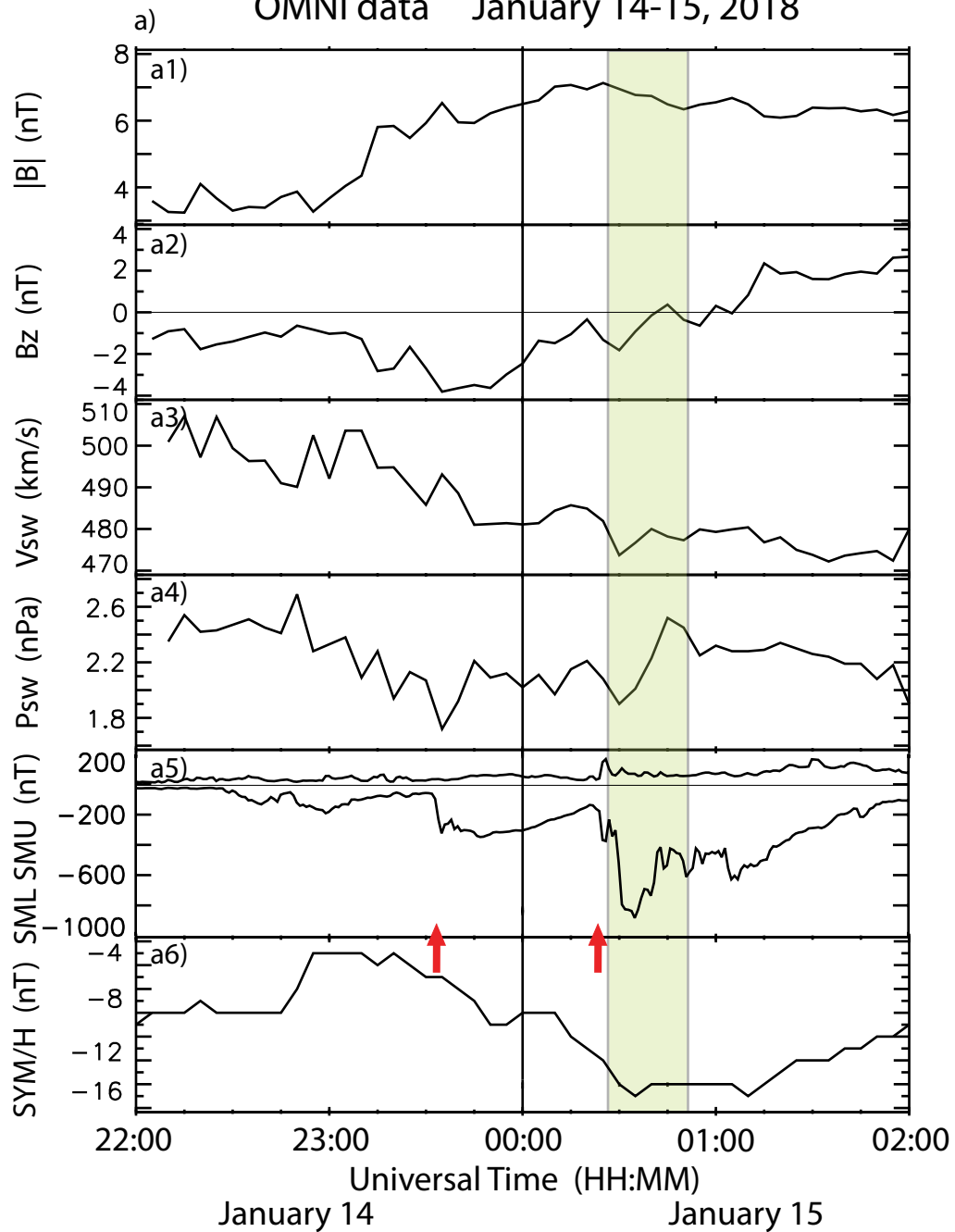
May 13, 2015



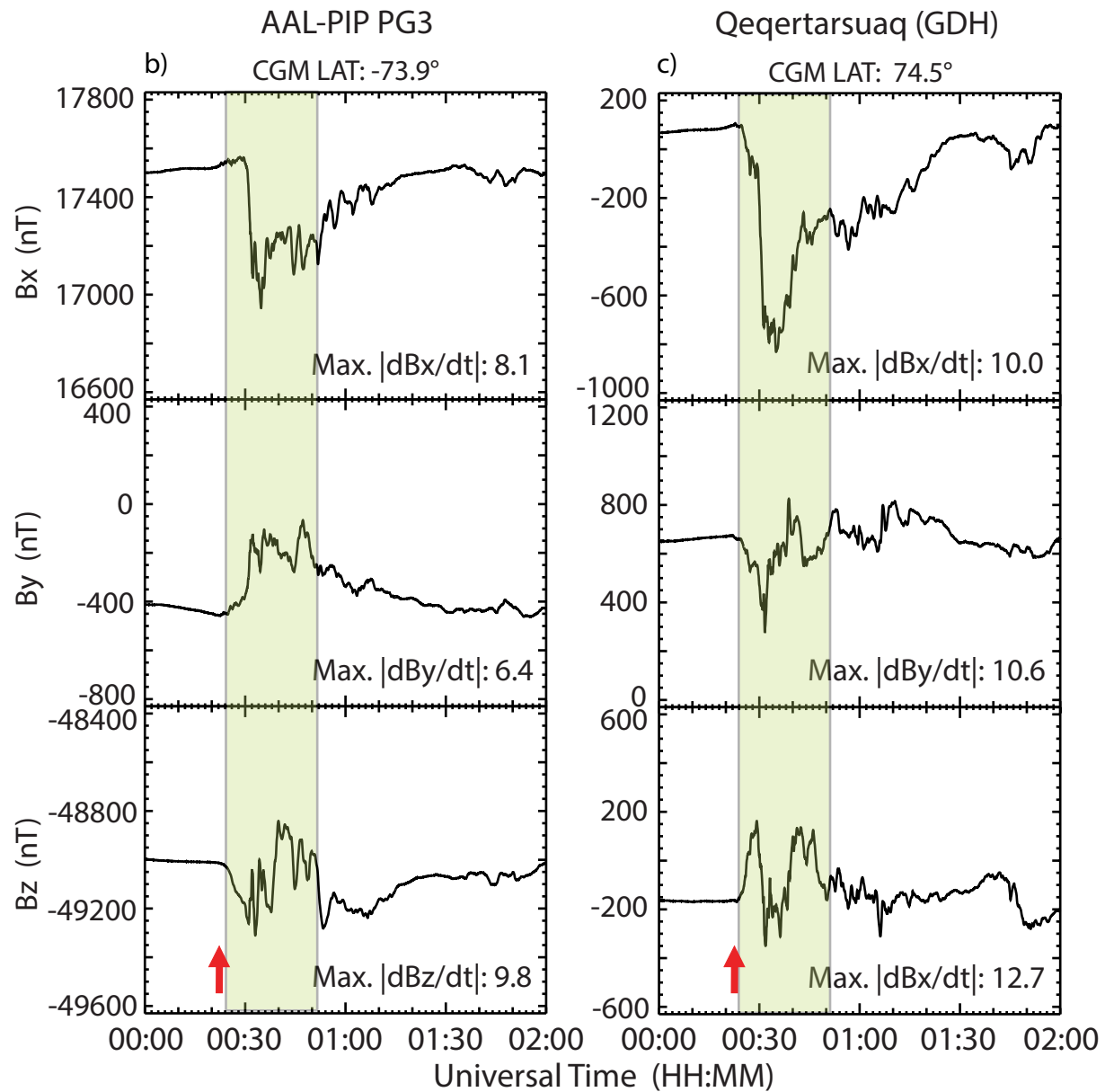
Universal Time (HH:MM)

Figure 3.

OMNI data January 14-15, 2018



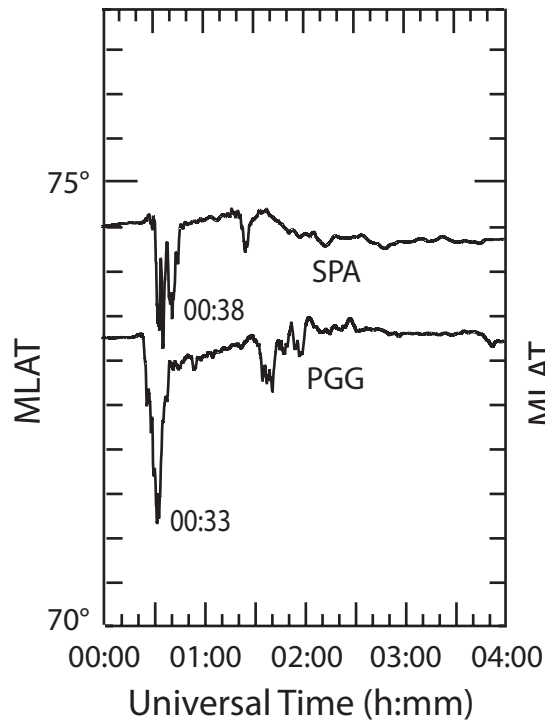
January 15, 2018 Yearday = 18015



**Figure 4.**

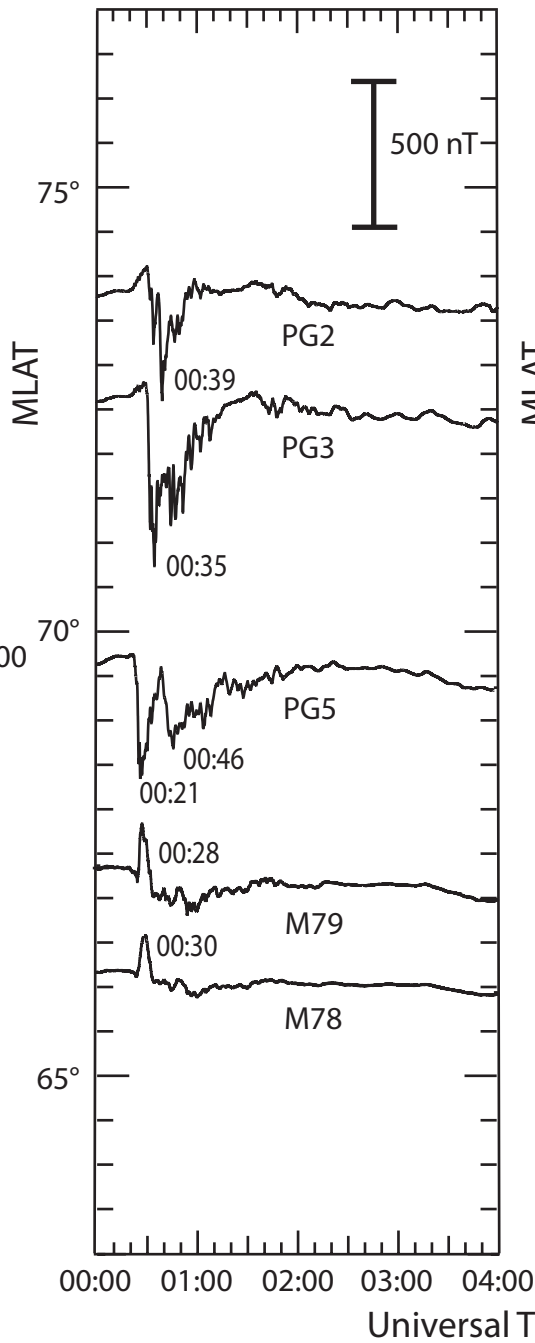
### Canada / Antarctica

MLT ~ 20.5 h



### Antarctica

MLT ~ 21.7 h



### Greenland

MLT ~ 21.7 h

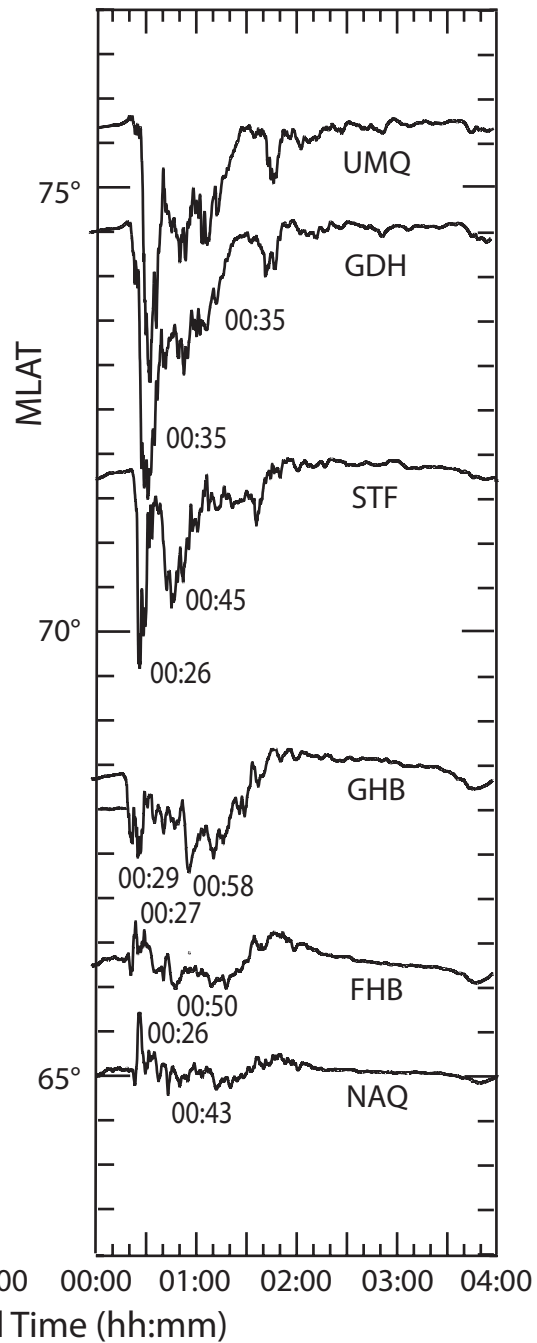


Figure 5.

January 15, 2018 18015 ~ 00:35 UT

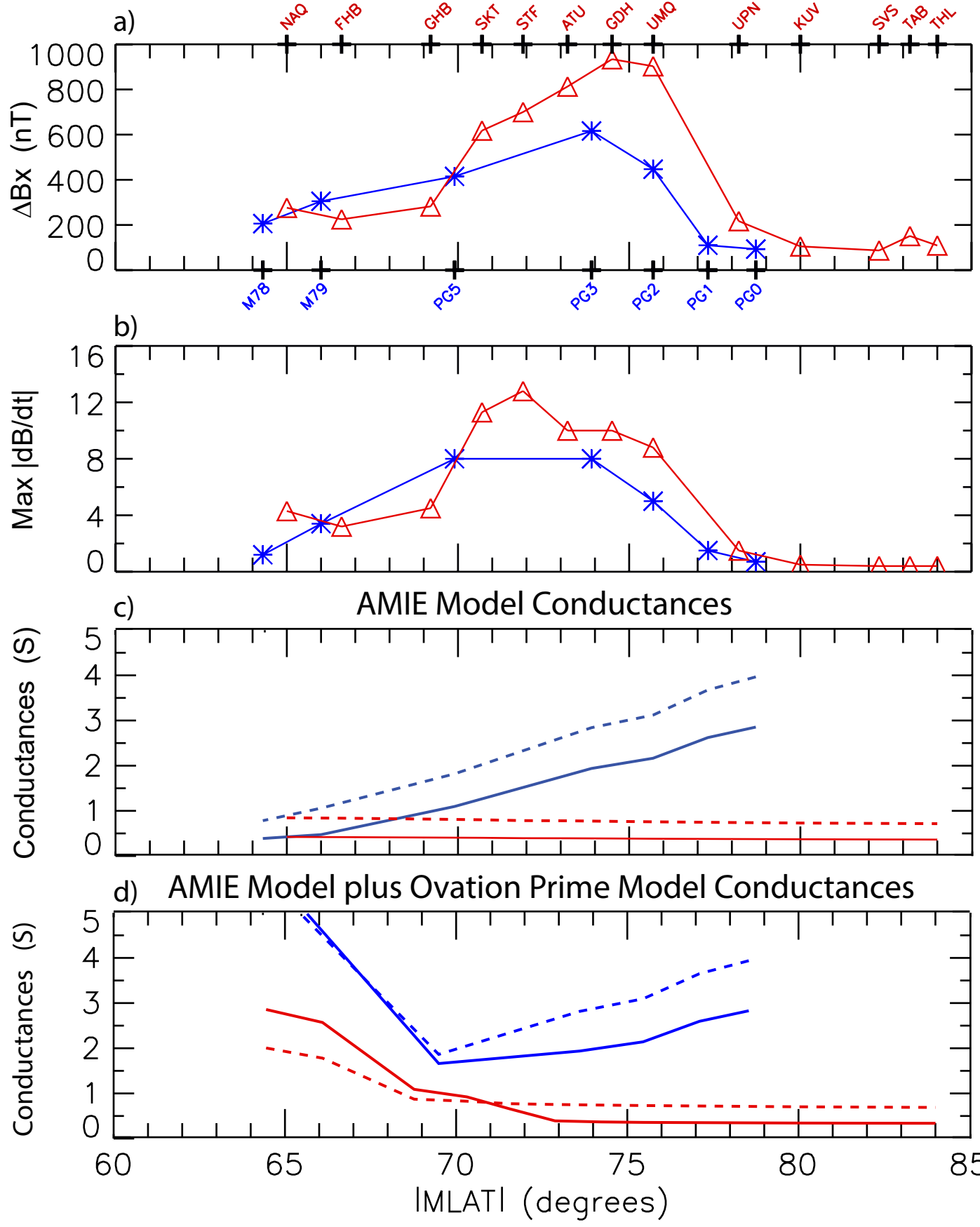
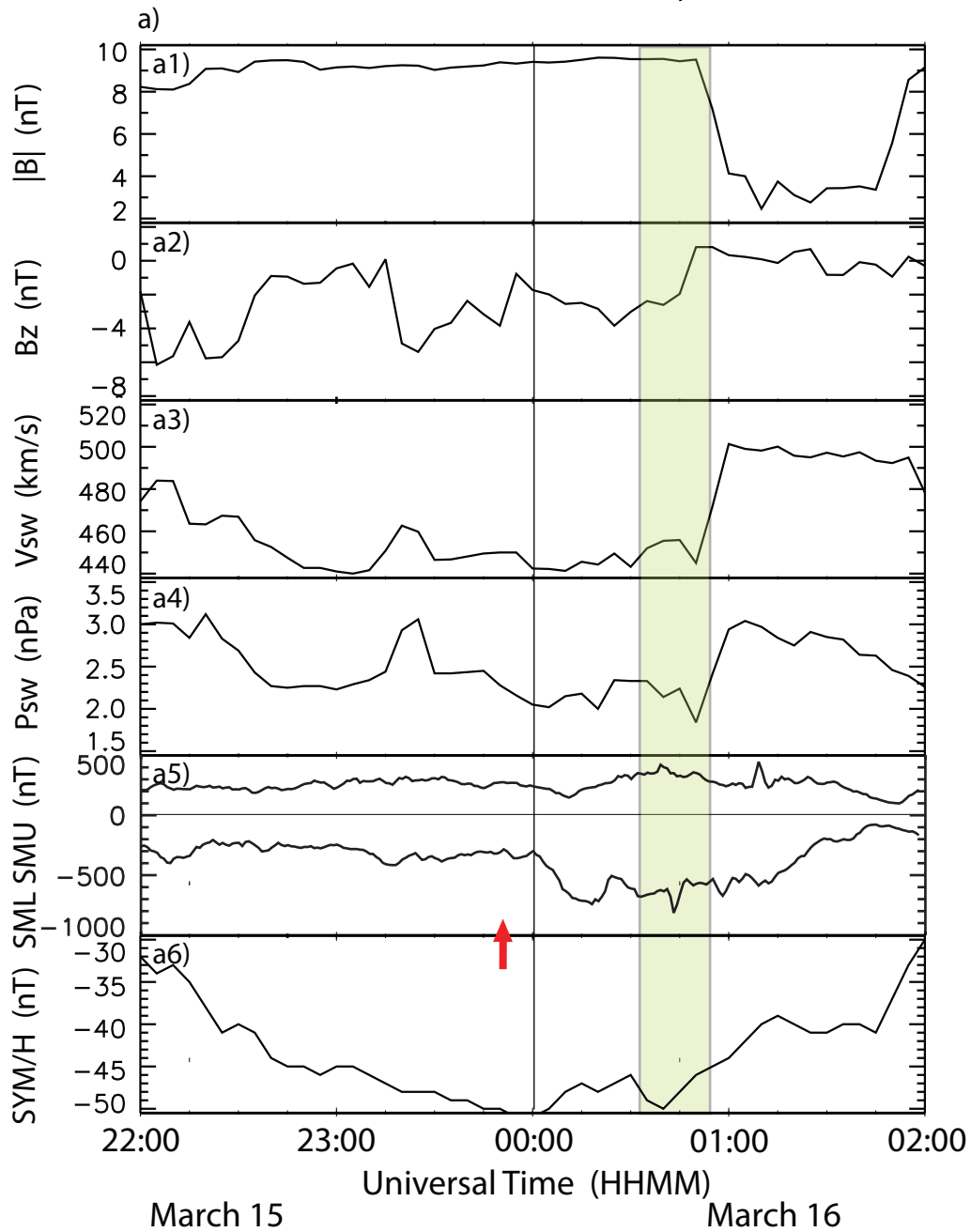


Figure 6.

OMNI data March 15-16, 2016



March 16, 2016 Yearday = 16076

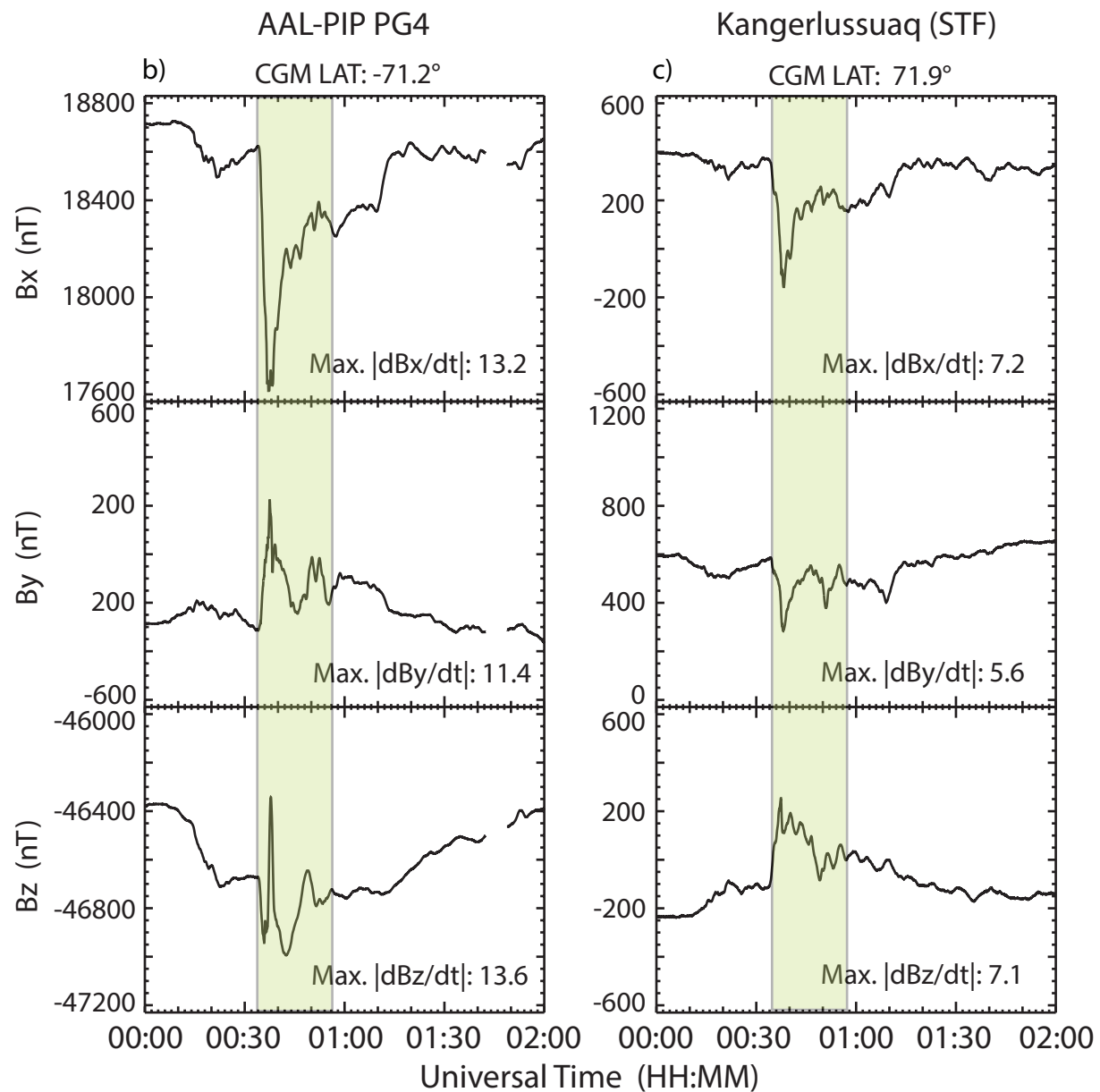
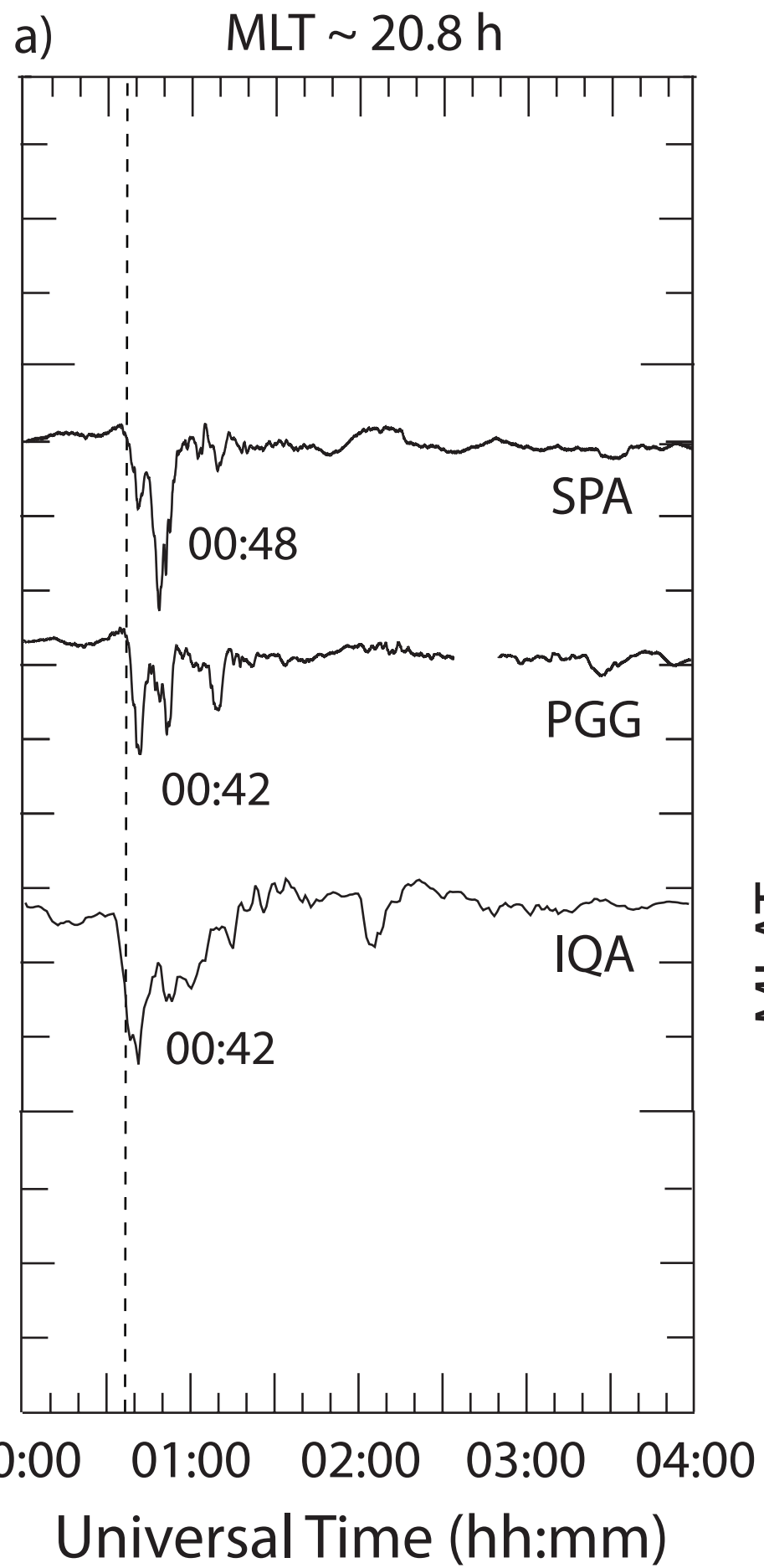
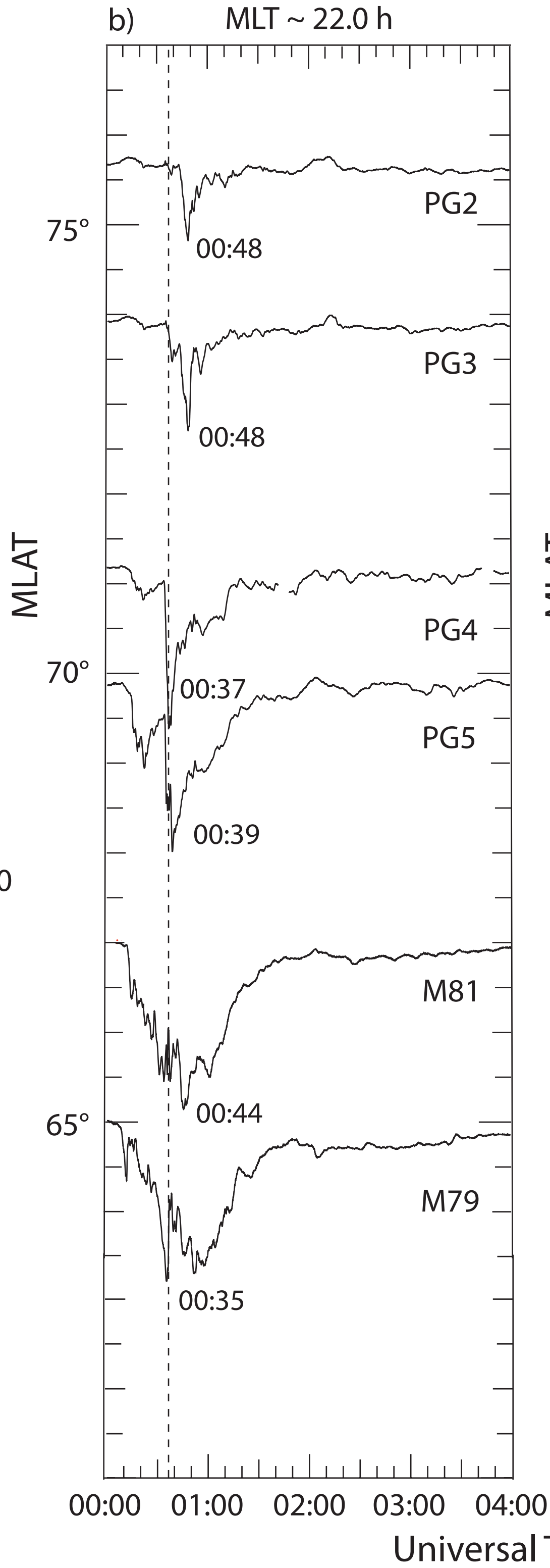


Figure 7.

### Canada / Antarctica



### Antarctica



### Greenland

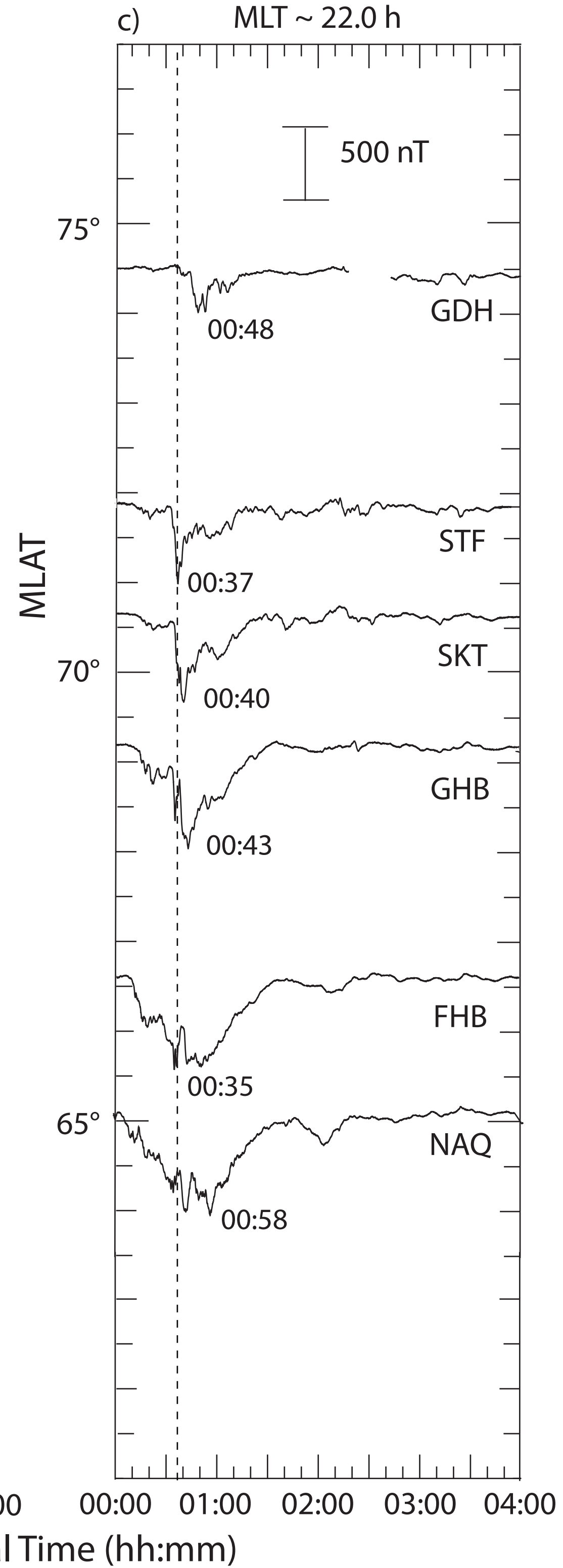


Figure 8.

March 16, 2016 16076 00:38 and 00:48 UT

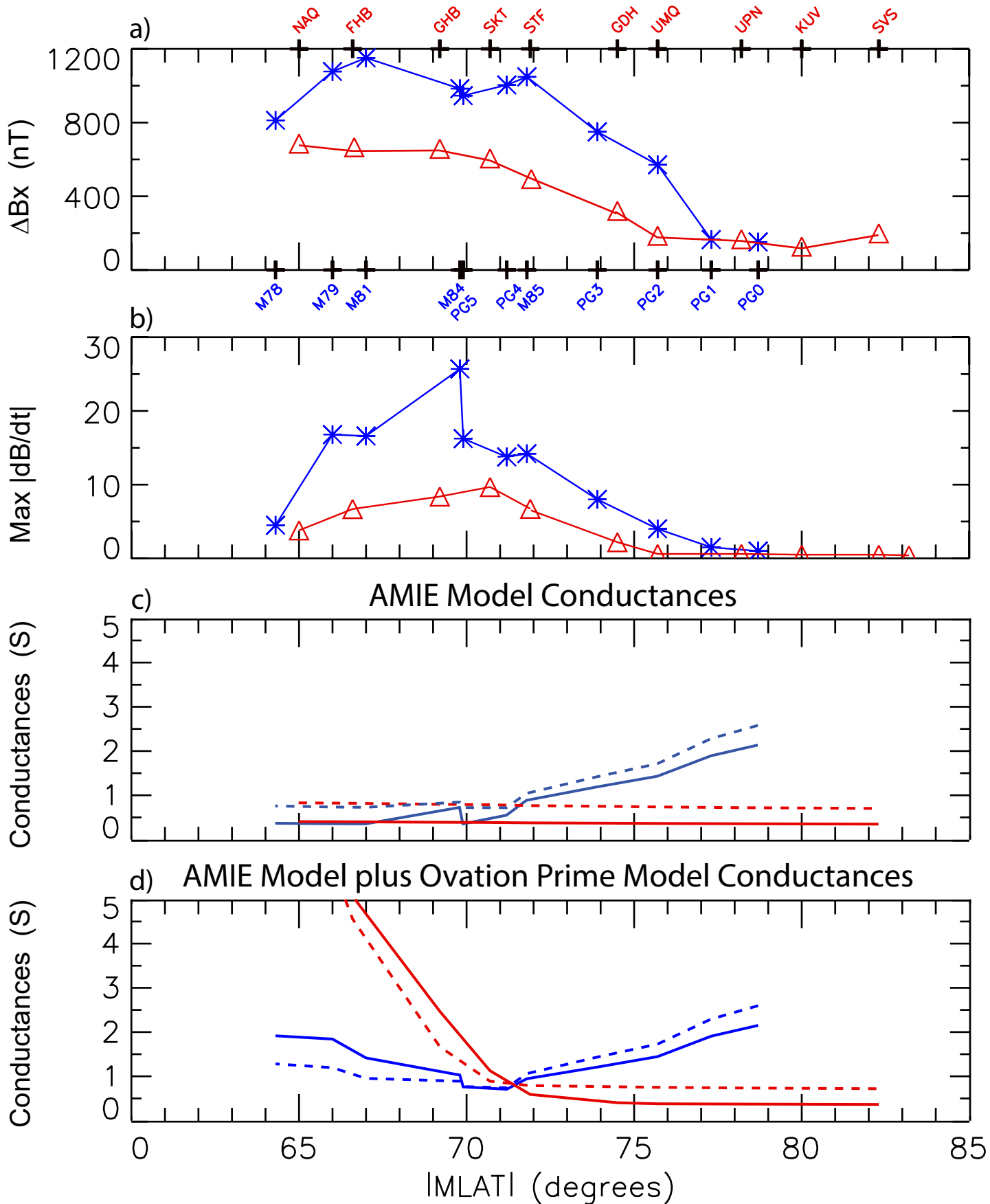
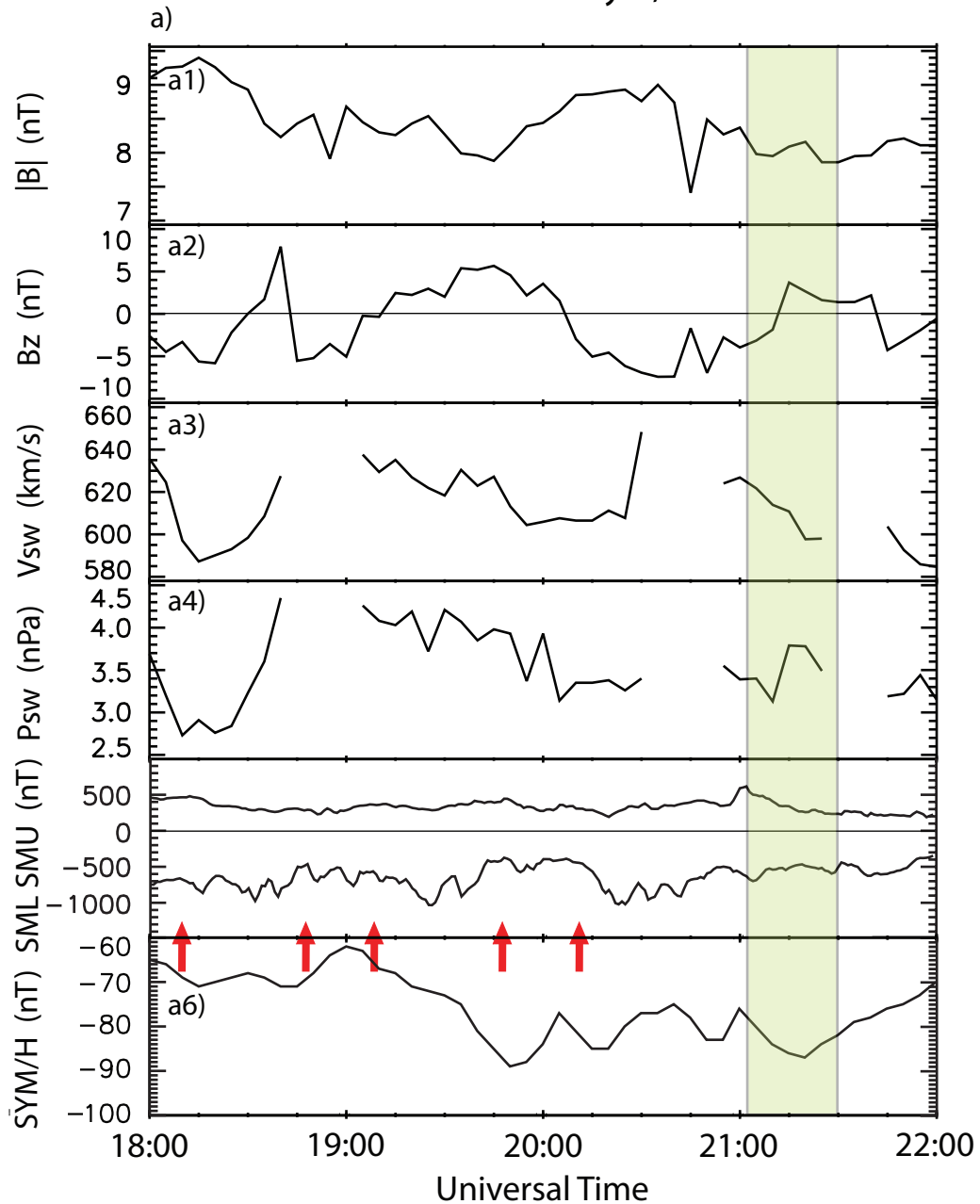


Figure 9.

OMNI data May 8, 2016



May 8, 2016 Yearday = 16129

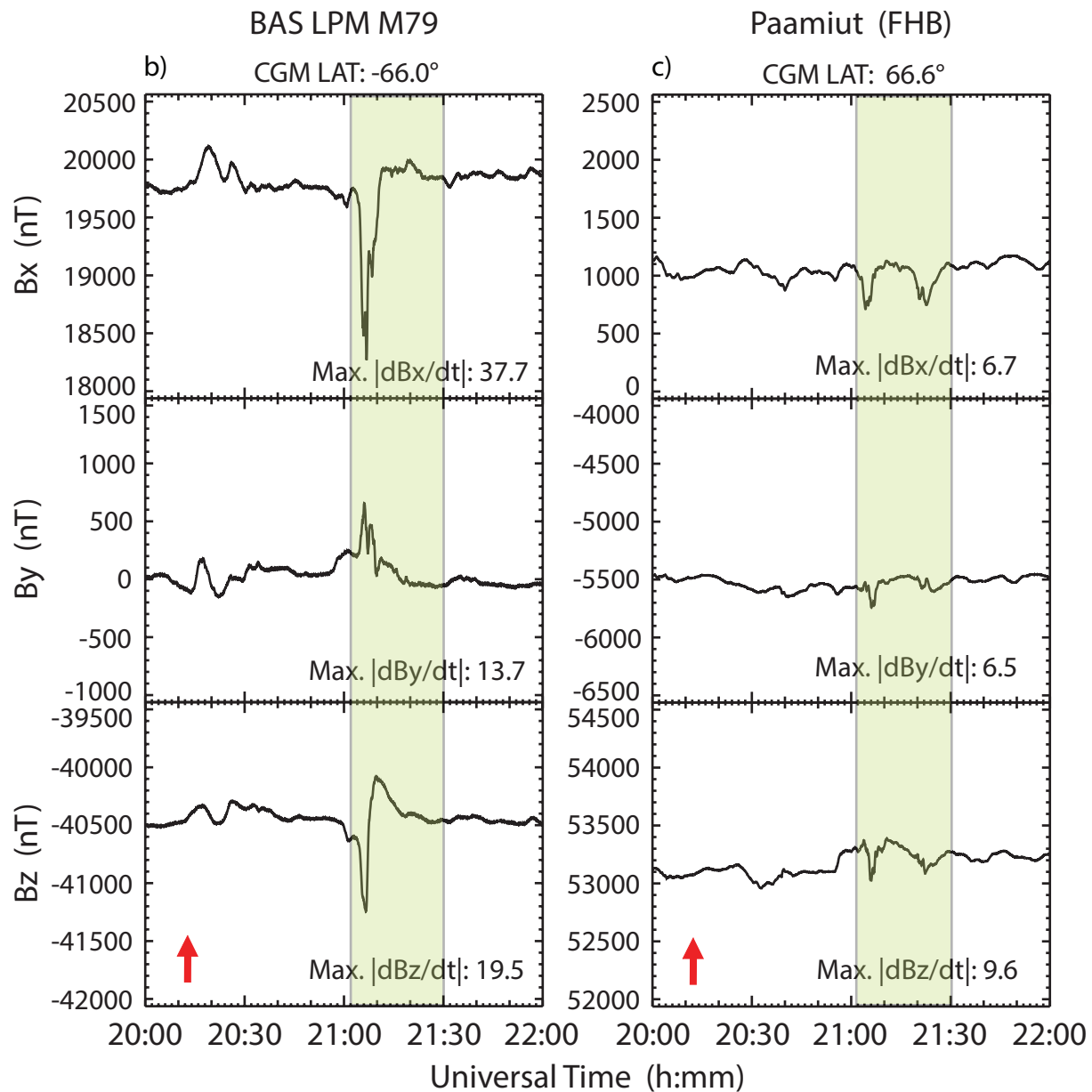
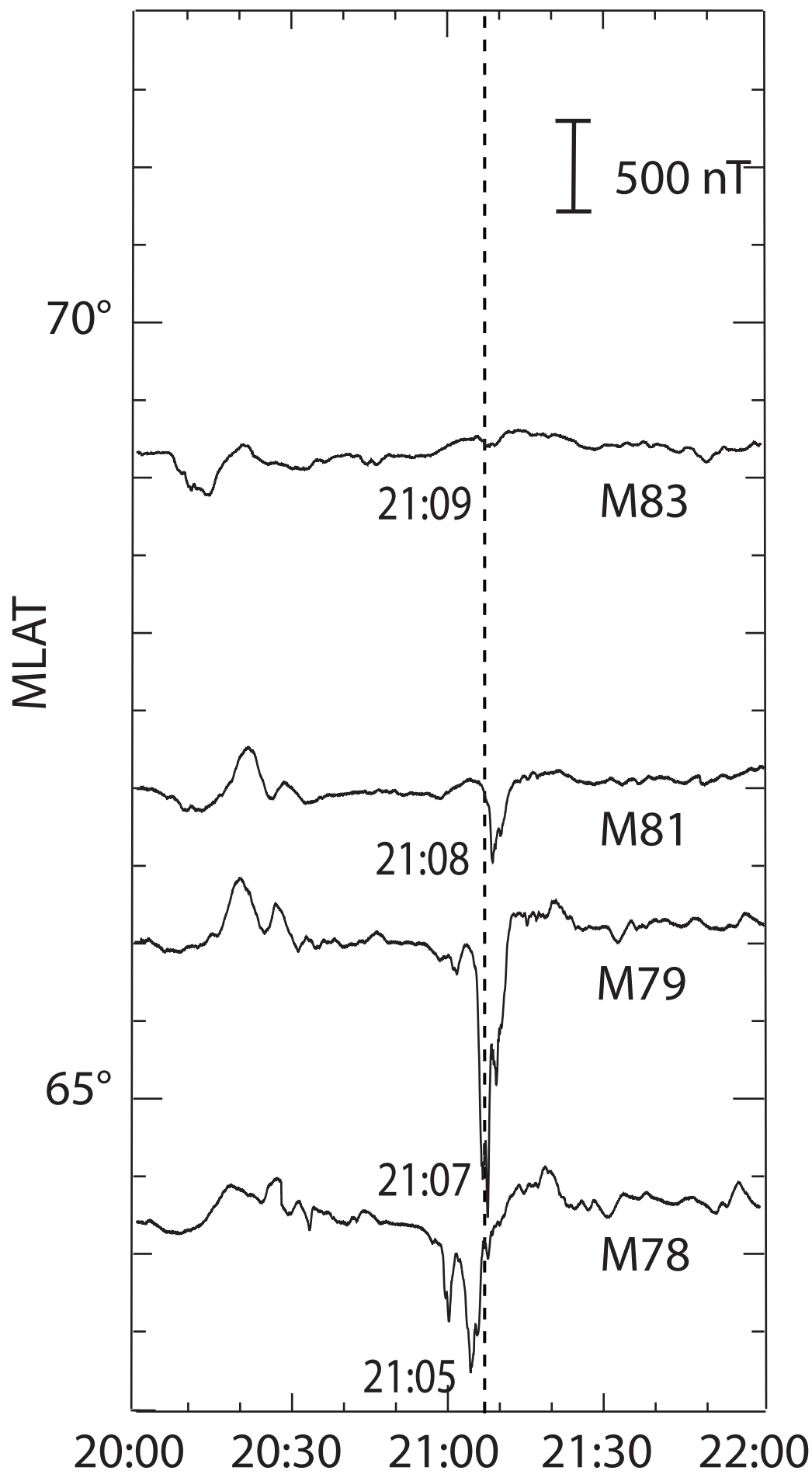


Figure 10.

# Antarctica

MLT ~ 19.1 h

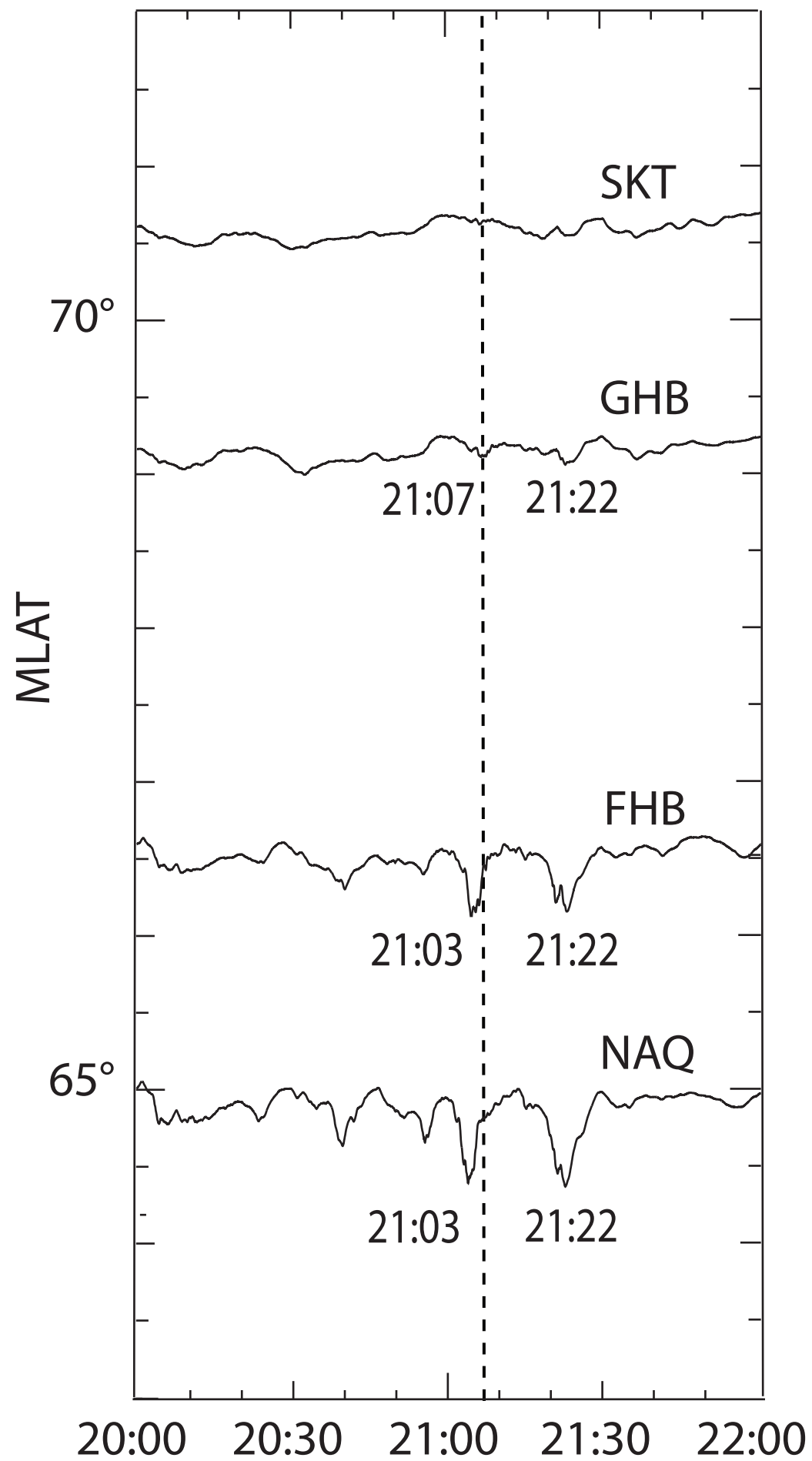
a)



# Greenland

MLT ~ 19.1 h

b)



Universal Time (hh:mm)

Figure 11.

May 8, 2016 16129 ~21:08 UT

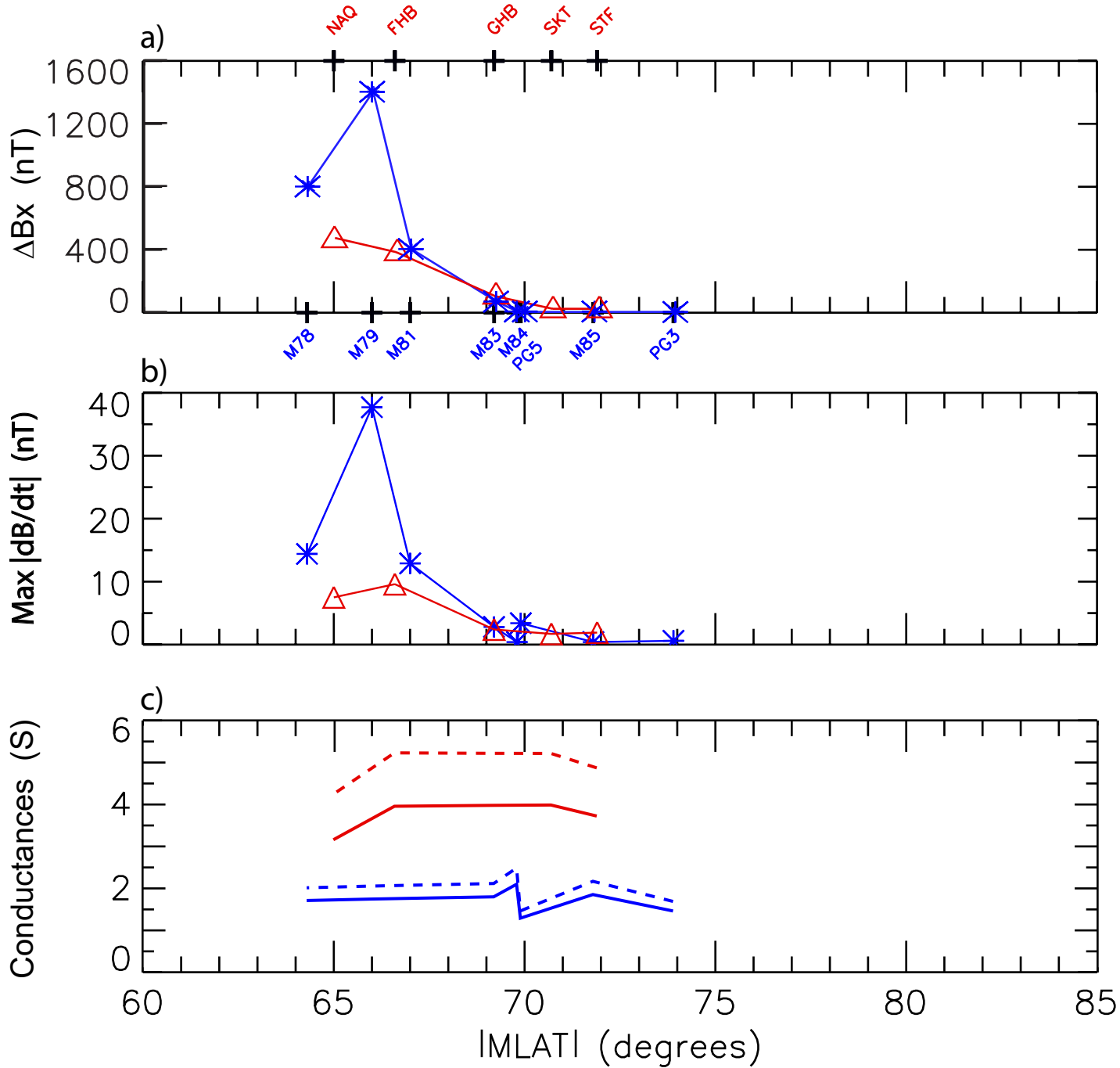


Figure 12.

OMNI data May 13, 2015

May 13, 2015

Yearday = 15133

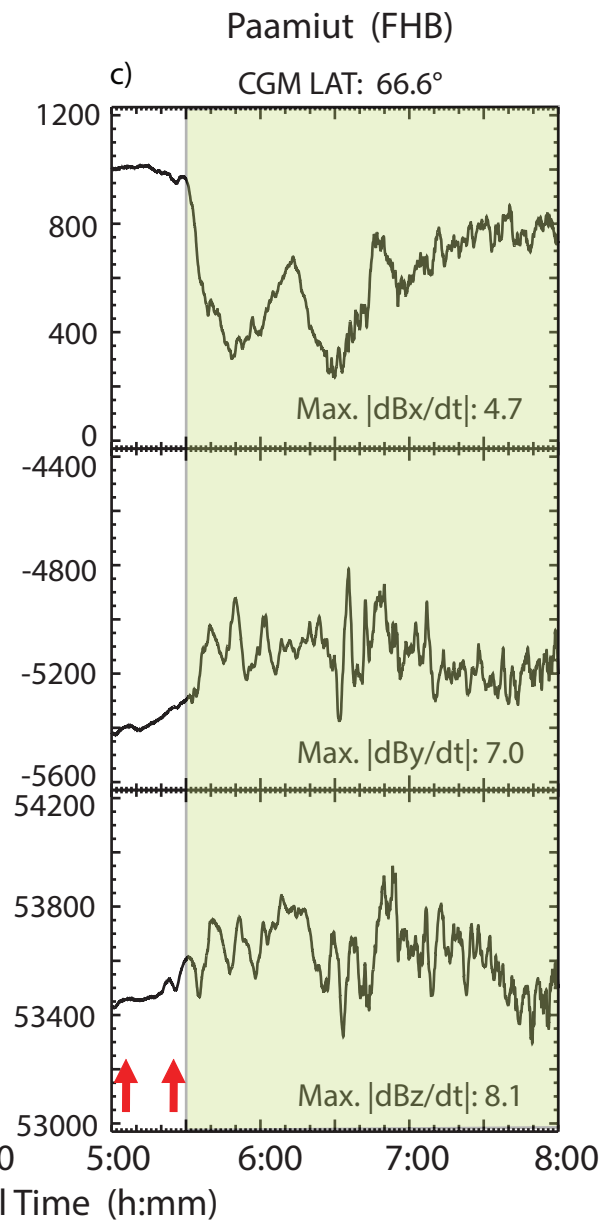
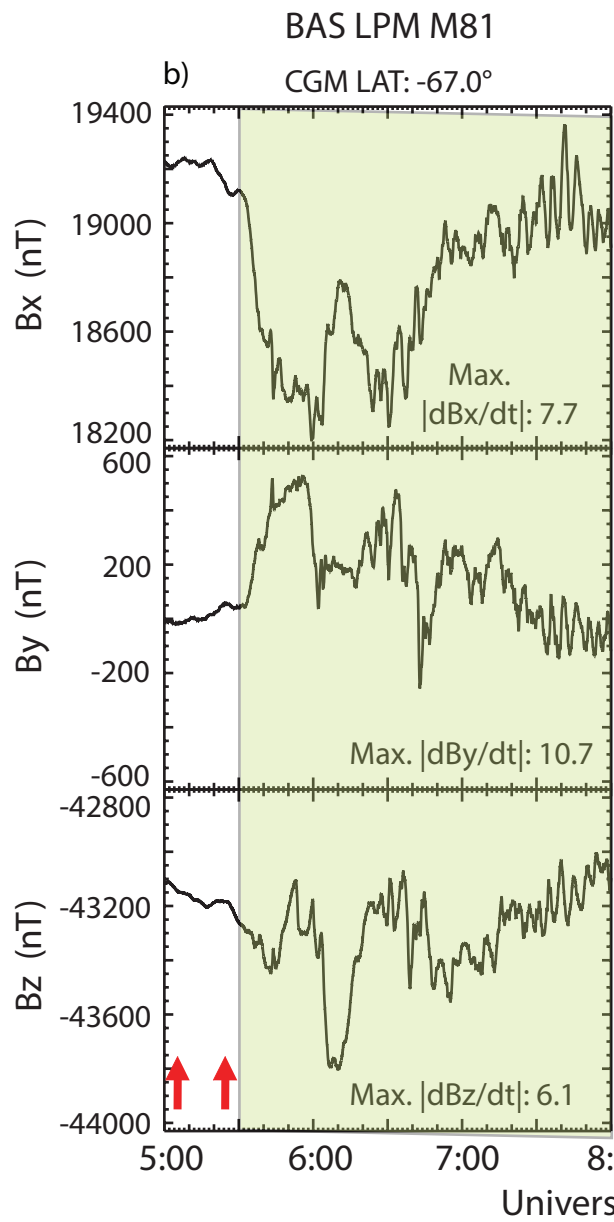
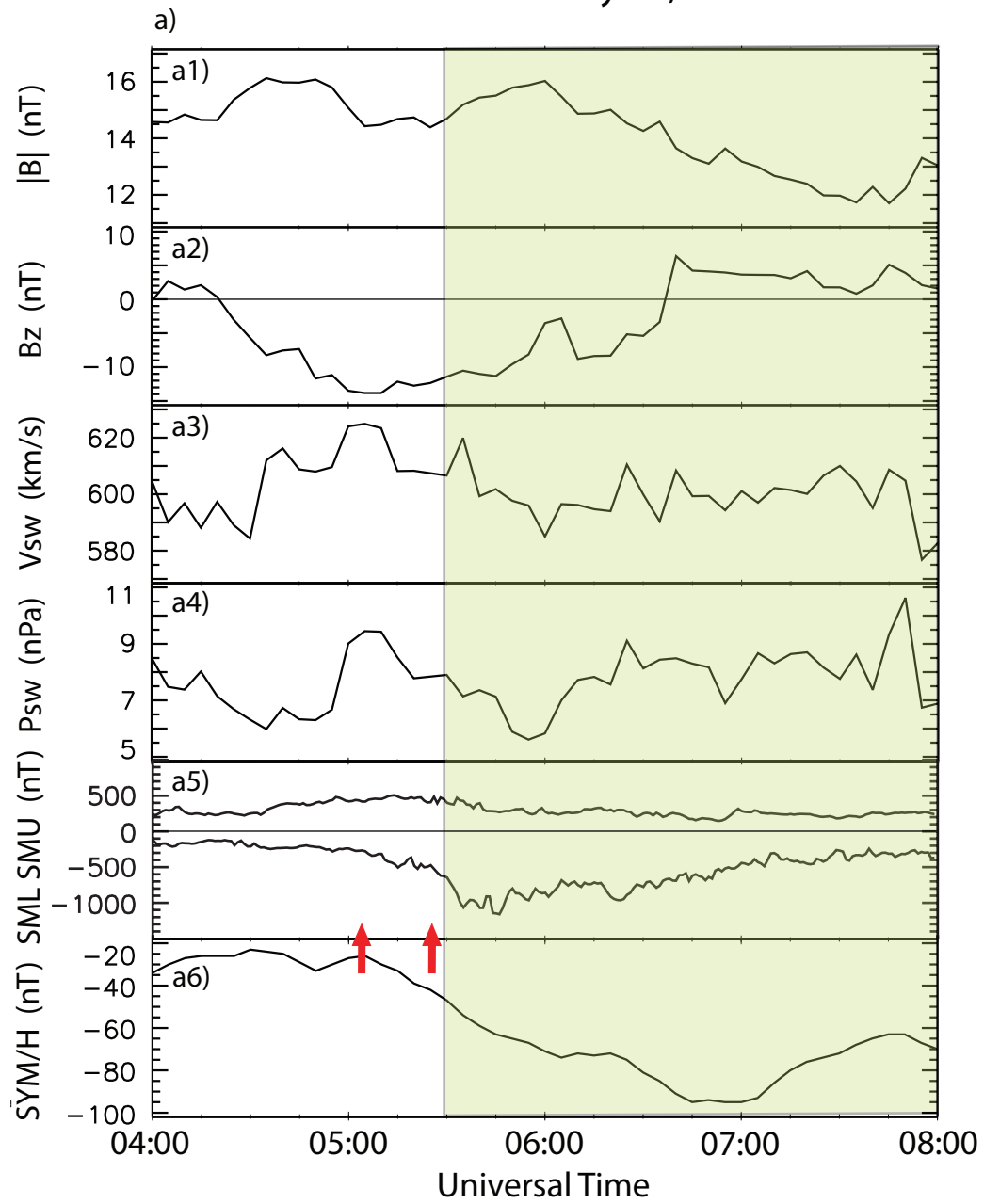
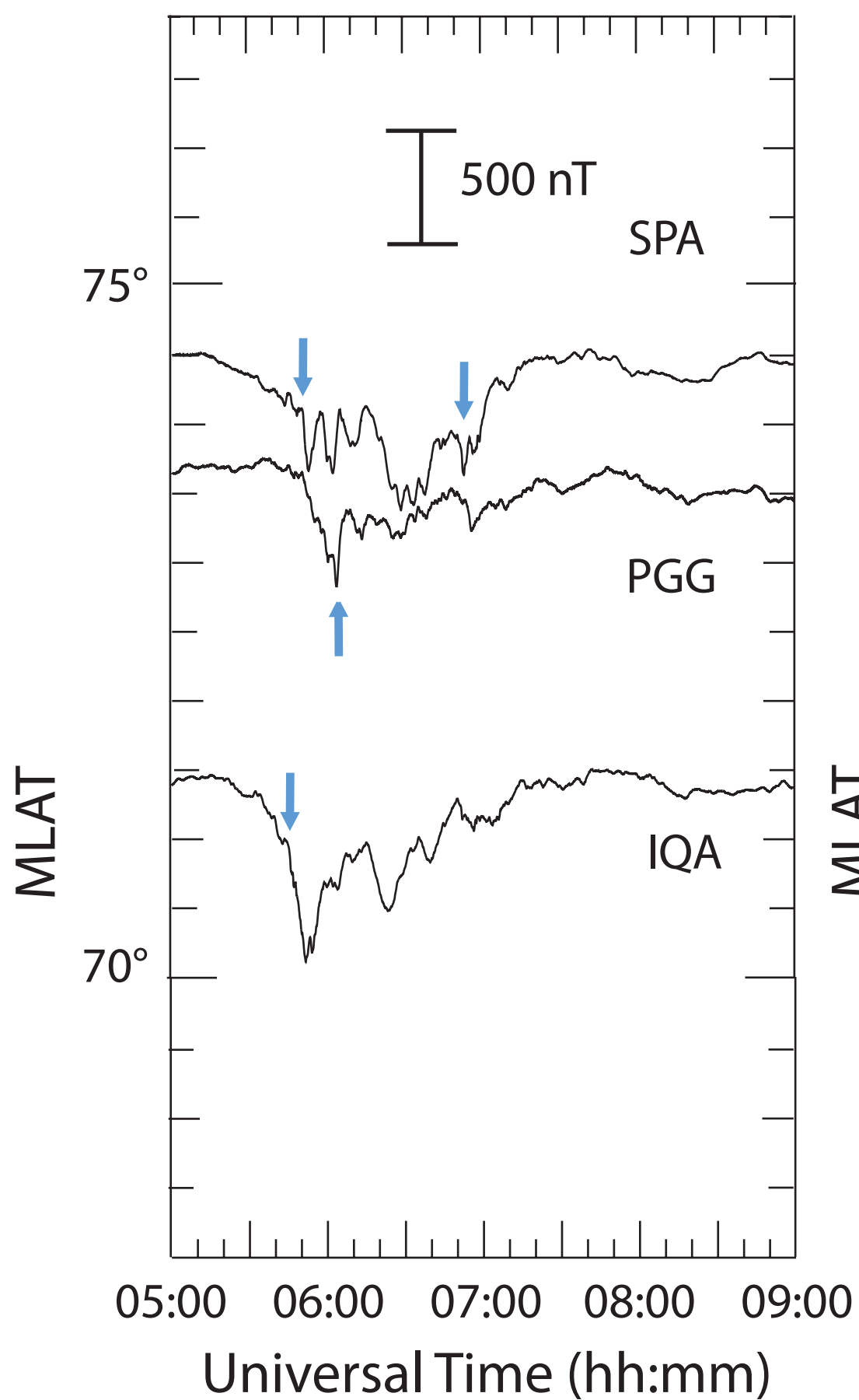


Figure 13.

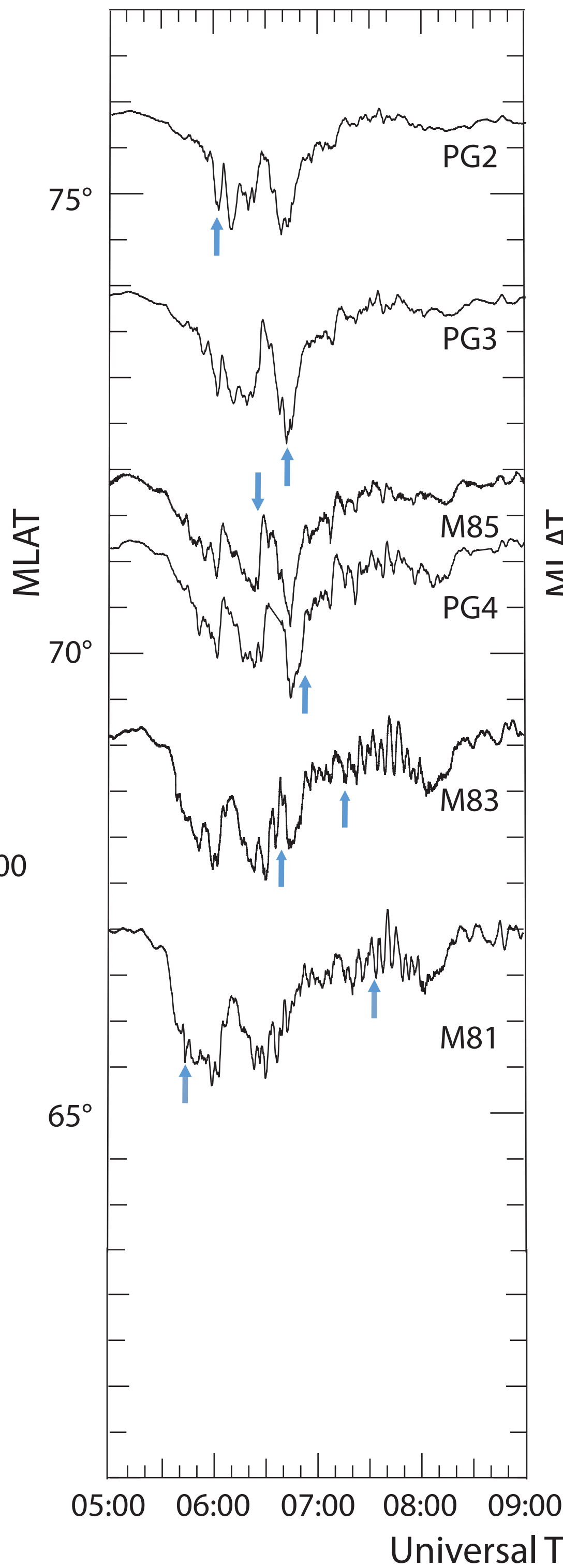
### Canada / Antarctica

a) MLT ~ 3 h



### Antarctica

b) MLT ~ 4.2 h



### Greenland

c) MLT ~ 4.2 h

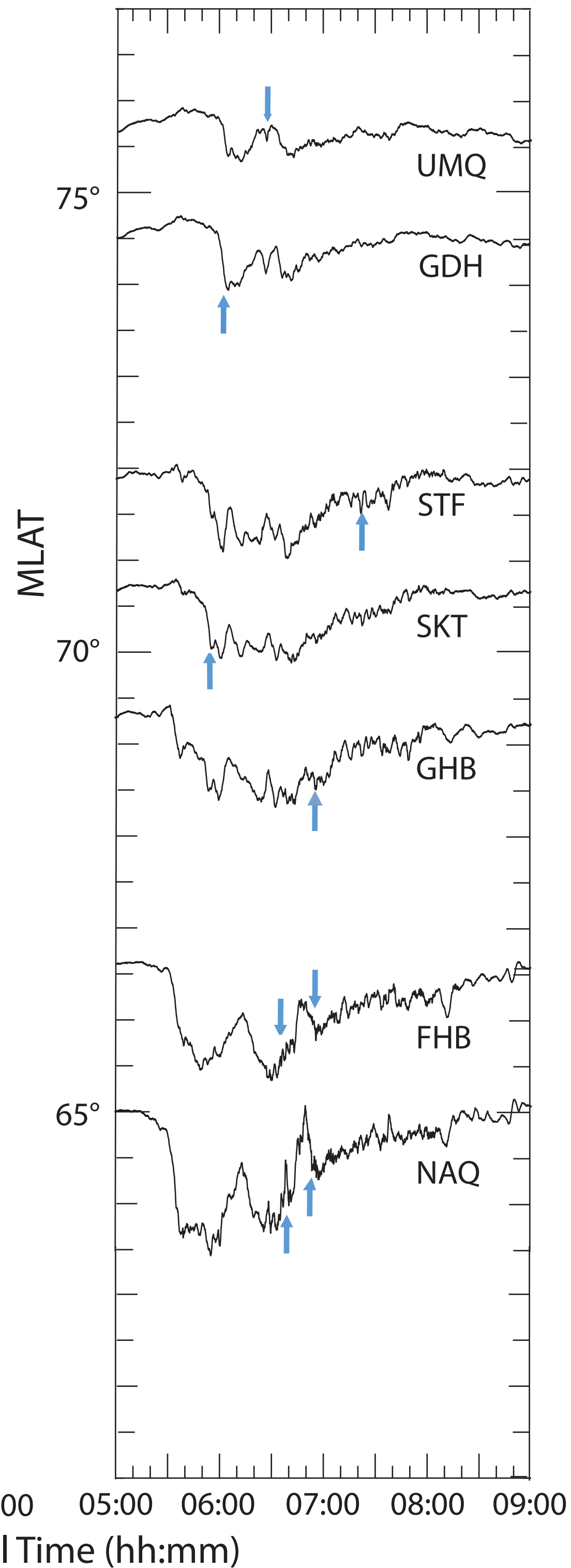


Figure 14.

May 13, 2015 15133 05:30 - 08:00 UT

